The silicon strip detectors of the ZEUS microvertex detector

Diplomarbeit am II. Institut für Experimentalphysik der Universität Hamburg

Dominik Dannheim
Holstenwall 13
D-20355 Hamburg

Genf, im August 1999

Abstract

A new silicon microvertex detector (MVD) will be installed in the ZEUS experiment during the shutdown for the HERA luminosity upgrade in 2000. This work gives an introduction into the layout of the MVD detector, presents the mechanical and electrical specifications for the detector modules and reports on electrical measurements of prototype detector modules and test structures.

The first chapter explains the basic properties of detector grade silicon, as far as it is important for the following. The models for currents and capacitances in silicon devices are presented. The influence of low energetic ionizing irradiation and of hadronic irradiation on the performance of silicon detectors is discussed.

Chapter two introduces the MVD detector and its basic specifications. The MVD is foreseen to improve the global precision of the ZEUS tracking system and will allow the study of heavy flavour physics with high efficiency.

Chapter three explains the layout of the MVD detector modules and the design of the test-structures. The surface area of the detectors is $41cm^2$, the thickness is about $330\mu m$. They are single sided, made of monocrystalline high resistivity n-type silicon with 512 readout p^+-strips, which are AC coupled to the readout electronics. The readout pitch is $120\mu m$. Between two readout strips there are five intermediate p^+-strips in order to improve the resolution by capacitive charge division. All strips are biased through poly-silicon biasing resistors. Three guard rings surround the active area of the detector. For each detector, one test-structure from the same wafer is produced. It allows by electrical measurements to determine technological parameters related to the detector performance.

Chapter four and five review the quality control measurements for the MVD prototype detectors. A test beam has been setup in order to characterize the performance of the detector modules and the readout electronics. A resolution of $\sigma_i \approx 7.5\mu m$ and a signal to noise ratio of about 22 have been determined. Electrical measurements have been performed on the detectors and the test-structures in order to check the electrical specifications. All measurements met the specifications. Measurements after a neutron irradiation test with $\phi_{eq} = 1 \cdot 10^{13} cm^{-2}$ were in the expected range. Measurements after $^{60}Co-$irradiation tests up to $2.9kGy$ showed an increase in the detector total leakage current by up to 4 orders of magnitude to a maximum value of about $400\mu A$. A shift in the flatband voltage from $-7V$ pre- to $-60V$ post-irradiation was also observed. By measurements on gate controlled diodes and PMOS transistors the additional leakage current has been attributed to surface generation current from generation centers at the $SiO_2 - Si-$interface. The detectors perform properly in the test beam after $^{60}Co-$irradiation.

Zusammenfassung

Zeitgleich mit dem Shutdown für das HERA Luminositäts-Upgrade im Jahr 2000 wird ein neuer Silizium-Mikrostreifen-Detektor (*engl.: silicon microvertex detector (MVD)*) in das ZEUS Experiment eingebaut werden. In dieser Arbeit werden das Layout des MVD und die mechanischen und elektrischen Spezifikationen für die Detektor-Module vorgestellt. Ferner werden elektrische Messungen beschrieben, die zur Überprüfung der Spezifikationen an Prototyp-Detektoren und Teststrukturen durchgeführt wurden.

Das erste Kapitel beschreibt die für die folgenden Kapitel wichtigen grundlegenden Eigenschaften von Detektor-Silizium. Modelle für Ströme und Kapazitäten in Silizium-Bauteilen werden vorgestellt. Der Einfluß von niederenergetischer ionisierender Strahlung und von hadronischer Strahlung auf Siliziumdetektoren wird diskutiert.

Der MVD Detektor und seine grundlegenden Spezifikationen werden im zweiten Kapitel eingeführt. Er soll die globale Präzision der ZEUS Spurvermessung verbessern und dadurch u.a. die Untersuchung schwerer Quark-Zustände mit hoher Effizienz erlauben.

Das dritte Kapitel beschreibt den Entwurf der MVD Detektormodule und der Teststrukturen. Die Fläche der Detektormodule beträgt $41cm^2$, die Dicke etwa $330\mu m$. Es handelt sich um einseitige Detektoren aus monokristallinem hochohmigen n-Typ-Silizium mit 512 p^+-Auslesestreifen, die kapazitiv an die Ausleseelektronik gekoppelt sind. Der Abstand der Auslesestreifen beträgt $120\mu m$. Zwischen zwei Auslesestreifen befinden sich 5 Zwischenstreifen zur Verbesserung der Ortsauflösung durch kapazitive Ladungsteilung. Alle Streifen sind durch Poly-Silizium-Vorwiderstände an die Spannungsversorgung angeschlossen. Die aktive Fläche wird von drei Guard-Ringen umgeben. Zu jedem Detektor wird eine Teststruktur auf demselben Wafer produziert, mit der durch elektrische Messungen technologische Parameter bestimmt werden, die für die Charakterisierung der Detektoren wichtig sind.

Kapitel vier und fünf beschreiben die Messungen zur Qualitätskontrolle der MVD Prototyp-Detektoren. Die Detektoren und ihre Ausleseelektronik wurden in einem Teststrahl-Experiment untersucht. Die gemessene Ortsauflösung beträgt $\sigma_i \approx 7.5\mu m$, das Signal/Rausch-Verhältnis wurde zu etwa 22 bestimmt. An den Detektoren und Teststrukturen wurden elektrische Messungen durchgeführt, um die Einhaltung der elektrischen Spezifikationen zu überprüfen. Alle Spezifikationen wurden erfüllt. Messungen nach Neutronenbestrahlung mit $\phi_{eq} = 1 \cdot 10^{13} cm^{-2}$ haben keine unerwarteten Effekte gezeigt. Bei Messungen nach $^{60}Co-$Bestrahlung bis zu $2.9kGy$ wurden um bis zu 4 Größenordnungen erhöhte Leckströme bis zu einem Maximalwert von etwa $400\mu A$ festgestellt. Außerdem wurde eine Verschiebung der Flachbandspannung von $-7V$ vor Bestrahlung auf $-60V$ nach Bestrahlung beobachtet. Durch Messungen an Gate-gesteuerten Dioden und PMOS-Transistoren konnte der erhöhte Leckstrom auf Oberflächengenerationsstrom von der $SiO_2 - Si-$Grenzfläche zurückgeführt werden. Im Teststrahl haben die mit ^{60}Co bestrahlten Detektoren keine Veränderung gegenüber unbestrahlten Detektoren gezeigt.

Contents

1 Silicon strip detector principles **6**
- 1.1 Physical properties of detector grade silicon . . . 6
- 1.2 The p-n junction . . . 8
- 1.3 Capacitances in silicon devices . . . 12
  - 1.3.1 Junction capacitance . . . 12
  - 1.3.2 Additional Capacitance from MOS-region . . . 12
- 1.4 Currents in silicon devices . . . 13
- 1.5 Radiation induced damage of silicon devices . . . 14
  - 1.5.1 Oxide and surface damage due to low energy ionizing radiation . 14
  - 1.5.2 Displacement damage due to high energetic hadronic radiation . 15

2 The Silicon Microvertex Detector (MVD) at ZEUS **20**
- 2.1 The ZEUS detector at HERA . . . 20
- 2.2 Requirements for the MVD . . . 23
- 2.3 Layout of the MVD detector system . . . 23
  - 2.3.1 BMVD layout . . . 23
  - 2.3.2 BMVD ladders . . . 24
  - 2.3.3 FMVD layout . . . 27
- 2.4 Radiation monitoring . . . 28
- 2.5 Readout electronics . . . 29

3 Design of the MVD detector modules **31**
- 3.1 Layout of the BMVD detector modules . . . 31
- 3.2 Design of the test structures . . . 33

4 Test beam measurements **36**
- 4.1 Test beam setup . . . 36
- 4.2 Test beam results . . . 37

5 Electrical measurements **38**
- 5.1 Test setup . . . 38
  - 5.1.1 Probe station . . . 38
  - 5.1.2 Electrical setup for I/V and C/V measurements . . . 38
  - 5.1.3 Long-term I/V measurements . . . 39

5.1.4 $\gamma-$irradiation 40
5.1.5 Neutron-irradiation 41
5.2 Measurement results 41
5.2.1 Total bulk capacitance C_{bulk} 41
5.2.2 Depletion Voltage 44
5.2.3 Effective doping concentration 47
5.2.4 Resistivity of the n-material 48
5.2.5 Biasing resistors 48
5.2.6 p^+ strip resistance 51
5.2.7 Doping concentration N_a of p^+-implantations 51
5.2.8 Built-in-voltage V_{bi} 52
5.2.9 Aluminum strip resistance 52
5.2.10 Coupling capacitance 53
5.2.11 Quality of coupling capacitance dielectric 54
5.2.12 Total leakage current 55
5.2.13 Long-term monitoring of the leakage current 62
5.2.14 MOS capacitor measurements 63
5.2.15 Gated diode measurements 69
5.2.16 Hole mobility in the interface area 75
5.2.17 $p^+ - p^+-$isolation 77
5.2.18 Summary of electrical measurements and conclusions for production quality control 83

6 Summary **87**

A Measurement principle of an LCR meter **89**

References **93**

Chapter 1

Silicon strip detector principles

1.1 Physical properties of detector grade silicon

This section gives a short overview about the basic electric properties of silicon.

Silicon atoms form a diamond like face centred cubic lattice, in which each silicon atom is surrounded by four neighbouring atoms in a tetrahedral configuration.

The electric properties of silicon are best described within the band theory. For silicon the band gap, i.e. the energy difference between the conduction band and the valence band, is

$$E_g = E_c - E_v = 1.12\,eV.$$

At $T = 0K$ the valence band is completely filled and no electrons are excited to the conduction band. Thus the silicon behaves as an isolator. But already at room temperature ($kT \approx 25meV$) electrons from the valence band overcome the small gap and enter the conduction band where they can take part in electrical conduction. The missing electrons (holes) in the valence band are also mobile and contribute to the electrical conductivity.

In intrinsic silicon the concentration of electrons in the conduction band n_e and the concentration of holes in the valence band n_h has to be equal:

$$n_e = n_h = n_i \tag{1.1}$$

At $T = 20^oC$ the intrinsic charge carrier density is [Sze81]

$$n_i = 8.34 \cdot 10^9 cm^{-3}.$$

The equilibrium density of electrons and holes in silicon can be changed by doping with donors or acceptors. Donors are atoms with 5 electrons in the outer shell. Only 4 of them are needed for the covalent bonding with the silicon atoms, therefore the 5th electron is "donated" to the valence band. The number of electrons in the valence band can be as high as the number of donors. Acceptors have only 3 electrons in the outer shell. To complete the covalent bonds to the neighbouring atoms they "accept" an electron from the valence band, where a hole is left. The number of holes in the valence band can be as high as the number of acceptors. Due to the *mass action law*

the product of electron and hole concentration in equilibrium is always equal to the square of the intrinsic carrier concentration:

$$n_e n_h = n_i^2 \tag{1.2}$$

The resistivity ρ, which is the inverse of the conductivity γ, can be evaluated from the charge carrier densities, their low field mobilities $\mu_{e,h}$ and the electron charge $q = 1.602 \cdot 10^{-19} C$ as

$$\rho = \gamma^{-1} = \frac{1}{q(\mu_e n_e + \mu_h n_h)} \tag{1.3}$$

For intrinsic silicon the mobility of electrons and holes at $T = 20^o C$ is $\mu_e = 1500 cm^2/Vs$ and $\mu_h = 450 cm^2/Vs$ which yields a resistivity of $\rho = 219 k\Omega cm$. For high electric fields ($E > 2kV/cm$) the linear relation between drift velocity and electric field strength $v = \mu E$, based on a constant mobility, is not anymore valid.

If the concentration of donors N_d exceeds the concentration of acceptors N_a ($N_d > N_a$) the material is called *n-type*, the electrons are majority carriers and the holes are minority carriers. For $N_a > N_d$ the material is called *p-type*, the holes are majority carriers and the electrons are minority carriers.

Phosphorous is often used as donor and boron as acceptor. The energy level of a single phosphorous atom E_c in silicon is close to the conduction band ($E_c - E_p \approx 45 meV$). Thus even at low temperature all phosphorous atoms are ionised ($N_d \approx n_e$). For boron the corresponding energy level E_b is close to the valence band ($E_b - E_v \approx 44 meV$) and therefore all boron levels are occupied by electrons from the valence band, leaving a concentration of holes $N_a \approx n_h$ in the valence band.

The resistivity ρ of a doped material can also be attributed to an *effective doping concentration* N_{eff} which is the net effect of ionized donors and acceptors:

$$N_{eff} = N_d - N_a \tag{1.4}$$

Accordingly, for n-type material N_{eff} is positive and for p-type it is negative.

The resistivity of detector grade silicon has to be very high, i.e. the doping concentration has to be very low ($\rho > 2 k\Omega cm \cong N_{eff} \leq 1 \cdot 10^{12}$).

The occupation of electrons and holes over the possible energy states is determined by the Fermi-Dirac statistics. The Fermi energy E_F is an important parameter in the corresponding distribution function

$$F(E) = \left(1 + \exp\left(\frac{E - E_F}{kT}\right)\right)^{-1}. \tag{1.5}$$

E_F can be obtained from the equilibrium density of electrons and holes.

$$n_e = N_c(T) \exp\left(-\frac{E_c - E_F}{kT}\right) \tag{1.6}$$

$$n_h = N_v(T) \exp\left(-\frac{E_F - E_v}{kT}\right) \tag{1.7}$$

$$n_i = \sqrt{N_c N_v} \exp\left(-\frac{E_g}{2kT}\right) \tag{1.8}$$

$N_c(T)$ and $N_v(T)$ are the effective densities of states at the bottom of the conduction band and at the top of the valence band, respectively. For intrinsic silicon the Fermi energy at room temperature E_{F_i} is almost in the middle between the valence and the conduction band.

$$E_{F_i} = \frac{E_c + E_v}{2} + \frac{kT}{2} \cdot \ln N_v/N_c \tag{1.9}$$

For n-type silicon ($n_e \approx N_d$) the Fermi energy E_{F_n} is close to the conduction band, for p-type silicon ($n_h \approx N_a$) E_{F_p} is close to the valence band (see figure 1.1).

$$E_{F_n} = E_c - kT \cdot \ln N_c/N_d \tag{1.10}$$

$$E_{F_p} = E_v + kT \cdot \ln N_v/N_a \tag{1.11}$$

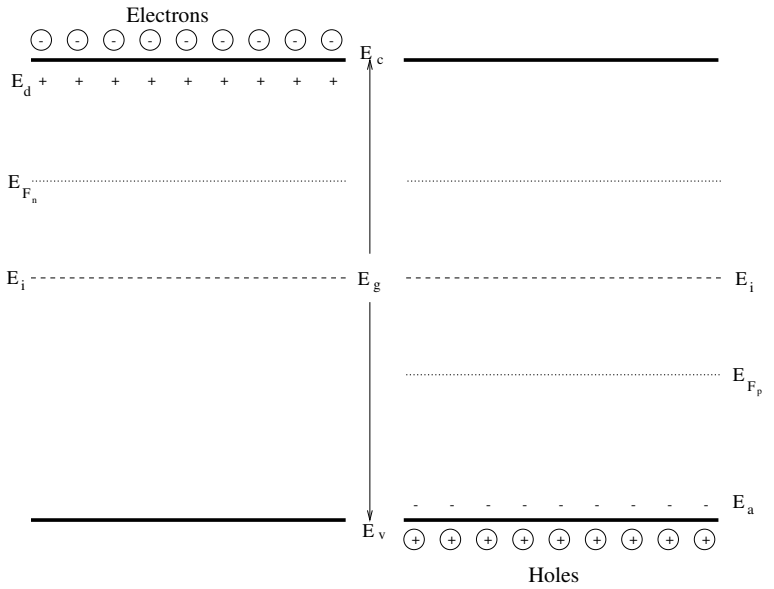

Figure 1.1: Energy diagram for n-type (left) and p-type (right) silicon. E_d denotes the energy level of the donor and E_a that of the acceptor.

Some important properties of detector grade silicon are summarized in table 1.1.

1.2 The p-n junction

An abrupt change from a surplus of acceptors N_a on the p-side to a surplus of donors N_d on the n-side is called a p-n junction, or a p^+-n junction, if $N_a >> N_d$. If the lateral dimensions of the junction are much larger than the overall thickness of the configuration, a one dimensional treatment is appropriate.

In thermal equilibrium both, hole and electron current densities, are zero:

$$J_e = J_h = 0 \tag{1.12}$$

atomic mass	$28.09amu$
crystal lattice	face centred cubic (diamond)
lattice constant	$5.43\mathring{A}$
electrical permitivity $\epsilon_{Si} = \epsilon_r \cdot \epsilon_0$	$11.9 \cdot 8.854 \cdot 10^{-14} F/cm$
bandgap E_g	$1.12eV$
intrinsic charge carrier density n_i	$8.34 \cdot 10^9 cm^{-3}$
electron mobility μ_e	$1500cm^2/Vs$
hole mobility μ_h	$450cm^2/Vs$
resistivity ρ	$219k\Omega cm$

Table 1.1: Some important properties of detector grade silicon, according to [Sze81] (all values given for $T = 20^oC$).

On the other hand the electron- and hole-currents are driven by the electric field:

$$J_e = -\mu_e n_e \frac{dE_F}{dx} \tag{1.13}$$

$$J_h = \mu_h n_h \frac{dE_F}{dx} \tag{1.14}$$

These equations show that in equilibrium the Fermi-level has to be constant at the junction which means that the conduction and valence band bend (see figure 1.2).

The potential difference between the bottom of the conduction band on the p-side and its bottom on the n-side is called the *built-in potential* V_{bi}.

Due to the electric field the region where the energy bands are bent is depleted of free charge carriers. The uncompensated donors and acceptors build a space charge and therefore this region is called *depletion region* or *space charge region* (SCR). The width of the depletion region depends on the built-in-voltage and on the concentration of donors and acceptors. Poisson's equation has to be fulfilled for any distribution of fixed charges:

$$-\frac{d^2V}{dx^2} = \frac{dE}{dx} = \frac{\rho_c(x)}{\epsilon_{Si}}. \tag{1.15}$$

$\rho_c(x)$ denotes the charge density per unit volume. In case of an abrupt junction this yields for the n-side of the depletion region ($0 < x \leq x_n$):

$$\frac{dE}{dx} = \frac{q}{\epsilon_{Si}} N_d \tag{1.16}$$

and for the p-side ($-x_p \leq x < 0$):

$$\frac{dE}{dx} = -\frac{q}{\epsilon_{Si}} N_a, \tag{1.17}$$

x_n and x_p are defined in figure 1.2.

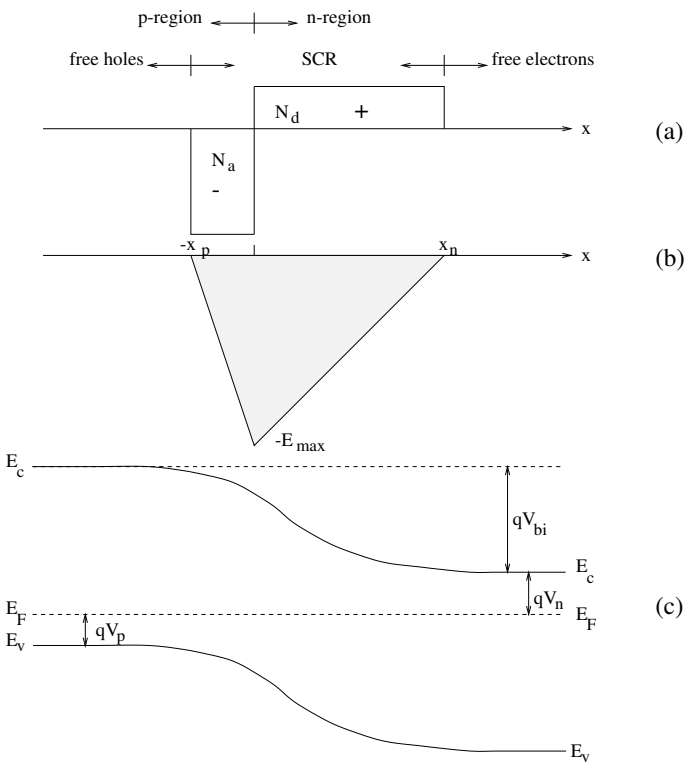

Figure 1.2: Abrupt p-n junction. (a) Space charge distribution. (b) Electric field distribution. (c) Energy-band diagram.

The electrical field E and built-in-potential V_{bi} can be obtained from these equations by integration. For the n-side the electrical field is

$$E_n = \frac{qN_d(x - x_n)}{\epsilon_{Si}} \tag{1.18}$$

and for the p-side:

$$E_p = \frac{-qN_a(x + x_p)}{\epsilon_{Si}}. \tag{1.19}$$

The built-in-potential V_{bi} is

$$V_{bi} = \frac{1}{2}E_{max}W, \tag{1.20}$$

where $W = x_n + x_p$ is the total width of the depletion region and E_{max} is the maximum field at $x = 0$:

$$E_{max} = E(x = 0) = \frac{qN_a x_p}{\epsilon_{Si}} = \frac{qN_d x_n}{\epsilon_{Si}}. \tag{1.21}$$

In case of $N_a >> N_d$ $(p^+ - n - junction)$ the last two equations yield

$$W = \sqrt{\frac{2\epsilon_{Si}}{qN_d}V_{bi}}, \tag{1.22}$$

with

$$V_{bi} = \frac{kT}{q} \cdot \ln \frac{N_a \cdot N_d}{n_i^2}. \tag{1.23}$$

For high resistivity silicon, as it is used for detector applications, the donor concentration N_d has to be replaced by the effective doping concentration N_{eff}. Another correction comes from the Debye-tail of the carrier distribution at the edges of the depletion region which introduces a term kT/q. An external voltage V can add to the built-in-potential V_{bi} and thus also change the width of the depletion region given by:

$$W = \sqrt{\frac{2\epsilon_{Si}}{qN_{eff}}(V + V_{bi} + \frac{kT}{q})}. \tag{1.24}$$

For external voltages which are large compared to $V_{bi} \approx 0.7V$ (see section 5.2.8) and $kT/q \approx 25mV$ the width of the SCR can be derived from the simplified expression:

$$W(V) = \sqrt{\frac{2\epsilon_{Si}}{qN_{eff}}V} \tag{1.25}$$

1.3 Capacitances in silicon devices

1.3.1 Junction capacitance

For large bias voltages the main contribution to the measured capacitance in a reverse biased silicon detector is given by the junction capacitance of the depletion zone. If deep trap levels are neglected, it can be shown that the dynamic junction capacitance $C_j = dQ/dV$ is related to the width W of the depleted volume by [Sze81]:

$$C_j = \epsilon_{Si} \cdot \frac{A}{W(V)}. \tag{1.26}$$

This means that the detector behaves like a parallel plate capacitor with two electrodes of the area A at a distance W. With the voltage dependence of the depletion width from equation (1.24) the junction capacitance can be written as:

$$C(V) = A\sqrt{\frac{\epsilon_{Si} q N_{eff}}{2(V + V_{bi})}}; \quad V \leq V_{dep} \tag{1.27}$$

$$C = C_{geom} = \frac{\epsilon_{Si} A}{d}; \quad V > V_{dep} \tag{1.28}$$

For bias voltages, which are large compared to the built-in-voltage V_{bi}, the capacitance is proportional to $\sqrt{V_{bias}}$. If $1/C^2$ is plotted versus V, independent of V_{bi} a straight line with slope $1/N_{eff}$ is expected until the *depletion voltage* is reached whereafter the capacitance remains constant.

The effective doping concentration can be calculated from the depletion voltage:

$$|N_{eff}| = \frac{(V_{dep} + V_{bi}) \cdot 2\epsilon_{Si}}{q \cdot d^2} \tag{1.29}$$

1.3.2 Additional Capacitance from MOS-region

For n-type bulk material an electron accumulation layer below the SiO_2-layer acts like a conducting plate for the capacitance measurements and thus affects the measured capacitance depending on the geometry. In silicon structures with a simple geometry, like MOS[1] capacitors and gated diodes, the contribution from the MOS region to the total capacitance can be controlled by the gate voltage above the SiO_2. However, the geometric situation is much more complicated for the silicon strip detector modules, which were investigated in this study. Only every sixth p^+-strip is covered by an aluminum readout strip that can act as gate. The field distribution between the strips depends on the electron accumulation layer and on the bias conditions. Only for small bias voltages an electron layer below the SiO_2 can be expected, that can contribute to the capacitance.

[1] MOS = Metal Oxyde Semiconductor

1.4 Currents in silicon devices

In an n-type silicon detector under reverse bias different sources for the current can be distinguished:

- Currents due to improper fabrication or handling of detectors like *surface leakage currents* or *high field effects* are ignored in the following discussion.
- *Diffusion current.* The external electric field leads to a current density of diffusing minority carriers against the concentration gradient according to the Shockley equation:

$$I_{diff} = I_{S,D}\left(\exp\left(\frac{q\cdot V}{k\cdot T}\right)-1\right) \tag{1.30}$$

$$I_{S,D} \approx q\sqrt{\frac{D_p}{\tau_p}}\frac{n_i^2}{N_{eff}} \tag{1.31}$$

  with $V<0$ for reverse bias. The diffusion constant D_p is given by the *Einstein relation* as:

$$D_p = \frac{kT}{q}\mu_h \tag{1.32}$$

  For room temperature this yields a value of

$$I_{diff} = 98\%\cdot I_{S,D}$$

  already at $V = 0.1V$. For the measured diffusion current and effective doping concentration the minority carrier lifetime can be derived from these equations.

- *Bulk volume generation current.* The reverse current arising from generation of electron hole pairs in the electric field zone grows with the width of the depleted volume which depends on the bias voltage according to equation (1.24)[2]. The bulk volume generation current I_{bulk} is related to the generation lifetime τ_g by

$$I_{bulk}(V) = qAn_i\frac{W(V)}{\tau_g} \tag{1.33}$$

- *Interface generation current.* The interface- or surface-generation current I_S in silicon devices arises from electron-hole pair generation at the $Si-SiO_2-$interface regions. It is given by

$$I_S = qA_S n_i S_0. \tag{1.34}$$

[2]This voltage dependence has to be corrected for small bias voltages, otherwise also under zero bias a generation current would flow. Therefore the so-called generation width W_g is introduced, which is however almost equal to the depletion width W for bias voltages large compared to the built-in-voltage $V_{bi} \approx 0.7V$. [Fei97]

Only interface states inside an electric field zone contribute to the current. Therefore I_S is suppressed in case of an inversion or accumulation layer below the SiO_2 which shields the interface states from the electric field. The complicated geometry and field distribution at the surface region of a strip detector makes it difficult to predict the depleted interface area A_S which is taking part in the generation process. However, on special test-structures the interface generation current can be investigated in detail with a well defined switching from accumulation via depletion to inversion. (see section 5.2.15). The amount of interface states contributing to the surface recombination velocity S_0 is characteristic for the quality of the SiO_2-processing during production. Hydrogen annealing is a standard method to avoid large interface currents. As one of the last production steps hydrogen is diffused into the silicon device. The hydrogen atoms can inactivate generation centers by occupying dangling bonds from the defects located close to the interface. The resulting bonds are however weak and can be destroyed by $\gamma-$irradiation, leading to an increase of active defects again (see section 1.5.1).

1.4.0.1 Temperature dependence

All currents in silicon devices are strongly temperature dependent. The current measured at a temperature T can be scaled to the corresponding current at 20^oC, which has been done for all measurements in this work. For the bulk generation current the following formula can be used:

$$I_{20} = I_T \cdot \left(\frac{T_{20}}{T}\right)^2 \cdot \exp\left(\frac{E_g}{2} \cdot \frac{q}{k} \cdot \left(\frac{1}{T} - \frac{1}{T_{20}}\right)\right) \tag{1.35}$$

For the effective energy gap at room temperature E_g a value of $E_g = 1.21eV$ has been used [FM54]. In the temperature range around $T = 20^oC$ the change in the leakage current is about $8\%/^oC$.

For the surface generation current the same formula can be used if the $(T_{20}/T)^2$ -term is replaced by a $(T_{20}/T)^3$ dependence [NB82]. However, in the small temperature range of the measurements described in this work ($18^oC < T < 24^oC$), the difference to the bulk generation temperature dependence is very small. Therefore for all current measurements the formula (1.35) has been used to normalize the measured current to $T = 20^oC$.

1.5 Radiation induced damage of silicon devices

1.5.1 Oxide and surface damage due to low energy ionizing radiation

Electron-hole pairs created by ionizing particles do not cause permanent damage in crystalline silicon. The amorphous SiO_2 surface on the contrary is very sensitive to ionizing radiation. Because of the large band gap of $8.8eV$ in SiO_2, free electrons and

holes can be trapped by deep levels associated with defects in the oxide. From these levels an emission back into the valence or conduction band is very unlikely at room temperature. The number of hole traps outbalances the number of defects that can trap electrons. The drift mobility of electrons in SiO_2 at room temperature is about $20\,cm^2V^{-1}s^{-1}$, whereas for holes the mobility is only about $2 \cdot 10^{-5} cm^2V^{-1}s^{-1}$ [Bra89]. Thus the trapping probability for holes is much larger than for electrons, leading to a positive charge-up of the SiO_2.

Most of the traps are located around $5nm$ of the $SiO_2 - Si-$interface, where most of the substoichiometry and imperfectly grown oxide is located [Fei97]. The center of gravity of the created charges will therefore almost be at the $SiO_2 - Si-$interface.

The charging up of the oxide can be enhanced by an external field with field lines pointing from the gate in the direction towards the bulk. In this case the recombination of electrons and holes is suppressed, the holes are driven through the $SiO_2 - Si-$interface and therefore the number of charges that can be trapped increases. If the field is inverted, the recombination of electrons and holes is still suppressed, but the holes are repelled by the $SiO_2 - Si-$interface and the charging up of the oxide will be diminished.

Another effect of ionizing radiation in SiO_2 is related to the low temperature ($T < 450^oC$) annealing in an atmosphere containing hydrogen (forming gas) that is normally employed to electrically deactivate the dangling bonds on the grown oxide by passivation with hydrogen atoms. Irradiation with ionising particles breaks the passivated bonds, resulting in an increase of active defects in the oxide. This effect is enhanced by the detached hydrogen atoms which are very reactive and can destroy further defect-hydrogen-bonds [Kuh97]. If the defects are located directly at the $SiO_2 - Si-$interface, they can act as generation centers for surface generation current below the interface. An electron accumulation layer below the oxide can neutralize these interface states and thus prevent them from acting as current generation centers (figure 1.3).

Macroscopic effects of the radiation induced charge up in the oxide layer are a shift in the flat-band voltage (see section 5.2.14), an increase in the surface generation current (see section 5.2.15) and a decrease in the hole mobility at the $SiO_2 - Si-$interface (see section 5.2.16).

1.5.2 Displacement damage due to high energetic hadronic radiation

1.5.2.1 Change in N_{eff}

The effective doping concentration N_{eff} in a silicon device changes with hadronic irradiation. This change corresponds to a change in the depletion voltage V_{dep}, which is proportional to $|N_{eff}|$ according to equation (1.29).

The fluence of any hadronic irradiation can be scaled to the equivalent fluence ϕ_{eq} of neutrons with an energy of 1 MeV [Lin99].

For small fluences ($\phi_{eq} \approx 1 \cdot 10^{13}\,cm^{-2}$) the dominating process is the reaction of

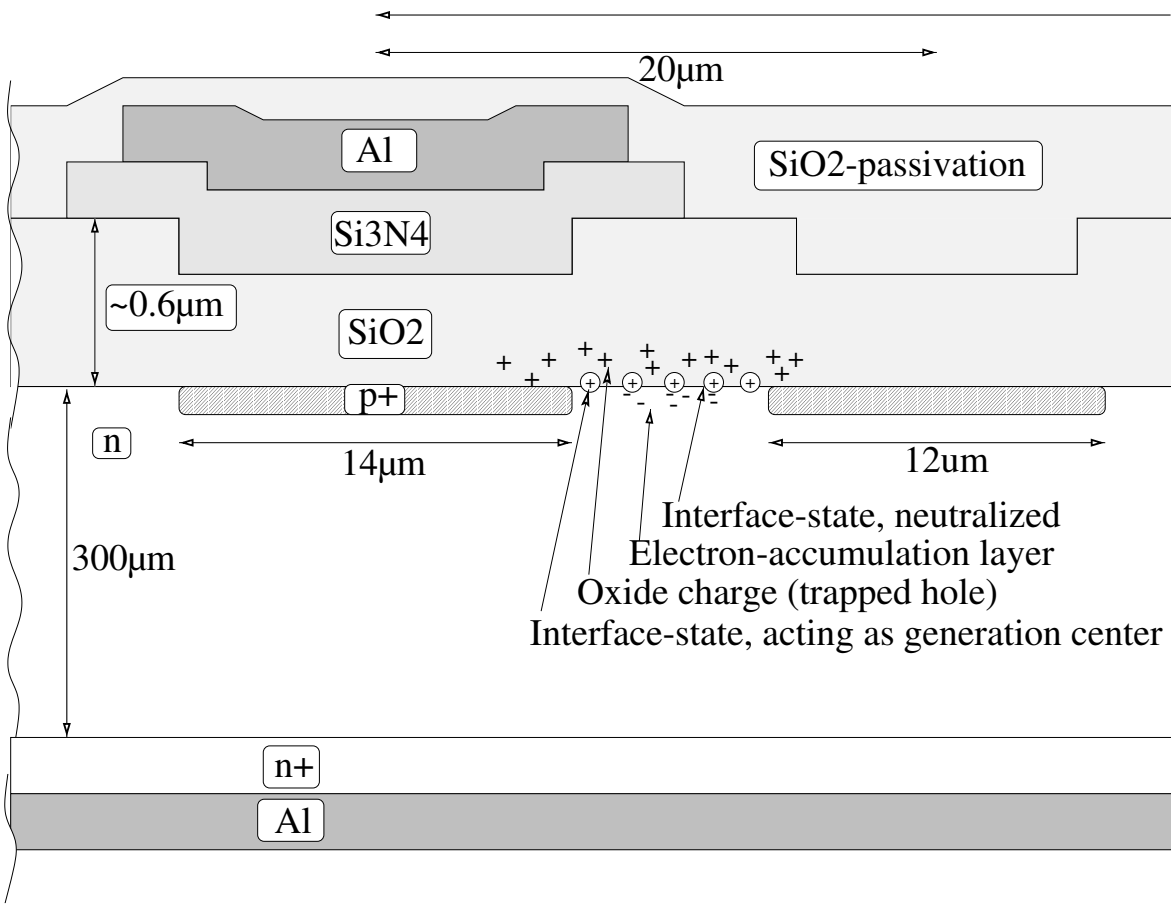

Figure 1.3: Oxide charges and current generation centers at the $SiO_2 - Si-$interface.

radiation induced vacancies and silicon interstitials with shallow donors (normally phosphorous) or acceptors (normally boron). Donors or acceptors which are incorporated in these defects are no longer available as doping atoms (*donor-/acceptor-removal*). Since the boron concentration is usually negligibly small [Mol99a], only the *donor removal* has to be taken into account. For higher fluences ($\phi_{eq} > 1 \cdot 10^{13}\, cm^{-2}$) the dominating radiation damage concerning N_{eff} is the formation of charged acceptors. Starting from n-type material the *donor-removal* and the acceptor creation finally lead to *type-inversion* resulting in p-type material.

The change in N_{eff} with hadronic irradiation is well described by a model which is based on the assumption that the concentration of donors decreases exponentially with ϕ_{eq} due to the *donor-removal* while at the same time acceptors are formed proportional to ϕ_{eq} [Lin99]. Fig. 1.4 shows $|N_{eff}|$ and V_{dep} as function of ϕ_{eq} as measured directly after irradiation.

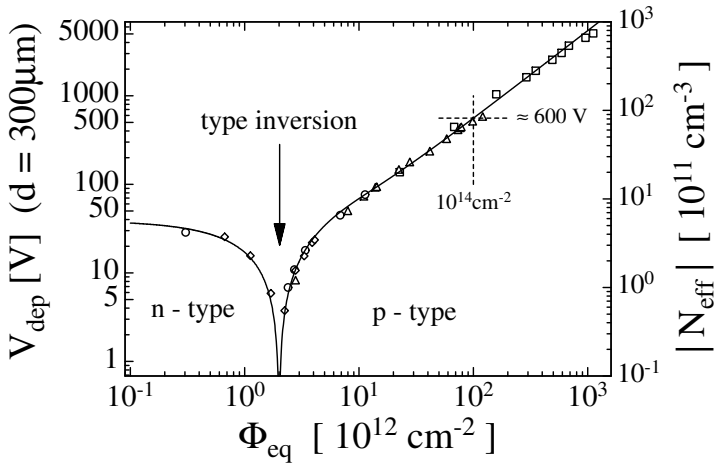

Figure 1.4: Change in the depletion voltage respectively the absolute doping concentration as measured immediately after irradiation [Wun92].

The radiation induced change in the effective doping concentration is not stable. Due to dissociation, recombination and forming of complex defects, $\Delta N_{eff} = N_{eff,0} - N_{eff}(t)$ decreases immediately after irradiation. In contrary to this short term *(beneficial-)annealing* an increase in ΔN_{eff} is observed within several years after the irradiation. This long term *reverse-annealing* can be explained by a model that describes transformation of neutral defects into negatively charged defects (acceptors) in the depletion region.

The experimental results on the change in N_{eff} after irradiation and annealing

processes are described by the following empirical formula:

$$\begin{aligned}\Delta N_{eff}(\phi_{eq},t) &= N_{eff,0} - N_{eff}(t) \\ &= N_C(\phi_{eq}) + N_a(\phi_{eq},t) + N_Y(\phi_{eq,t}) \\ &= N_{C0}(1-\exp(-c\phi_{eq})) + g_c\phi_{eq} + g_a\cdot\phi_{eq}\cdot\exp\left(-\frac{t}{\tau_a(T)}\right) \\ &\quad + g_Y\cdot\phi_{eq}\left(1-\frac{1}{1+t/\tau_Y(T)}\right). \end{aligned} \tag{1.36}$$

N_C denotes the stable damage component, N_a the *beneficial-annealing* component, and N_Y the *reverse-annealing* component. For the investigations in this work the parameters in formula 1.36 were taken from recent results on high resistivity material and are summarized in table 1.2.

parameter	value	reference
N_{C0}	$6.3\cdot10^{11}cm^{-3}$	[Mol99b]
c	$1.27\cdot10^{-13}cm^{-2}$	[Mol99b]
g_c	$1.52\cdot10^{-2}cm^{-1}$	[Mol99b]
g_a	$1.87\cdot10^{-2}cm^{-1}$	[Lin99]
$\tau_a(20^oC)$	$2\,days$	[Lin99]
g_Y	$5.16\cdot10^{-2}cm^{-1}$	[Lin99]
τ_Y	$475\,days$	[Mol99a]

Table 1.2: Values for parameters in formula (1.36). If available, only data for high resistivity n-type float zone material has been averaged.

1.5.2.2 Change in dark current

Irradiation with hadrons leads to an increase in the dark current. It is mainly caused by volume generation current and independent of the specific material. The number of radiation induced generation centers is proportional to the fluence:

$$\frac{\Delta I}{V} = \alpha(t,T)\cdot\phi_{eq} \tag{1.37}$$

For the dark current only a *beneficial annealing* after the irradiation is observed which is also independent of the specific material. The corresponding time dependence of α can be parametrized by one exponential and one logarithmic term[Mol99a]:

$$\alpha(t) = \alpha_I\cdot\exp\left(-\frac{t}{\tau_I}\right) + \alpha_0 - \beta\cdot\ln t/t_0. \tag{1.38}$$

A fit to the existing data for the annealing at room temperature ($T = 21^oC$) results in the following set of parameters:

$$\begin{aligned} \alpha_I &= 1.23 \cdot 10^{-17}\, A/cm \\ \tau_I &= 1.4 \cdot 10^4\, min \\ \alpha_0 &= 7.07 \cdot 10^{-17}\, A/cm \\ \beta &= 3.29 \cdot 10^{-18}\, A/cm \\ t_0 &= 1\, min \end{aligned}$$

For annealing times of 1 and 3 weeks this results in the following values:

$$\alpha(1\, week) = 4.64 \cdot 10^{-17}\, A/cm \tag{1.39}$$

$$\alpha(3\, week) = 3.81 \cdot 10^{-17}\, A/cm \tag{1.40}$$

Chapter 2

The Silicon Microvertex Detector (MVD) at ZEUS

2.1 The ZEUS detector at HERA

ZEUS is a general purpose detector system installed in the hadron electron ring collider (HERA) at DESY, Hamburg. HERA provides colliding beams of positrons or electrons ($E_{e^+} = 27.5GeV$) and protons ($E_p = 920GeV$). The corresponding center-of-mass energy is $E_{cms} = 318GeV$ [1]. Figure 2.1 shows the present layout of the ZEUS detector. The inner tracking detectors are measuring charged particles in a magnetic field of $1.43T$. The beam-pipe is surrounded by the central tracking detector (CTD). It consists of 72 cylindrical drift chamber layers which are divided into 9 superlayers. The angular coverage is $15^o < \theta < 164^o$ [2]. A high resolution depleted-uranium calorimeter is measuring the energy in the pseudorapidity region $-3.8 < \eta < 4.3$ [3]. A detailed description of the ZEUS detector system is given in [ZEU93].

During the 2000 shutdown HERA will be upgraded to allow high luminosity runs with a high sensitivity to low e-p cross section physics [Sch98]. A silicon microvertex detector (MVD) will be placed around the beam-pipe inside the CTD. It will improve the global precision of the tracking system and allow to identify events with secondary vertices originating from the decays of long-lived states ($ct \approx 100\mu m$) like hadrons with charm or bottom quarks or τ leptons. The present configuration of the ZEUS detector allows to study heavy flavour physics by other means (e.g. charm identification via D^* mesons reconstruction). However, due to the low efficiency of these methods, the analysis is still dominated by statistics. The MVD will allow to access high-purity and large statistics samples as shown in figure 2.2.

Some of the physics topics which are accessible with the MVD are [ZEU97]:

- *Charm in photoproduction.* From the rate of charm events in direct photoproduction the gluon content of the proton can be measured.

[1] Values for the 1998 data taking periode

[2] θ is the polar angle between the particle track and the proton beam line (z-axis)

[3] $\eta = -\log\tan(\theta/2)$

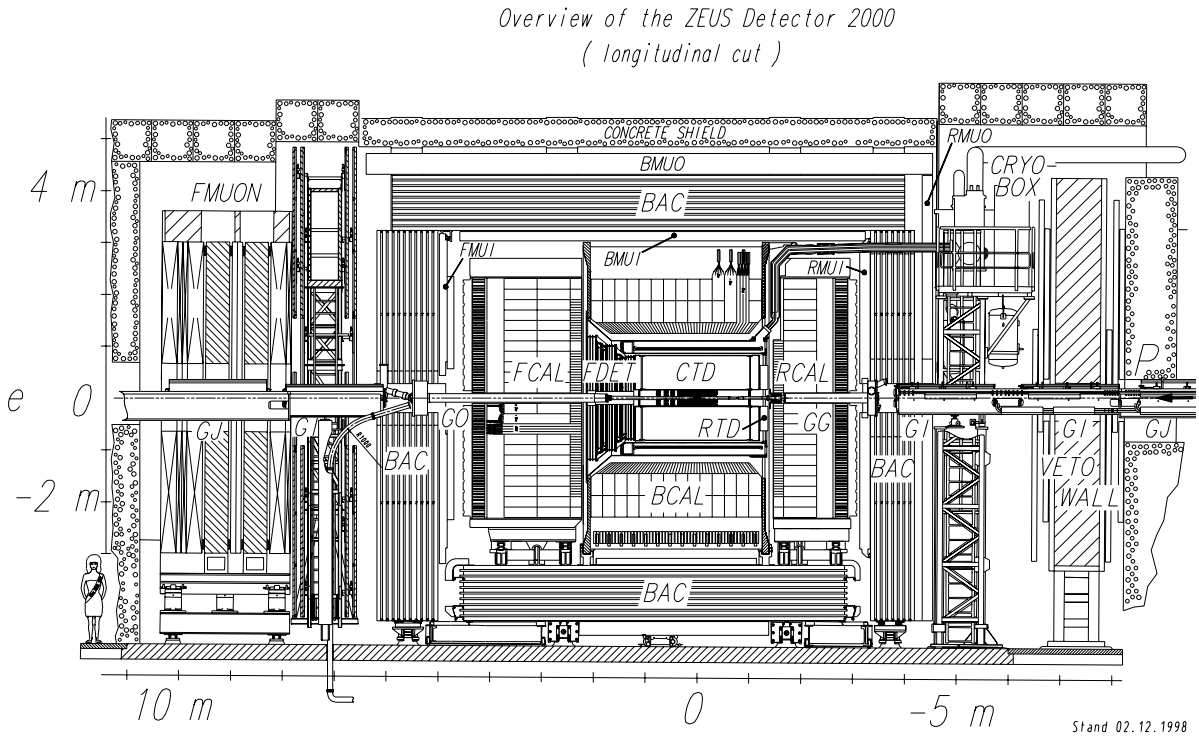

Figure 2.1: Longitudinal cut of the ZEUS detector after the luminosity upgrade.

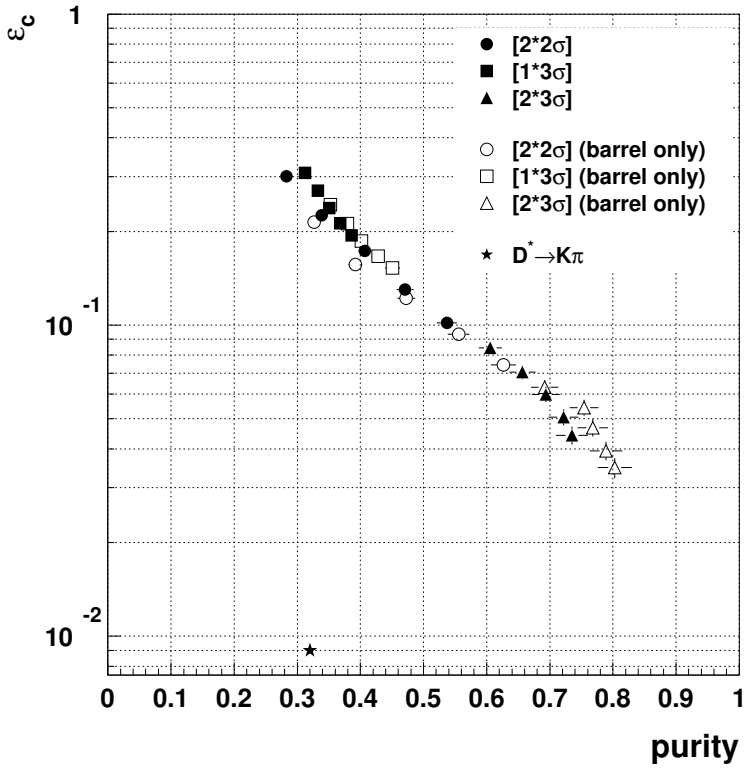

Figure 2.2: Purity versus efficiency for different selection criteria of charm in DIS using the MVD. The star shows the current values obtained with the ZEUS tracking system via D^* meson reconstruction.

- *Charm in Deep Inelastic Scattering (DIS).* In particular the measurement of the proton structure function F_2^{charm} will profit from an extension of the kinematic range with the MVD.
- *New physics.* The possibility to identify secondary vertex tracks and the improved resolution of the tracking system will provide a better understanding of the nature of the interaction (e.g. very high Q^2 electrons are scattered in the forward direction).

2.2 Requirements for the MVD

During the design of the MVD the following requirements have been specified:

- Angular coverage of the region $10^o < \theta < 160^o$ around the interaction point (IP).
- Measurement of three points per track, in two projections each.
- $< 20\mu$m intrinsic hit resolution.
- Two track separation down to 240 μm.
- Physical space available is limited by the inner volume of the CTD ($r = 16$ cm), and by the beam pipe volume.
- Radiation hardness up to an integrated dose of $3kGy$ within the foreseen operation time of 5 years (see section 2.4).

2.3 Layout of the MVD detector system

According to the specifications, the MVD has been split into a central (BMVD) and a forward (FMVD) detector, requiring a good matching with the existing detectors (see figure 2.3).

2.3.1 BMVD layout

The length of the barrel section ($622mm$), is dictated by the longitudinal distribution of the interaction region, which is dominated at HERA by the length of the proton beam bunch. A cross section of the BMVD in the $r - \phi$ plane is shown in fig. 2.4. Three layers with 600 detector modules altogether have been chosen for high efficiency of pattern recognition and to allow an estimation of the momentum of the tracks in the trigger. The first layer of detectors, placed at r = 3 − 5 cm from the CTD axis, follows the elliptical shape of the beam-pipe. The second and third layers are placed around a circle at r ≈8.6 cm and r ≈12.3 cm. Note that the beam-pipe is not centered with respect to the CTD axis and that the nominal IP is shifted towards the HERA center (increasing x values), of about 4 mm. The beam-pipe shape and the beam

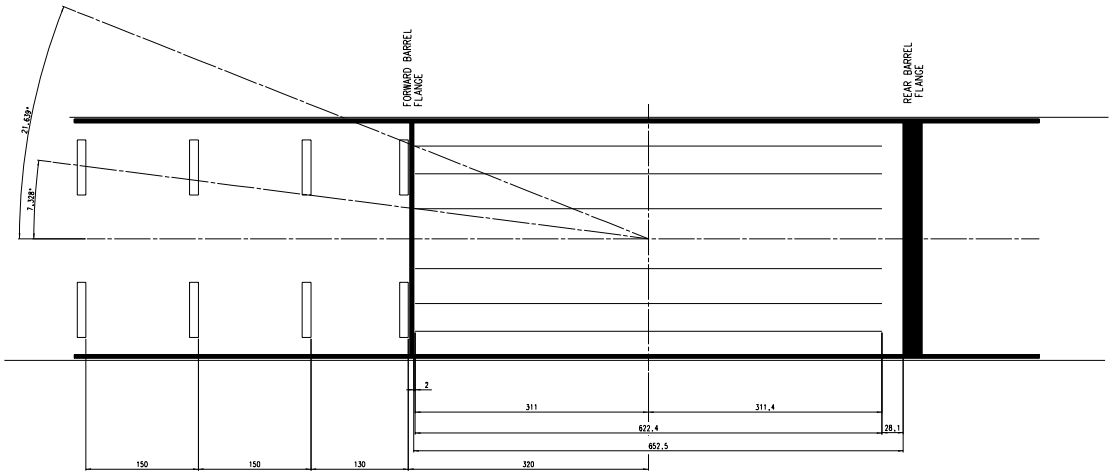

Figure 2.3: Layout of the MVD along the beam line (horizontal and vertical scale are different, all dimensions in mm).

optics are the result of optimisation studies on background in the interaction region. The greatest contributions are direct and back-scattered syncrotron radiation of the electron beam[4][Sch98].

2.3.2 BMVD ladders

Two quadratic silicon strip detectors are arranged in a halfmodule with strips parallel and perpendicular to the beam line ($r-\phi$ and $r-z$ plane, see figure 2.5). Both detectors are electrically connected via a Kapton® foil of triangular shape. The resulting readout area is approximately $120 \cdot 60 mm^2$. A small overlap minimizes the dead area of the cell. An additional Kapton® fanout connects the strips to the frontend electronics, where both detectors are read out together. Two halfmodules are placed on top of each other, forming a readout module of 1024 channels. In this way a track traversing the module can be reconstructed in two dimensions. Five readout modules are placed on a support ladder (figure 2.6). The Kapton® fanout is bent around the edge of the ladder and the hybrid with the frontend electronics is positioned on top of the detector. The ladders consist of carbon fiber and besides supporting the detectors and frontend electronics provide the cooling for the readout chips. Prototype ladders have been built and tested. They proved to be light ($\approx 70g$) and rigid (deflection $\approx 45\mu m$ for $220g$ weight, flatness $\leq 100\mu m$).

[4]With respect to the current beam optics. For the high lumi running the separation of the two beams occurs close to the IP.

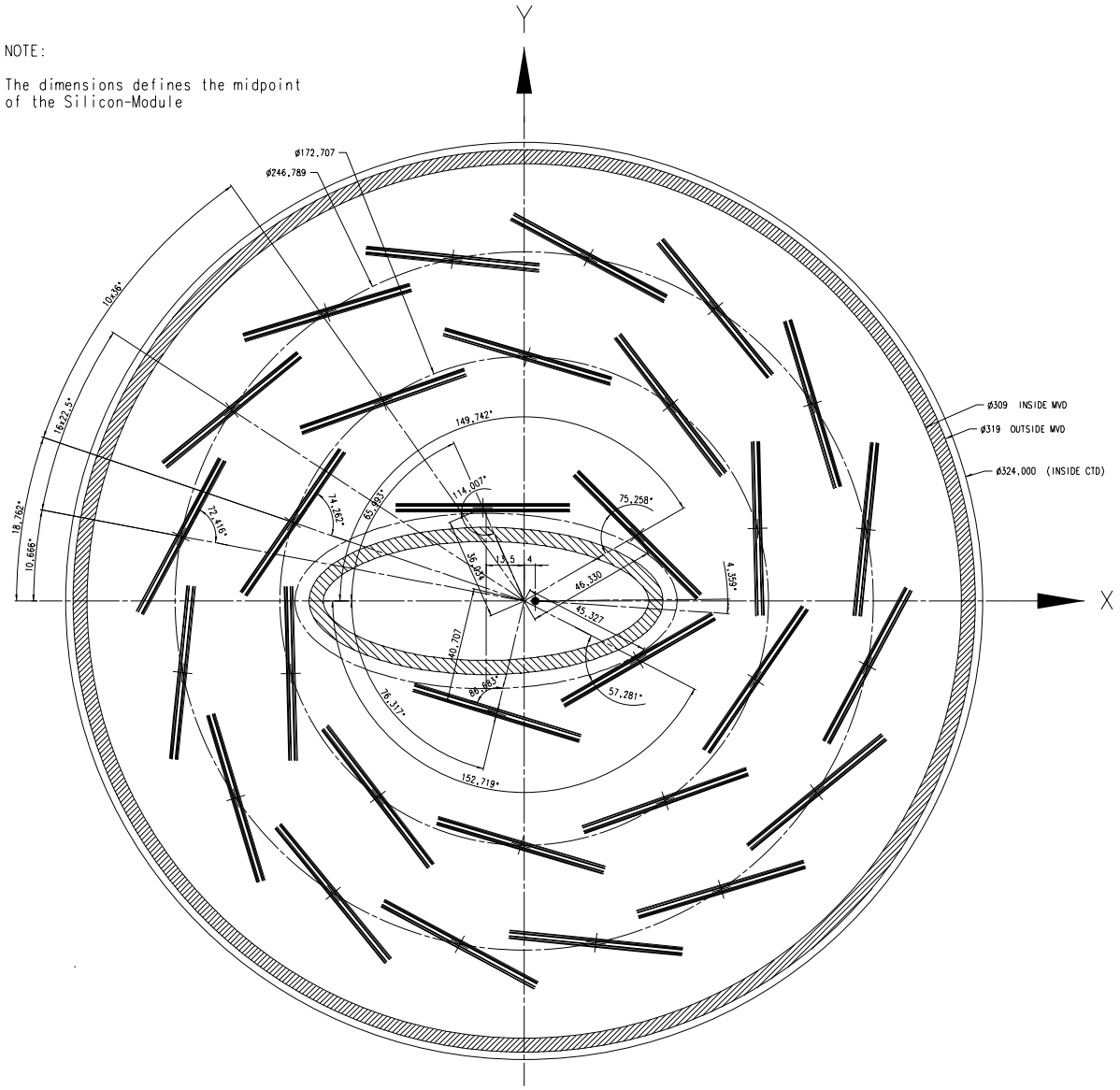

Figure 2.4: BMVD cross section in the $r-\phi$ plane. The silicon sensors are surrounding the beam pipe in three layers.

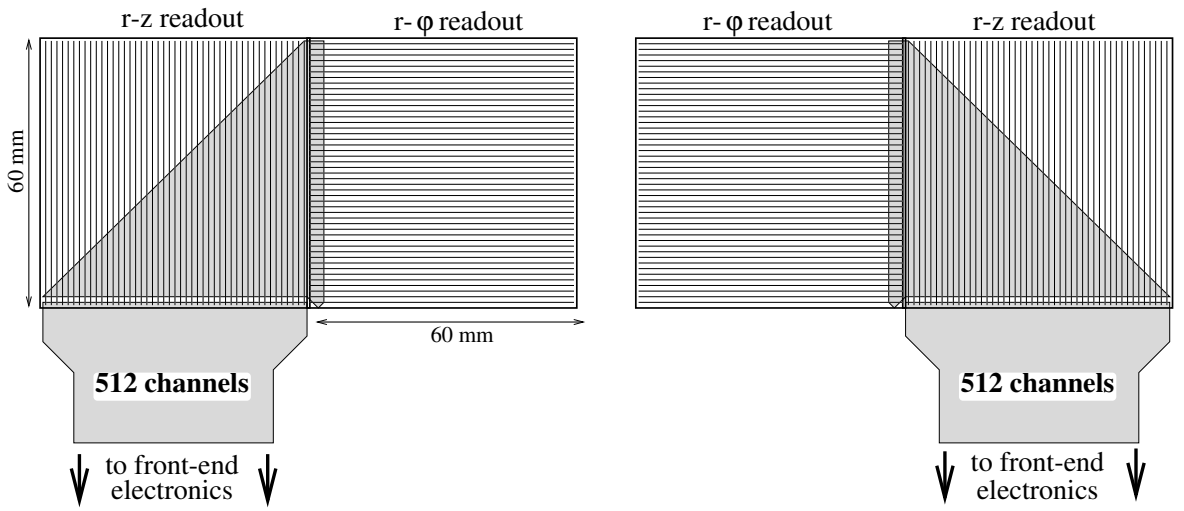

Figure 2.5: BMVD readout cell.

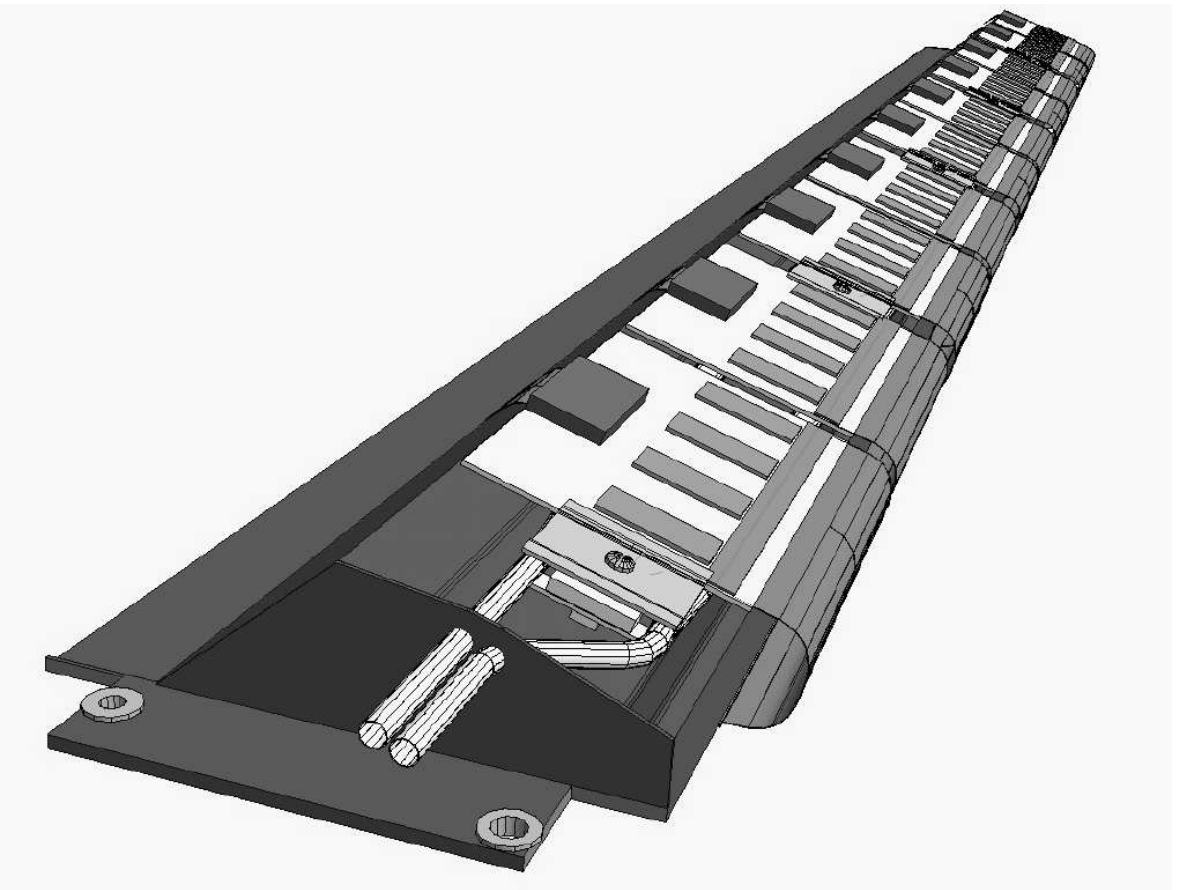

Figure 2.6: Layout of a ladder with five modules.

2.3.3 FMVD layout

The forward vertex detector consists of 112 silicon modules which are arranged in wheels. It extends to a pseudorapidity of $\eta = 2.6$. The wheels provide essential tracking and vertexing information in regions which are not covered by the existing tracking system. A wheel is made of two layers of 14 silicon planes. The planes are of the same type as the barrel sensors but with a "wedge" shape, two sides being parallel and two tilted by 13 degree in opposite directions. One plane incorporates 480 readout strips. Figure 2.7 shows a cross section of a forward wheel. By using two overlapping planes with strips oriented along the two tilted edges, one wheel provides r and ϕ coordinates per track (see figure 2.7). A small overlap between adjacent detectors in a layer is

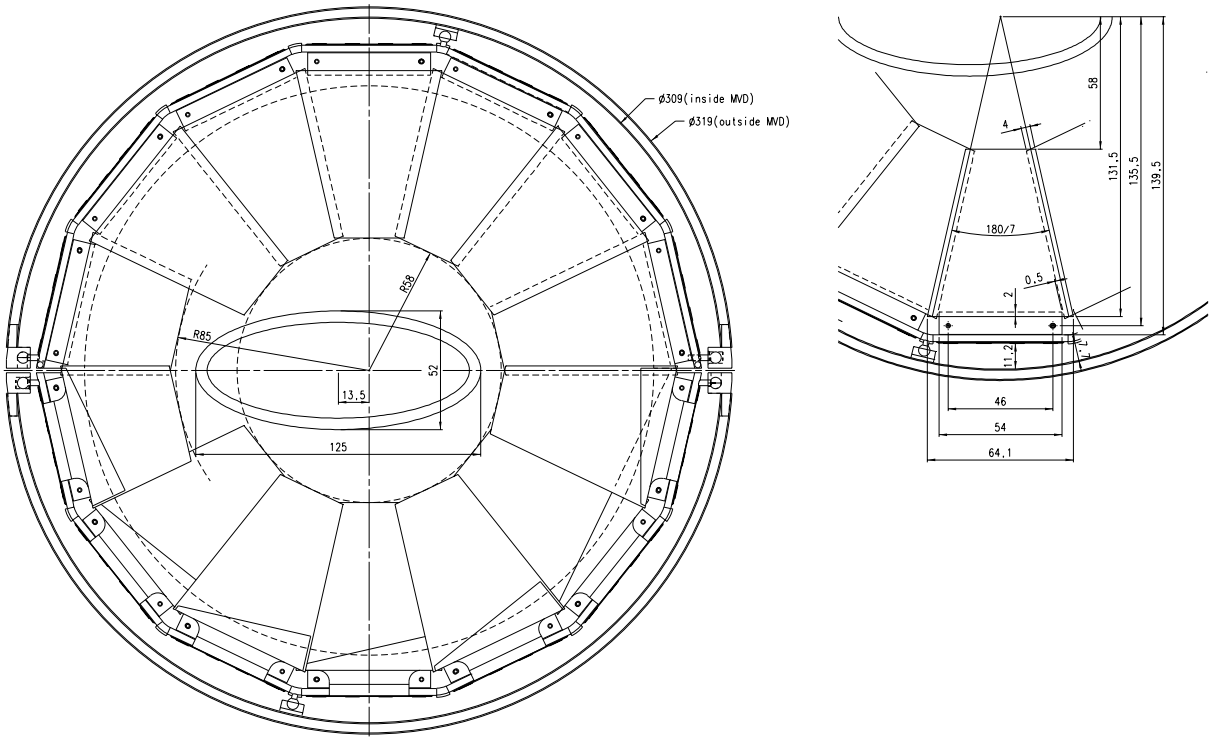

Figure 2.7: Arrangement of detectors in a forward wheel.

used in order to minimize dead regions and to allow a relative alignment. The four wheels are positioned at $z = 32, 45, 60$ and $75cm$ and the first wheel is mechanically attached to the barrel support structure. In order to optimize the space around the beam-pipe, two detectors with different dimensions have been designed. As for the BMVD, a Kapton® foil connects the readout strips with the frontend chips (see figure 2.8). Each detector is read separately using the same hybrid structure as for the barrel section.

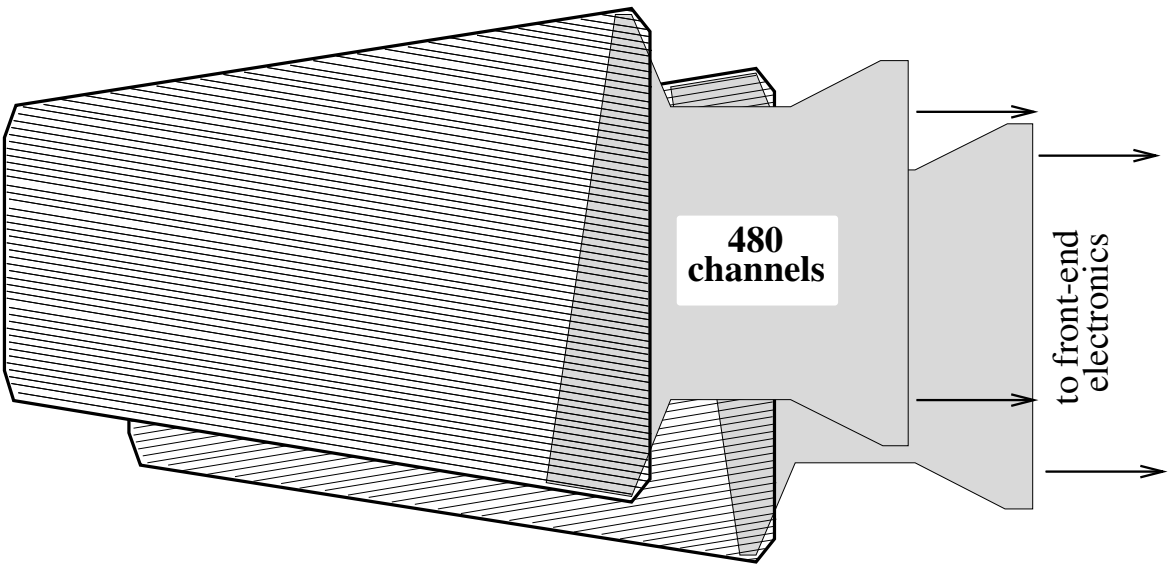

Figure 2.8: FMVD readout cell.

2.4 Radiation monitoring

The estimated operation time of the MVD in HERA is at least 5 years. During this time an integrated radiation dose of up to $0.5kGy$ is expected. The MVD detectors including the readout are designed to stand an integrated dose up to at least $3kGy$.

Main sources of radiation in the MVD area are the background from synchrotron radiation during normal operation and radiation due to beam losses.

For the background radiation backscattering, edge scattering and reflections at the absorbers close to the ZEUS interaction region of HERA can be distinguished. The expected dose from these radiation sources depends strongly on the exact geometry of all material in this region. Also bremsstrahlung due to the residual gas in the beam pipe is an additional source of background radiation. Its contribution depends on the quality of the vacuum in the beam pipe. In order to minimize these sources of radiation simulations have been performed [Sch98]. The total dose during normal operation is expected to be in the order of $50Gy$ per year as it was measured close to the H1 vertex detector in 1996 [Eic98].

Radiation due to an accidental loss of the positron beam occurs within a very short time ($msec$). Since there is no electron dump in HERA, the beam dump occurs in regions of minimum machine apertures (i.e. close to the experiments). It can reach doses of $10kGy$ per year as it was observed by the TLDs in both 1995 and 1996 [ZEU97]. In order to avoid such unpredictable and unacceptable high doses of radiation, a fast electron beam dumping system will be provided for the luminosity upgrade. It will allow all experiments to dump the electron beam via an interlock within few revolutions. For ZEUS a radiation monitoring system which is based on experiences of the OPAL radiation monitoring system [CER97] is under developement. It will use PIN diodes of

$10x10\ mm^2$ which are located close to the MVD area.

2.5 Readout electronics

The MVD silicon detectors are readout by HELIX [FR97], an analog chip initially designed by the ASIC laboratory in Heidelberg and manufactured in the 0.8 μm CMOS process by AMS. The HELIX 2.2 [Rie98] version, specifically designed for the HERA-B experiment, is currently used for the MVD prototypes. The HELIX 3.0, with design contributions from ZEUS, will be used in the final production. Figure 2.9 shows a schematic of the HELIX 2.1, which is still valid also for the current version 2.2. The

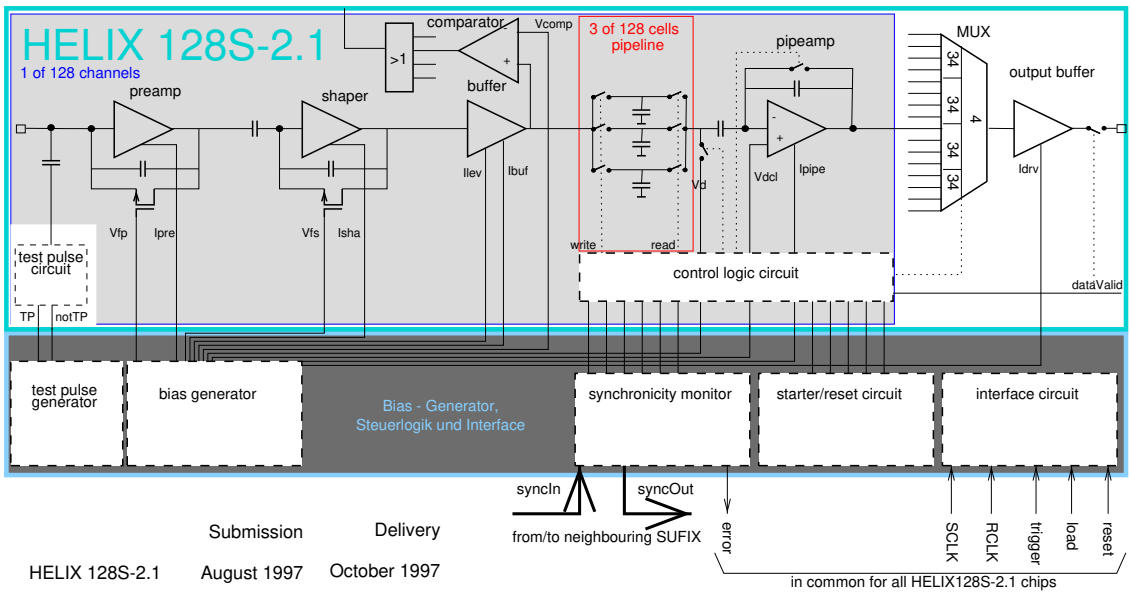

Figure 2.9: Circuit of the HELIX 2.1 analog readout chip.

chip integrates 128 channels with a charge sensitive amplifier/shaper; the signals are then sampled in an analog pipeline with a maximum latency of 128 sampling intervals. The chip has an additional amplifier per channel which is used to read the pipeline and is followed by a multiplexer and a buffer used to transfer the data on a serial bus. An important feature of HELIX is the capability to synchronize the data transfer of 4 chips on the serial bus using a daisy-chain mechanism; the first chip of the chain sends a token to the next chip after having transmitted all the data. The token moves on the chain and is sent back by the last chip through the chain until it reaches the first chip which generated it. The HELIX 3.0 chip will implement a failsafe token which will allow to exclude a bad chip from the readout chain, without hindering the functioning of the remaining chips of the chain.

The measured noise figure for the HELIX chip is

$$\mathrm{ENC}[e] = 340 + 40 * C[\mathrm{pF}], \tag{2.1}$$

where C denotes the input capacitance of one channel as seen from the preamplifier.

The signal from the HELIX chip is transferred via an analog link to the ADC cards about $10m$ away from the detector hybrids. The ADC perform the pedestal and common mode subtraction and a first cluster reconstruction. The signal is then transferred to the MVD second level trigger processors and to the ZEUS event builder.

Chapter 3

Design of the MVD detector modules

3.1 Layout of the BMVD detector modules

The strip detectors are single sided, made of high-resistivity ($\approx 5k\Omega cm$) n-type silicon. The thickness is about $330\mu m$[1], the overall dimensions are $64mm \cdot 64mm$. The backplane is n^+ doped and aluminized. Figure 3.1 shows a corner of a BMVD detector module. The front side is covered by 3082 p^+ doped strips. Every sixth strip is read out AC coupled by an aluminum strip on top of the p^+ strips. The width of the intermediate strips is $12\mu m$. The 514 readout strips are $14\mu m$ wide. The strip pitch is $20\mu m$, the readout strip pitch $120\mu m$. The aluminum readout strips are about $14\mu m$ wide and AC coupled to the p^+ readout strip by a double layer of Si_3N_4 and SiO_2 of approximately $250nm$ thickness. All p^+ strips are biased using poly silicon resistors which alternately connect even and odd strips to either side of the two bias lines located perpendicular to the strips close to the detector edges. The first and last readout strip are connected directly to the bias lines, completing the bias ring around the active area. Three guard rings surround the bias ring. Beyond the last guard ring an n^+ doped ring is placed, which extends through the bulk volume down to the backplane. It allows to bias the backplane with a contact from top. The active area of the detector is about $61.7mm \cdot 62.5mm = 38.6\,cm^2$. The area covered by guard rings is about $0.7\,cm^2$.

Capacitive charge division between the readout strips is used in order to limit the number of readout channels and to achieve a spatial resolution of $10\mu m$ for minimum ionizing particles traversing the detector with angles up to 30^o with respect to the detector. Due to the capacitive coupling between neighbouring strips, the charge collected at intermediate strips induces charges on the readout strips. The charge collected on the readout strips is approximately inversely proportional to the distance between interpolating and readout strip [Koe85]. To achieve uniformity in charge collection all

[1]This value has been obtained from mechanical measurements on prototype detectors. The specified value for the thickness was $300\mu m$.

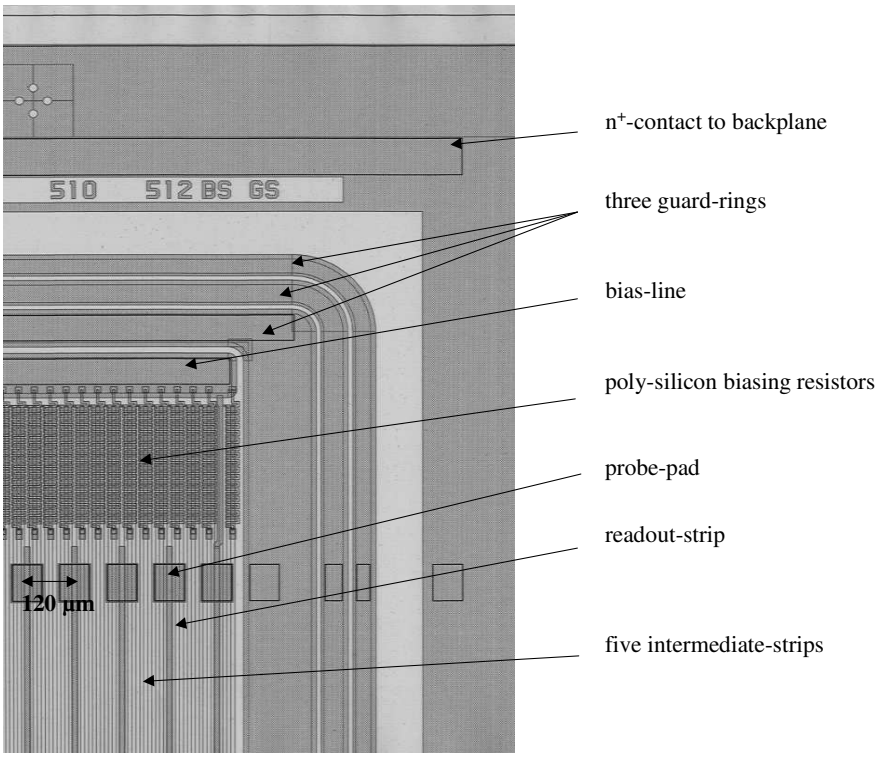

Figure 3.1: Mask of one corner of a BMVD detector module.

strips have to be kept at the same potential.

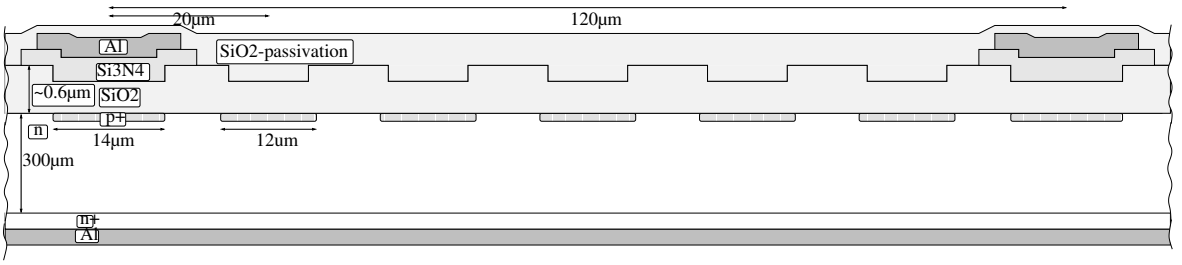

Figure 3.2: Cross section of MVD detector module with two readout strips.

The technology of the FMVD modules is the same as for the BMVD. Only the "wedge" shape and the number of 480 readout channels per detector are different.

3.2 Design of the test structures

Not all specifications and technological parameters can be measured directly on the detectors. Therefore special test-structures have been designed. For each detector there will be one test-structure from the same waver which has passed the same production steps as the corresponding detector. Besides giving access to technological parameters that cannot be measured on the detectors themselves, this concept also allows to repeat measurements after assembly and installation of the detector system. At this stage the detectors are no longer accessible for most of the electrical measurements. Also tentative critical measurements that might destroy a detector irreversibly can be performed on the test-structures.

Figure 3.3 shows a photo of a test-structure. In this chapter only a brief introduction in the test-structures will be presented. In section 5.2 the individual structures will be explained in detail with the measurements that are performed on them. The following structures are implemented and used for measurements:

- *Poly-silicon resistors.* 10 poly-silicon resistors on each test structure allow to directly measure the value of the biasing resistors.

- p^+ *fingerstrips.* Each of the two fingerstrip structures consists of two neighbouring p^+ strips in a meander-like shape with a total strip length of $54mm$. The p^+ strips are covered by aluminum strips with the same width and coupling layer below as on the detector. The two different fingerstrip structures have a p^+-strip width of $12\mu m$ (W12) and of $14\mu m$ (W14). The strip pitch is $8\mu m$ (W12) and $6\mu m$ (W14). p^+ and aluminum strip are accessible with prober contacts on both sides. The structure has been used to measure the resistance between neighbouring p^+ strips, which are not accessible from outside on the detector. Other parameters that could be measured on the fingerstrips are the p^+ and aluminum resistivity. Also interstrip capacitance measurements can be performed on the fingerstrips.

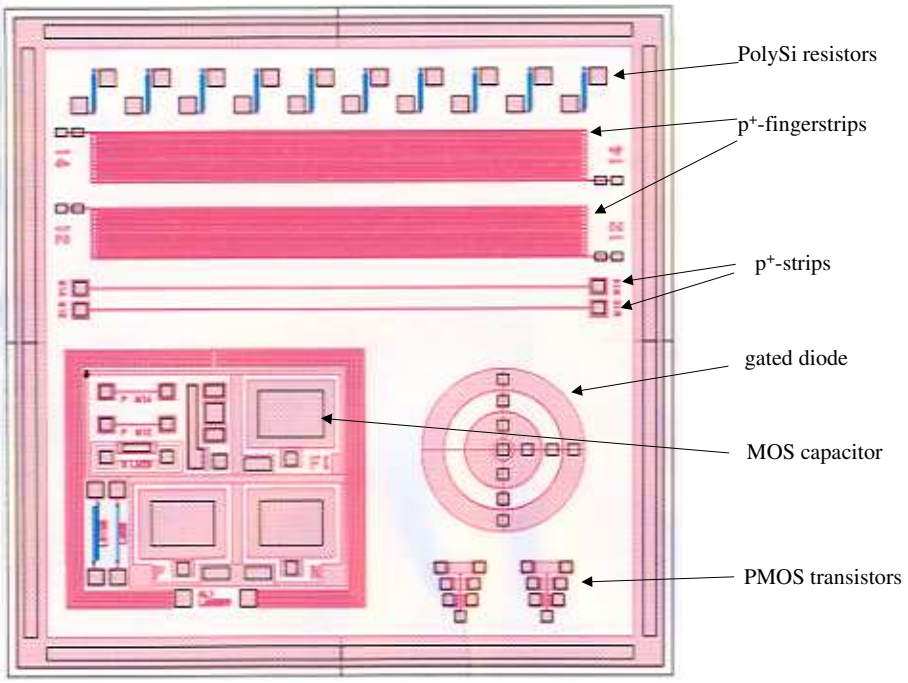

Figure 3.3: Layout of a part of the test structures. The PAD diode is not shown.

But due to the different geometry the results are different to the situation in the detector.

- p^+ *strips.* Two separated p^+ strips with $12\mu m$ (W12) and $14\mu m$ (W14) strip width and a length of $4600\mu m$ each allow to measure the resistivity of the p^+ implant for readout (W14) and intermediate (W12) strips.

- *Gated diode.* The gate controlled diode is a standard component for the investigation of surface effects on $p-n$ junctions [Gro67]. For the MVD test structures a design with two gates and one guard ring has been chosen. In this work it has been used to investigate the surface generation current before and after $\gamma-$irradiation. Also the flatband voltage has been determined from the gated diode measurements.

- *MOS*[2] *capacitor.* With the MOS capacitor the characteristics of the coupling oxide layer can be investigated [Gro67]. Besides the measurement of the oxide thickness it has been used to determine the flatband voltage from which the amount of positive oxide- and interface charges has been calculated.

- *Pad diode.* The pad diode consists of a p^+ pad ($3.6mm \cdot 3.6mm$) on top of the silicon bulk and three guard rings around the active area. It allows to study the characteristic of the $p-n-$ junction with reduced edge effects from the SiO_2 region compared to the strip detector. For this work it has not been used.

- *PMOS transistor.* The PMOS transistor is a surface field-effect transistor. It has been used to extract the threshold voltage, which corresponds to the flatband voltage, and to determine the mobility of holes in the interface area below the oxide. Also the gated diode has been used as a PMOS transistor.

[2]MOS = metal oxide semiconductor

Chapter 4

Test beam measurements

4.1 Test beam setup

In order to understand and verify the performance of the detectors and the readout electronics, a test beam has been setup. Figure 4.1(a) shows a sketch of the setup. Prototype detectors assembled with the readout electronics are being exposed to a low energy electron beam ($2 - 6\,GeV$) of the DESY II accelerator. The tracks of charged particles are measured by three pairs of reference detectors providing x and y coordinates in the plane perpendicular to the beam which defines the z-axis. The reference detectors are strip detectors with $50\,\mu m$ readout pitch and one intermediate strip. The device under test (DUT) can be moved laterally and rotated, in order to select tracks with a specific incident angle.

The accuracy in predicting the coordinates of the track is determined by the intrinsic resolution of the reference detectors and by multiple scattering. It has been measured as $\sigma_t = 5.4\mu m$ for a $6\,GeV$ electron beam (figure 4.1(b)).

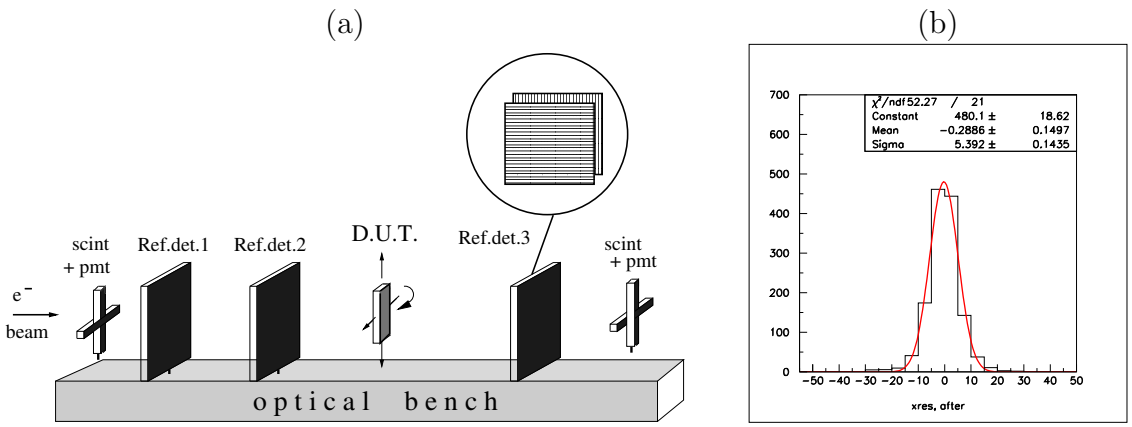

Figure 4.1: (a) Test beam setup. (b) Measured accuracy in predicting the coordinate of the track on the DUT for a 6 GeV electron beam.

4.2 Test beam results

The test beam setup has been succesfully used to characterize the performance of the BMVD prototype detectors for minimum ionizing charged particles. The most important results are:

- A signal to noise ratio of $S/N \approx 22$ has been achieved for the prototype readout electronics (HELIX 128 V2.2) coupled to a single BMVD detector. The noise level is distributed uniformly over the strips.
- The measured efficiency is very high ($> 99.8\%$).
- Gain variations within single HELIX readout chips are in the order of 2%.
- The position resolution of the detector modules at normal incidence is $\sigma_i < 7.5\mu m$.
- The resolution as function of the incident angle is in fair agreement with first results from a detector simulation.
- A detector which was $\gamma-$irradiated with $2.8kGy$ at $100V$ bias voltage has been mounted in the test beam. No deterioration in the performance has been observed so far. Final results are expected soon.
- The installation of a detector in the test beam which was neutron irradiated with $\phi_{eq} = 1 \cdot 10^{13} cm^{-2}$ is under way.

Chapter 5

Electrical measurements

5.1 Test setup

5.1.1 Probe station

A Suss-PM5-probe station [Sus] has been used for contacting unbonded detectors and test structures. The prober is located in a black aluminum box which provides both electric shielding and light tightness. It consists of a stainless steel chuck, up to 10 micropositioners which are fixed on one of the two platforms on the left and right, a stereo microscope Zeiss Olympus SZ40 and a vacuum system.

The device under test (DUT) is fixed on the chuck by vacuum. The chuck can be moved manually in the x- and y-direction. The DUT can be viewed with the stereo microscope.

Suss-prober needles [Sus] with a conical shape (7μm diameter tip) are used for contacting the DUT. They can be moved in all 3 dimensions and the force applied to the surface of the DUT is controlled by a spring mechanics.

A PT100 thermo-resistor is fixed close to the chuck in order to monitor the temperature of the DUT during electrical measurements.

The chuck and all prober needles are connected to coaxial cables which provide electrical connection to external devices. The PT100 is connected to an external multimeter by 4 unshielded wires.

5.1.2 Electrical setup for I/V and C/V measurements

Fig. 5.1 shows a scheme of the standard measurement setup used for I/V and C/V measurements.

A combined voltage source and pico-amperemeter Keithley 487 is used to bias the DUT during I/V and C/V measurements. For I/V measurements it also reads the resulting current. It can provide voltages from $-500V$ to $+500V$ with a maximum current of $2mA$ and measures currents up to $2mA$. The resolution is $10fA$ in the $2nA$ range and $1nA$ in the $2mA$ range.

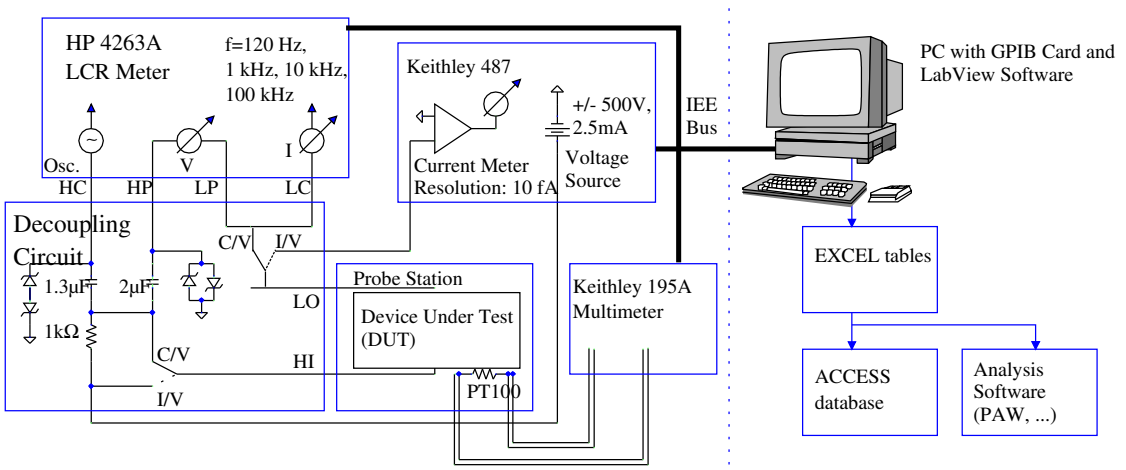

Figure 5.1: standard electrical setup used for I/V and C/V measurements.

For the standard C/V measurements a Hewlett Packard 4263A LCR meter is used. Possible measurement frequencies are $120Hz$, $1kHz$, $10kHz$ and $100kHz$. The resolution is $1fF$ at $f = 10kHz$. Another LCR meter Hewlett Packard 4192A was used for investigating frequency dependencies in detail. It can measure over a continous frequency range from $5Hz$ to $13MHz$. The resolution is $10fF$ at $f = 10kHz$.

The measurement principle of an LCR meter is explained in appendix A.

For measuring devices which are externally biased, an additional decoupling circuit is used to protect the input of the LCR meters.

Since all dark currents are strongly temperature dependent (see section 1.4), the temperature is monitored using a PT100 thermo-resistor which is located close to the DUT inside the prober box.

The PT100 thermo-resistor is measured by a Keithley Multimeter 195A. The accuracy of the displayed temperature is about $\pm 0.5^oC$ at room temperature.

Ground loops in the setup would be a source of noise. Long cables can lead to a pick-up of noise [Kei98]. To suppress both types of noise, all devices are located close to each other and connected to the same power line.

All power supplies and measurement devices are connected to a GPIB Board in a PC via an IEEE bus. On the PC LabView-programs are used to control and readout the connected devices. All settings and results are stored directly in EXCEL sheets which are then used for further analysis and as an interface to an ACCESS database system.

5.1.3 Long-term I/V measurements

In order to test the long-term stability of the BMVD prototype detectors, 8 of them were bonded in support structures and kept under continous bias for several weeks.

Fig 5.2 shows a sketch of the setup. The support structures with the bonded detectors on top are located in a black box. All detectors are connected to the same power supply (Heinzinger HN 1200). The backplane contact is made from the n^+ bond pad on top. Bias ring and first guard ring are grounded via protection resistors. The bias and guard leakage currents are determined by measuring the voltage drop $V_{R_{bias}}$ and $V_{R_{guard}}$ over the corresponding protection resistors with a Keithley 2001 Multimeter. The temperature is measured with a Testoterm 1100 thermometer through a hole in the box. All measurements are taken manually and recorded in an EXCEL data sheet.

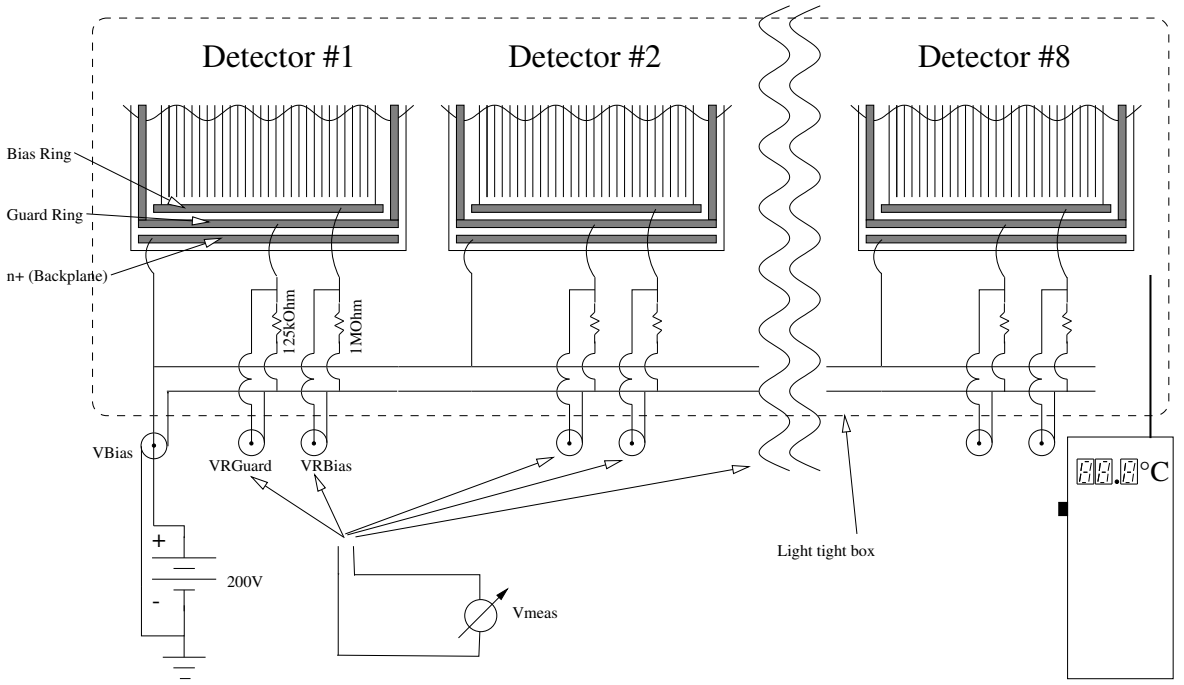

Figure 5.2: Sketch of long-term I/V measurement setup.

5.1.4 $\gamma-$irradiation

Low energy $\gamma-$irradiations with $^{60}Co-$sources ($E_\gamma \approx 1.2MeV$) have been performed at 2 different irradiation facilities:

- *Floating irradiation.* One detector and its corresponding test structure have been sent to the National Institute of Measurements (Nederlands Meet Instituut) at Utrecht, Netherlands. Using a $^{60}Co-$point source they were irradiated floating, i.e. without bias voltage applied. In 2 runs, each about 16 hours at constant dose-rate of $62.5Gy/hour$, an estimated total dose of $2kGy$ was received. With various apertures and collimators a homogenous dose over the detector- and test-structure-area at a distance of about $1m$ from the source has been obtained. I/V measurements of the detectors leakage current have been performed at different annealing times after the irradiation, starting 8 hours after the second irradiation.

- *Irradiation under bias.* One detector has been irradiated using a $^{60}Co-$source at the Hahn-Meitner-Institut in Berlin. During irradiation it was surrounded by several ^{60}Co sources producing a homogenous radiation field with respect to the detector area. The dose-rate was $150Gy/hour$. The detector was bonded in a support structure. During irradiation it has been kept under a bias voltage of $100V$. The total dose was $2.90kGy$ in seven steps. The photo-current has been measured during the irradiation. After each irradiation step an I/V curve of the total leakage current of the detector has been taken. A test-structure has been irradiated together with the detector, but floating. In a second iteration eight test-structures have been irradiated at the same irradiation facility. Four of them were biased during irradiation with $+100V$ applied to the backplane and all contacts on top grounded. The other four test-structures were irradiated floating. The total dose for two of the biased test-structures was $50Gy$. The total dose for the other six test-structures was $2.8kGy$. For all irradiated detectors and test-structures the annealing has been studied by performing a set of measurements at several points of time after the irradiation.

5.1.5 Neutron-irradiation

One detector and its corresponding test-structure were sent for irradiation with neutrons to a reactor in Ljubljana, Slowenia [LJU]. During irradiation both were floating. The energy spectrum of the reactor neutrons ranges from thermal energies up to about $10MeV$ with a maximum at about $1MeV$. The detector was exposed to a fluence of $\phi_{eq} = 1 \cdot 10^{13} cm^{-2}$ in a single irradiation step[1].

The annealing after the irradiation has been studied by performing I/V and C/V measurements on the detector and on the test-structure at different times, starting 7 days after the irradiation.

5.2 Measurement results

In the sections below the relation between the detector performance and the values of electrical specifications is discussed in detail, and the specified values are compared with the measurement results. At the end of this chapter a summary table of the specified and measured values is given.

5.2.1 Total bulk capacitance C_{bulk}

The total bulk capacitance of the detector depends both on geometrical and electrical properties as one can see from equations 1.27 and 1.28.

For measuring the total bulk capacitance of the prototype detectors, the setup shown in fig. 5.3 was used. The first guard ring was grounded and the bias voltage was

[1] ϕ_{eq} is defined in section 1.5.2

applied between the detector backplane (HI) and the bias ring (LO). Using the decoupling circuit shown in figure 5.1, the capacitance between HI and LO was measured and recorded in the parallel mode of the LCR meter.

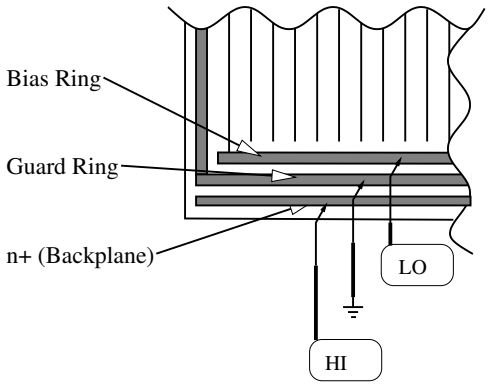

Figure 5.3: Setup used for measuring the total bulk capacitance of the detector.

For the capacitance at bias voltages above full depletion a value of about

$$C_{dep} = 1.34nF$$

was measured for all detectors at the default measurement frequency of $f = 1kHz$ (fig. 5.4). This result is close to the values measured by the manufacturer:

$$C_{dep,manuf.} = 1.31nF.$$

The geometric capacitance of the whole active area yields in agreement with these measurement results

$$C_{geom} = \epsilon_{Si}\frac{A}{d} = 11.9 \cdot 8.854 \cdot 10^{-14}\frac{F}{cm}\frac{6.17cm \cdot 6.25cm}{0.033cm} = 1.23nF. \qquad (5.1)$$

5.2.1.1 Frequency dependence of C_{bulk}

For all capacitance measurements on the detectors a frequency dependence of the resulting capacitances was observed. It can be attributed to the equivalent circuit of a detector that is never matched exactly by one of the display modes of the LCR meter (see appendix A). This work is focussing on the extraction of technological parameters from the measurement results. Not all frequency dependencies that were found have been understood or investigated further.

One of the measurements for which the frequency dependence was investigated further, but not understood completely, was the total bulk capacitance C_{bulk}. Fig. 5.5 shows measurements at different frequencies.

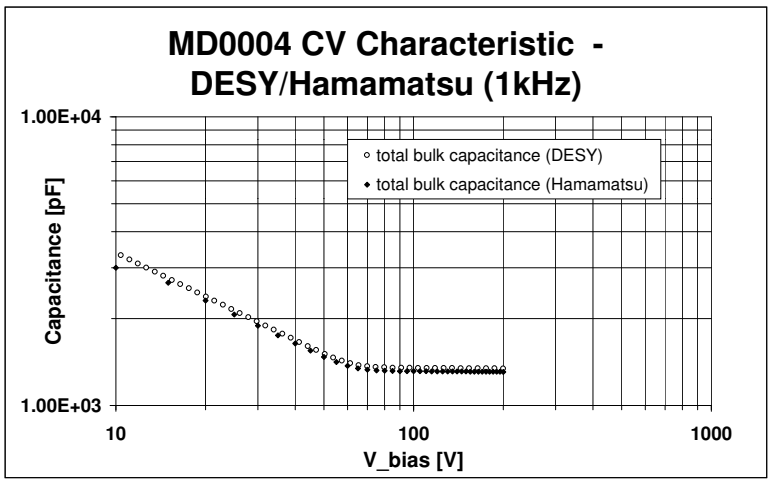

Figure 5.4: Total bulk capacitance as function of applied bias voltage.

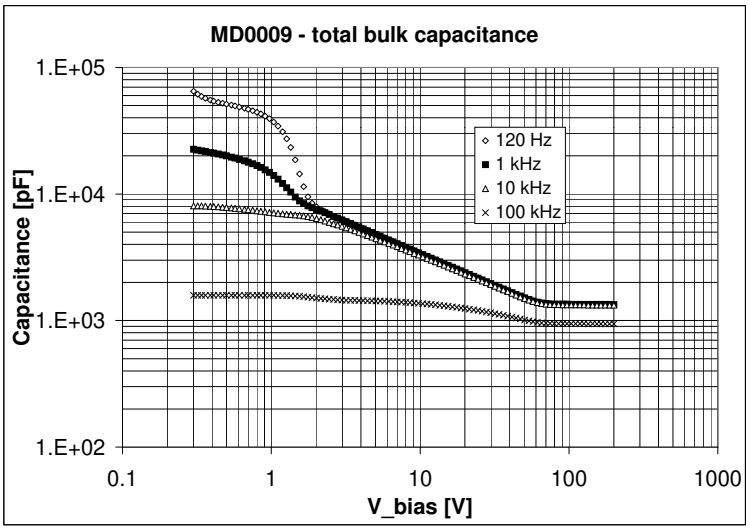

Figure 5.5: C/V curves for different frequencies.

For small bias voltages ($V_{bias} < 3V$) a decrease in C_{bulk} was observed with increasing frequency. For non irradiated detectors no strong frequency dependence of the measured capacitance at bias voltages above 3V up to frequencies of 10kHz was observed. The measurement done at 100kHz shows a lower value of the total bulk capacitance in the overall voltage range.

For the frequency dependence of C_{bulk} different effects contribute:

- *Interface-states.* The contribution of the capacitance of the $Si-SiO_2-$interface-region to the total capacitance for $V_{bias} < V_{zm}$ can explain a frequency dependence in the measured capacitance for small values of V_{bias} [Wun92]. The zone-merging-voltage V_{zm} denotes the value of the bias voltage where the depletion regions around the individual strips merge into one common depletion layer below all strips. At this voltage the total area contributing to the measured capacitance becomes smaller which can be seen as a step-like decrease in the C/V-curve. Interface-states in the $Si - SiO_2-$interface-region contribute to the measured capacitance only for voltages below V_{zm}. They can follow the AC-voltage of the LCR-meter only at small frequencies, leading to a higher value of the measured capacitance compared to high frequencies.

- *Series resistance from biasing resistors.* The displayed capacitance in the parallel mode of the LCR differs from the capacitance of the depleted volume according to appendix A, leading to smaller values at high frequencies.

- *Deep energy levels.* One reason for a lower value of C_{bulk} at high frequencies is the presence of damage induced deep energy levels that, depending on their energetic position, can follow the AC-voltage of the LCR meter only at sufficiently small frequencies. For higher frequencies they do not contribute to the total capacitance and thus lead to a lower value of C_{bulk} [Fei97]. This explains mainly the strong frequency dependence of the total bulk capacitance for neutron-irradiated detectors.

5.2.2 Depletion Voltage

During operation in the ZEUS experiment all detector-modules have to be fully depleted to achieve the maximum resolution and charge collection efficiency. The bias voltage has the following impact on the detector performance:

- *Resolution worsening due to reduced diffusion of charge carriers.* A larger value of the depletion voltage leads to a higher electric field in the detector. The charge collection time decreases and therefore one can benefit less from the resolution increase due to charge diffusion [Bel83]. This argument holds only for perpendicular tracks.

- *Danger of local breakdown.* A larger value of V_{dep} causes a larger field inside the detector. This could lead to a field strength at critical points (e.g. at the

$p^+-Si-SiO_2-$triangle) where a local avalanche breakdown may occur, resulting in an increase of the leakage current.

- *Heating up of the detector-modules.* The power consumption in the detector modules at full depletion increases at least linearly with V_{dep}:

$$P = V_{dep} \cdot I_{leakage} \tag{5.2}$$

The maximum power that can be absorbed in the detectors is limited by the design of the cooling system. An increasing temperature would, according to equation 1.35, lead to an increasing current, resulting in additional noise as well as in further increasing current. A *thermal runaway* might occur where the current and temperature increase until the detector module is destroyed. After moderate doses of hadronic irradiation as expected during the operation-time of the MVD V_{dep} will decrease while on the other hand $I_{leakage}$ will increase.

- *Radiation hardness.* Hadronic irradiation leads to a decrease in the depletion voltage until type inversion (see section 1.5.2). Detectors with higher starting values of V_{dep} (corresponding to larger values of N_{eff}) will reach the type inversion at a higher fluence and can thus be called radiation harder.

The radiation hardness was considered to be the most important design aim with respect to the resistivity of the ordered material. In any case a type inversion during the MVD lifetime should be avoided. Therefore a depletion voltage around $V_{dep} \approx 150V$ was originally specified. However, the producer could only offer detector material with a resistivity of $3k\Omega cm < \rho < 6k\Omega cm$, corresponding to $60V < V_{dep} < 115V$.

The depletion voltage has been estimated from a $1/C^2-V-$plot (fig. 5.6) by fitting with two straight lines, one in the region of an almost linear increase and one in the plateau region. V_{dep} is assumed to be reached at the intersection of these two lines, i.e. when the measured capacitance becomes constant. For all 20 detectors of the first production batch the depletion voltage before irradiation was about

$$V_{dep} = 65V, \tag{5.3}$$

which according to equation 1.29 corresponds to an effective doping concentration of

$$N_{eff} = 7.9 \cdot 10^{11} \frac{1}{cm^3}. \tag{5.4}$$

From this value the Fermi potential

$$\phi_F = -\frac{E_{F_n} - E_{F_i}}{q}$$

in the $n-$bulk can be derived as

$$\phi_F = -\frac{kT}{q} \ln \frac{N_{eff}}{n_i} = -0.11V. \tag{5.5}$$

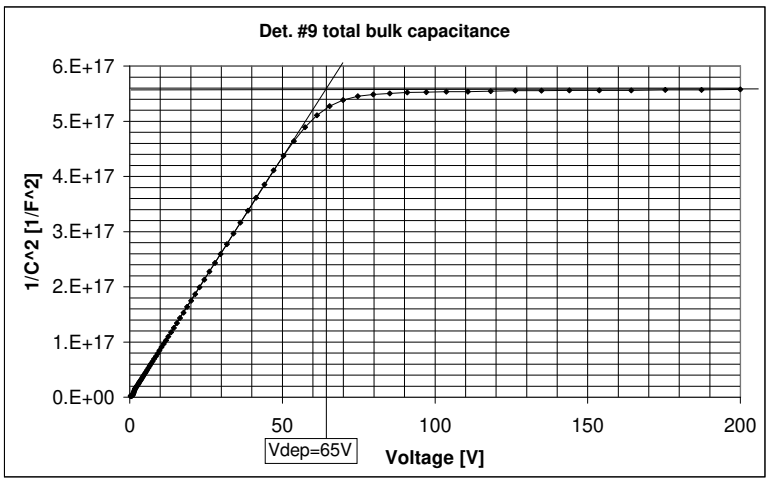

Figure 5.6: Total bulk capacitance in a $\frac{1}{C^2}/V-$plot.

5.2.2.1 V_{dep} after neutron irradiation

For the detector which had received a neutron irradiation with $\phi_{eq} = 1 \cdot 10^{13} cm^{-2}$, the depletion voltage has been not only estimated before, but also at two different annealing times after the irradiation. For this detector a value of $V_{dep,unirrad} = 68V$ has been observed before the irradiation. One week after the irradiation a depletion voltage of $V_{dep,1w} = 17V$ has been measured. Three weeks after irradiation V_{dep} has increased again to $V_{dep,3w} = 30V$ (fig. 5.7).

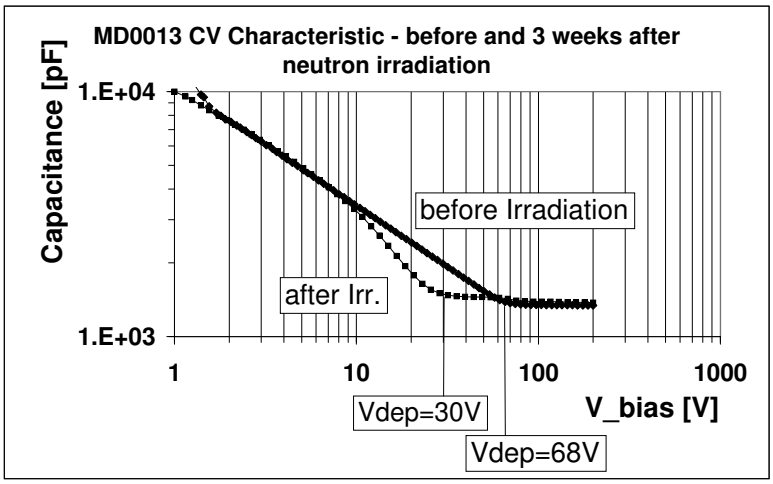

Figure 5.7: Depletion voltage before and three weeks after neutron irradiation with $\phi_{eq} = 1 \cdot 10^{13} cm^{-2}$ (measurement frequency: $f = 1kHz$).

According to section 1.5.2, the neutron irradiation causes displacement damages in the silicon lattice of the bulk volume, resulting in a change of N_{eff}. By annealing and reverse annealing N_{eff} finally becomes a complicated function of the received fluence,

temperature and annealing time after irradiation, described by the empirical formula (1.36).

The measured and expected values of the depletion voltage for the two annealing times are summarized in table 5.1.

annealing time	V_{dep} measured	V_{dep} predicted
$1\,week$	$17V$	$14V$
$3\,weeks$	$30V$	$13V$

Table 5.1: Measured and predicted depletion voltage for 2 different annealing times after neutron irradiation with $\phi_{eq} = 1 \cdot 10^{13} cm^{-2}$.

As one can see from figure 5.7, the estimation of the the depletion voltage becomes difficult for irradiated detectors. Taking this into account, the measurement results are in agreement with the predictions. The influence of hadronic irradiation on the depletion voltage of the detectors can therefore be described by empirical formulae that parametrize the radiation induced bulk damage.

For the experiment a similar maximum dose of about $3kGy$ of hadronic irradiation during the expected operation time of 5 years has been assumed (see section 2.4). Contrary to the neutron irradiation test in Ljubljana the radiation will not occur as one single dose but will be distributed over the whole operation time, leading to a more complicated annealing process. Therefore with this irradiation test only the basic quantitative understanding of the radiation induced change in the depletion voltage has been proven, indicating no additional unexpected radiation effects at the detectors.

A beam test of this detector to determine the efficiency and position resolution after the neutron irradiation is under way.

5.2.3 Effective doping concentration

From the depletion voltage measured before irradiation ($V_{dep} = 65V$) the effective doping concentration N_{eff} can be determined according to equation (1.29) as

$$N_{eff} = \frac{2\epsilon_{Si}(V_{dep} + V_{bi})}{q_0 d^2} = 7.9 \cdot 10^{11} \frac{1}{cm^3}. \tag{5.6}$$

The $\frac{1}{C^2}-$plot (fig. 5.6) offers another possibility to directly calculate N_{eff} from the slope of the curve as

$$N_{eff} = \frac{2}{q_0 \epsilon_{Si} A^2 (\frac{d\frac{1}{C^2}}{dV})}. \tag{5.7}$$

For the unirradiated detectors this yields a value of about

$$N_{eff,slope} = 9.7 \cdot 10^{11} \frac{1}{cm^3}.$$

For the neutron irradiated detector the change of the depletion voltage also corresponds to a change in the effective doping concentration. The observed strong frequency dependence and the changed shape of the C/V curves after the neutron irradiation makes it questionable to obtain N_{eff} from the slope of the C/V curve. Thus only the estimated depletion voltages from table 5.1 has been used to calculate N_{eff} after irradation. The resulting values are

$$N_{eff,1w} = 2.1 \cdot 10^{11} \frac{1}{cm^3}$$

after one week and

$$N_{eff,3w} = 3.7 \cdot 10^{11} \frac{1}{cm^3}$$

after three weeks of annealing.

5.2.4 Resistivity of the n-material

The resistivity ρ of the bulk can be evaluated from the concentration of electrons and holes and their mobility according to equation 1.3. For the calculation it has been assumed that the free electron concentration n_e is much higher than the hole concentration n_h. The resistivity ρ can in this case be estimated as

$$\rho = \frac{1}{q \cdot \mu_e \cdot N_{eff}}. \tag{5.8}$$

For the unirradiated detectors a value of about

$$\rho = 5.3 k\Omega cm$$

is obtained. The specified range was

$$3 k\Omega cm < \rho < 6 k\Omega cm.$$

5.2.5 Biasing resistors

Each strip on the detector is connected to the bias ring via one resistor made of polysilicon (fig. 3.1). The purpose of these resistors is to bias all strips to the same potential without loosing signals to the bias ring.

The biasing resistors are sources for parallel thermal current noise at the preamplifier inputs of the readout channels. A high value for the biasing resistors is thus desirable for a small noise in the readout channels. Large differences in the resistance values between neighbouring strips could (for large dark currents) result in a spread of the strip potentials. This would cause a distortion of the electric field below the strips and part of the signals could be lost to neighbouring strips. Fig. 5.8 shows a sketch of the electric field inside the detector. The overlap o at the right and at the left side of strip 2 denotes the area were field lines starting below strip 2 end in strip 1 or in strip 3. A large value of o corresponds to a systematic shift of the particle position measured

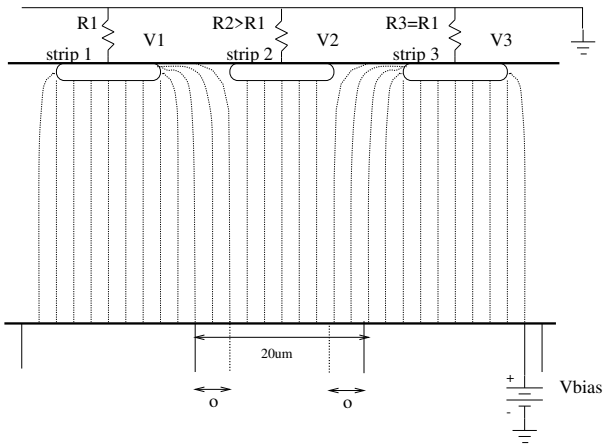

Figure 5.8: Sketch of the electric field inside the detector.

by the detector. The overlap o can be estimated from the dark current and from the differences of the biasing resistors in the following way. The biasing resistor R_2 of strip 2 is considered to have a larger value than the one of the neighbouring strips 1 and 3. Therefore the voltage drop caused by the dark current through R_2 is also larger than for the strip 1 and 3, resulting in a higher potential of strip 2: $V_2 > V_1 = V_3$. According to Gauss' law, the number of field lines ending in a strip is proportional to the charge on this strip: $\oint \vec{E} d\vec{f} = \frac{Q}{\epsilon_{Si}}$. This relation can be used to estimate o. Fig. 5.9 shows a simplified model of 2 neighbouring strips inside the detector. The charge on strip 1

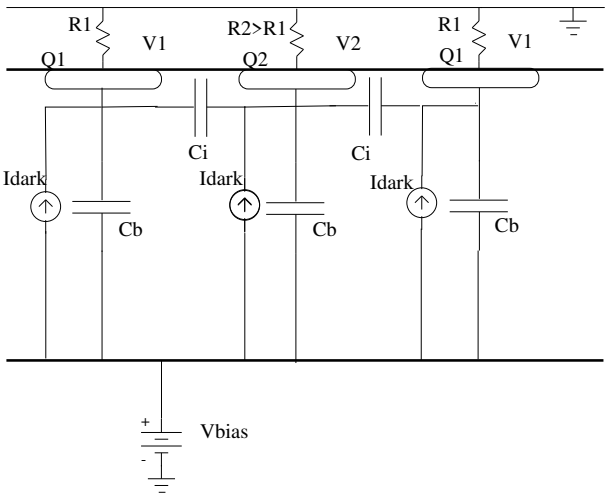

Figure 5.9: Simplified detector model for estimating the influence of the biasing resistors on the distribution of the electric field lines.

and strip 2 is given by the relations

$$Q_1 = C_i(V_1 - V_2) + C_b(V_1 - V_{bias}) \quad (5.9)$$
$$Q_2 = 2 \cdot C_i(V_2 - V_1) + C_b(V_2 - V_{bias}). \quad (5.10)$$

With $C_i = x \cdot C_b$ this yields for the fraction of mislead field-lines:

$$\left|\frac{Q_1 - Q_2}{Q_1 + Q_2}\right| = \left|\frac{3 + x}{x \cdot \frac{R_1 + R_2 - 2 \cdot V_{bias}/I_{dark}}{R_1 - R_2} - 1}\right| \quad (5.11)$$

To demonstrate the importance of well dimensioned biasing resistors two cases are considered:

- *Biasing resistors in the GΩ−range.* An irradiated detector with high leakage current ($I_{dark} = \frac{100\mu A}{3082} \approx 30nA/strip$) is assumed. The interstrip-capacitance is about 10 times larger than the capacitance to backplane ($x = 10$). 2 strips with $R_1 = 1.0G\Omega$ and $R_2 = 1.5G\Omega$ are biased to $V_{bias} = 100V$. Under these assumptions one gets:

  $$|\frac{Q_1 - Q_2}{Q_1 + Q_2}| = 16\%.$$

  With a strip pitch of $20\mu m$ this results in an unacceptably large overlap of

  $$o = 1.5\mu m$$

  .

- *Biasing resistors in the MΩ−range.* In this case values of $R_1 = 10M\Omega$ and $R_2 = 15M\Omega$ are assumed, resulting in an overlap of

  $$o = 2nm,$$

  which is negligibly small.

From these examples it becomes obvious that even a large spread in the values of the poly-silicon resistors will hardly affect the field distribution inside the detector, as long as the values of the resistors remain in the $M\Omega$−range.

The specified range for the poly-silicon resistors is $R_{poly-si} = 1.5 \pm 0.5M\Omega$. A larger spread would not be critical for the detector performance but it would indicate possible problems in the production technology of the manufacturer.

On the detector the poly-silicon resistors are accessible from outside only through the coupling capacitors and can thus not be measured with a DC I/V measurement. For this purpose 10 poly-silicon resistors are located on each test-structure which have probing-contacts on both sides (fig. 3.3).

Measurements of the poly-silicon resistors have been performed for a sample of the available test-structures. The measured values were between $R_{poly-si} = 1.5M\Omega$ and

$R_{poly-si} = 2.5M\Omega$. The spread of the poly-silicon resistance values within one batch was always below $\pm 0.1M\Omega$.

On the neutron irradiated test-structure ($\phi_{eq} = 1 \cdot 10^{13} cm^{-2}$) an increased value of $R_{poly-si} = 2.8M\Omega$ has been measured after the irradiation. This increase can qualitatively be understood as the reduction of free charge carriers due to radiation induced defects.

5.2.6 p^+ strip resistance

The finite resistance of the p^+-implants reduces the charge-spread time constant of the strips. Thus the charge created and collected at a p^+-strip will disperse little during the integration time of the readout electronics.

The number of acceptors in the p^+-implant has to be larger than the number of donors in the depletion region of the detector, which are created by the backplane bias potential. Only then all field lines end in p^+-strips. This will be achieved for standard implantation depths if the p^+-resistance is on the order of the specification value of $R_{p^+} < 150k\Omega/cm$.

The implant width of the readout-p^+-strips is $14\mu m$ (W14), the width of the intermediate strips is $12\mu m$ (W12). Both types of strips are also part of the test-structures. The resistance of a single p^+-implant can not be measured directly on the detectors. Therefore all measurements have been performed on single strips on the test-structures.

The p^+-resistance has been measured on a sample of the test-structures by an I/V-measurement, applying a DC-voltage between both sides of the p^+-strip and measuring the current through the strip. For the W14-strips values of about

$$R_{p^+,W14} \approx 90k\Omega/cm$$

have been measured for unirradiated detectors. For the W12-strips the values were about

$$R_{p^+,W12} \approx 100k\Omega/cm.$$

After neutron irradiation the resistance remained at

$$R_{p^+,W14,n-irrad} \approx 90k\Omega/cm$$

and

$$R_{p^+,W12,n-irrad} \approx 100k\Omega/cm.$$

All measurement values were within the specifications.

5.2.7 Doping concentration N_a of p^+-implantations

The doping concentration N_a of the p^+-implantations can be derived from the p^+-resistivity $\rho_{p^+} = A_{profile} \cdot R_{p^+}$ according to:

$$N_a = \frac{1}{q \cdot \mu_h \cdot \rho_{p^+}}. \tag{5.12}$$

The hole mobility μ_h for high doping concentration is about [Gro67]

$$\mu_h = 90cm^2/(V \cdot s).$$

The implantation depth of the p^+-implants is about $d_i = 0.1\mu m$ ($30keV$ bor implantation technology), resulting in an area of

$$A_{profile} = 1.2 \cdot 10^{-8} cm^2$$

for the W12 profile. With a p^+-resistance of $R_{p^+,W12} = 100k\Omega/cm$ a value of about

$$N_a = 5.8 \cdot 10^{19} cm^{-3} \tag{5.13}$$

is obtained.

5.2.8 Built-in-voltage V_{bi}

The built-in-voltage of the p-n-junctions is given by the difference of the fermi-levels on the p^+- and on the $n-$side (equation 1.23). From the effective doping concentration N_{eff} of the $n-$bulk (5.4) and from the doping concentration N_a of the p^+-implantations (5.13) one can estimate the built-in-voltage according to equation 1.23 as

$$V_{bi} = 0.7V. \tag{5.14}$$

With equation 1.22 this yields for the depletion depth at $V_{bias} = 0V$:

$$W\left(V_{bi}\right) = 34\mu m. \tag{5.15}$$

5.2.9 Aluminum strip resistance

The aluminum readout strips on top of every sixth p^+-strip form a coupling capacitance C_c with the underlying p^+-strip which transfers the collected AC-signal to the readout electronics. Due to the large value of the resistivity of the p^+-strips ($R_{p+} \approx 200k\Omega/cm$, see section 5.2.6), the collected charge will not spread all along the p^+-strip but will remain close to the position where the charge is collected at the p^+-strip. A large resistance R_{Alu} along the aluminum strips would form a low-pass-filter with C_c for particles crossing the detector far away from the bonds to the readout electronics. This would lead to a loss of signal height depending on the position of the particle along the strips. For the MVD detectors a value of $R_{alu} < 20\Omega/cm$ has been specified.

The aluminum strip resistance has been measured for a sample of the prototype detectors. For this purpose I/V measurements similar to the p^+-strip resistance measurements (section 5.2.6) have been performed directly on the detectors and also on the test-structures. Due to the small resistivity of the aluminum, the simple 2 wire measurement is very sensitive to errors caused by cable- and connection-resistors. Therefore the value for R_{Alu} has only been estimated to be within the specification:

$$R_{Alu} < 20\Omega/cm.$$

For a more precise determination of R_{Alu} one would have to use the 4 point measurement principle which excludes errors due to cable and connection resistors.

5.2.10 Coupling capacitance

When reading out the detector signals into the preamplifier and shaper frontend electronics, one has to make sure not to saturate the charge amplifiers with the DC leakage current from the detector. In order to avoid this problem an AC readout through coupling capacitors has been chosen. The readout capacitance, which is formed by the series circuit of each coupling capacitor C_c and the effective input capacitance C_{ampli} of its corresponding preamplifier channel, has to be large compared to the interstrip and backplane capacitances inside the detector. Otherwise a signal loss to the backplane and to the neighbouring channels would occur which results in a deterioration of the resolution and charge collection efficiency.

The coupling capacitor for each readout channel is formed by the aluminum readout strip, its p^+-strip below and a double layer of SiO_2 and Si_3N_4 in between. The value of C_c is geometrically determined by the area of the p^+- and readout-strips as well as the thickness of the double layer.

The value of the coupling capacitors has been specified to $C_c > 20pF/cm$, which is sufficiently large compared to the backplane capacitance ($C_{bulk,singlestrip} = 0.07pF/cm$, see section 5.2.1) and the interstrip capacitances ($C_i \approx 1.5pF/cm$).

Measurements of C_c have been performed directly on the detectors and on single strips of the test-structures. The detector measurements have been accomplished with the LCR meter measuring between one readout strip and the bias line while the detector was biased to full depletion. The LCR setting was "series-mode", assuming that the measured device consists of the bias resistor $R_{poly-si}$ and the coupling capacitance C_c in series. The influence of neighbouring channels has been neglected, assuming that the coupling capacitance is much larger than the capacitances inside the detector. Due to the p^+-strip resistivity, only for small frequencies the whole strip is seen by the signal, higher frequencies lead to a lower value of the measured capacitance. Therefore only the values at $f = 120Hz$ have been taken. All measurement results were within the specification. Typical values of

$$C_c = 27pF/cm$$

have been observed. The displayed values for the poly-silicon resistors were on the order of $R_{poly-si} = 2M\Omega$, consistent with the measurements performed at the poly-silicon resistors on the test-structures (see section 5.2.5). To cross check the results of the detector measurements, also the single strips on the test-structures have been investigated. In this case also the p^+-strip has a contact pad, allowing to measure with the LCR meter directly between aluminum- and p^+-strip (fig. 3.3). The results obtained on the test-structures agreed with the corresponding detector measurements.

5.2.11 Quality of coupling capacitance dielectric

Pinholes in the oxide can introduce a DC-connection between the implant and the aluminum readout strip. In this case the detector leakage current will flow directly into the charge amplifier and may saturate it. The additional Si_3N_4-layer below the aluminum strips can prevent the readout electronics from such shorts in case of pinholes in the SiO_2. The double layer technology has been chosen to combine the advantages of both isolation materials: The large resistivity of the SiO_2 and the negligible number of expected pinholes in the Si_3N_4.

The quality of the coupling layers has been specified with the maximal leakage current I_{cc} through the coupling capacitor C_c. At a certain voltage V_{cc}, applied between implant and readout strip, the leakage current through the coupling layers can be measured. It has been specified to $I_{cc} < 100pA$ at $V_{cc} = 60V$. During normal detector operation, implant and readout strip are at similar potential ($V_{cc} \leq 1V$). However, due to a high flux of particles through the detector caused by a beam loss, a larger potential difference may occur. Even in this case a sudden increase in I_{cc} by a breakdown through the double layer has to be avoided. It would possibly destroy the coupling capacitor permanently, resulting in a bad channel.

Measurements of I_{cc} and the breakdown voltage V_{bd} have been performed directly on the detector, applying a voltage between the bias line and single strips. An example of the resulting I/V-curves is shown in figure 5.10. For all measured prototype detectors

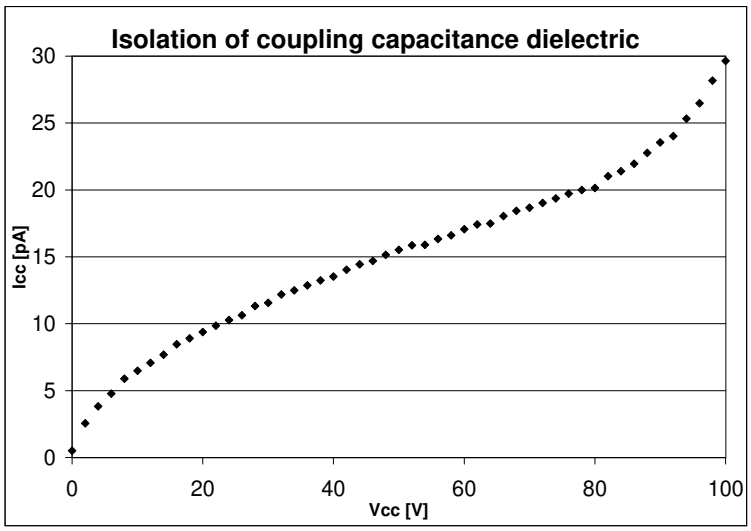

Figure 5.10: I/V measurements for the coupling capacitors.

the specifications were fulfilled with $I_{cc} < 20pA$ at $V_{cc} = 60V$.

It has been observed that the coupling layers are sensitive to voltage transients. Measurements have been performed with the applied voltage set to $0V$ after each measurement point and immediately afterwards raised to the next measurement voltage with a gradient of about $10\,V/1\,ms$. In this case the coupling capacitor is permanently

damaged already at an applied voltage transient of $V_{cc} < 10V$, which can be seen from a high leakage current ($I_{cc} > 100pA$ at $V_{cc} = 60V$). The current remains in this order, even when the voltage is raised smoothly again. Since an eventual beam loss in the experiment would occur within about $100ns$, the observed sensitivity to voltage transients can lead to a damage of the coupling capacitors in the those detectors which are affected by a beam loss. The problem is still under study.

5.2.12 Total leakage current

The leakage current through the p^+-strips affects the detector performance mainly as a source of noise for the preamplifier input. For a CR-RC pulse-form shaper, as it is used in the HELIX readout chip, the noise level in terms of ENC increases with the square-root of the leakage current:

$$ENC_I = \frac{e}{2}\sqrt{\frac{I_S}{q}T_p}. \tag{5.16}$$

I_S is the total leakage current of a single strip and T_p is the peaking time of the signal shaper. ($T_p \approx 60ns$ for the HELIX readout chip [FR97].) Due to the large number of 512 readout strips[2], the noise from the leakage current is small even for a large total leakage current. A total leakage current of $I = 200\mu A$ e.g. yields a noise of

$$ENC_I = 200e,$$

which is has to be compared with the signal of about $25000e$ for $1MIP$.

The total leakage current has to be limited and stable within long-term operation in the ZEUS environment, in order to ensure a proper functioning of the detector system with respect to the cooling system and the design of the power supplies. High and unstable leakage currents can also indicate problems in the manufacturing technology.

The total leakage current at $T = 20^oC$ has been specified not to exceed $I_{max} = 2\mu A$ at a bias voltage of $V_{bias} = 200V$.

Bulk generation- and recombination-current, diffusion current and surface generation current as sources of the detector leakage current are explained in section 1.4. On the detectors only the sum of these currents can be measured while on the gated diode, located on the test-structures, it is possible to separate the individual contributions to the total leakage current [Joh94].

The setup for the global I/V-measurements was the same as the one for the global C/V measurements (figure 5.3). The backplane was biased, the first guard ring grounded and the current through the bias ring was measured.

All measurements have been performed at room temperature ($18^oC < T < 24^oC$) and are corrected to $T = 20^oC$ with formula (1.35) (see section 1.4).

Figure 5.11 shows an example of the resulting I/V-curves for unirradiated detectors. Most of the detectors had a low leakage current on the order of $I_{dark} < 100nA$ at

[2]Because of the capacitive charge division only the readout strips are taken into account for this estimation

$V_{bias} = 200V$. The results are very close to the final quality control measurements done at Hamamatsu. The shape of the I/V-curve does not show a $\sqrt{V}-$dependence of the current as expected for a bulk generation current described by equation 1.33. The current increases up to 80% of the maximum value already within the first $3V$ and remains almost constant to higher bias voltages. This behaviour can be understood by taking into account generation current at the $Si - SiO_2-$interface. The generation centers in the interface area contribute to the total leakage current as soon as they become part of the depleted volume, i.e. when the depletion zones of the individual strips merge into a common depletion layer below the SiO_2. This surface generation current delivers an almost constant contribution to the total leakage current (see section 1.4).

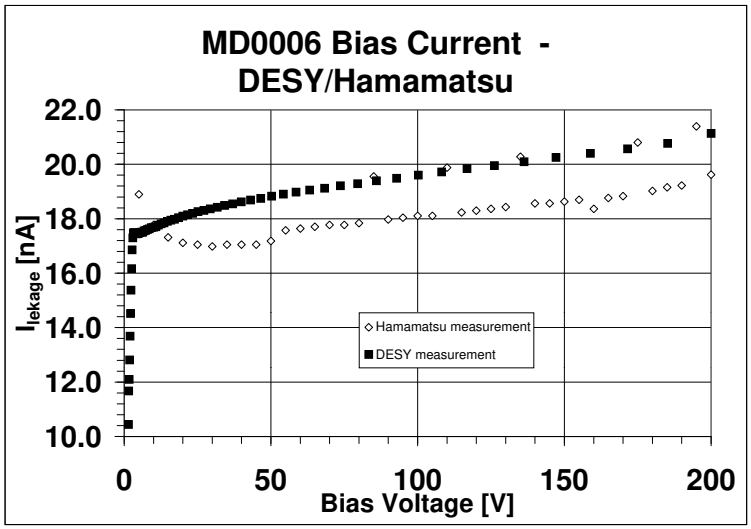

Figure 5.11: Global I/V measurement for one of the protoype detectors.

5.2.12.1 Influence of detector handling on total leakage current

For 6 of the 20 prototype detectors from the first production batch, an increase in leakage current of about 3 orders of magnitude was observed after different handling steps. In order to understand this behaviour, investigations of changing storage and handling conditions have been peformed. Finally the increase in the leakage current was attributed to mechanical damage caused by prober needles.

Figure 5.12 shows an example of a detector becoming "bad". The leakage current measured at $V_{bias} = 200V$ increased from $I_{leakage} = 21nA$ before to $I_{leakage} = 2\mu A$. Also the shape of the I/V-curve changed from the normally observed flat form to a linear increase corresponding to an ohmic resistor of about $R = 70M\Omega$.

An explanation of the increasing current has been found in damage to the detector during measuring with prober needles. The force of the prober needles to the detector is controlled by a spring mechanic. Systematic studies of the total leakage current as

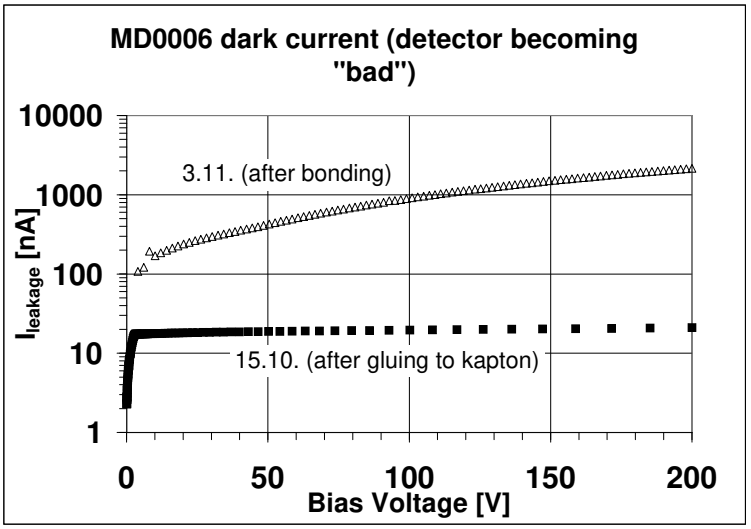

Figure 5.12: Global I/V measurements for a detector becoming "bad".

function of the applied force have been performed [Mar99]. If the force of the needle exceeds $20g$, an irreversible increase of the total leakage current occurs, resulting in I/V-curves similar to the ones of the "bad" detectors measured before. After this result the spring mechanics of the needle-holders have all been calibrated, so that they do not exceed a maximum force of $5g$, which is still sufficient for a good electrical contact to the surface of the detectors and test-structures.

5.2.12.2 Total leakage current after hadronic irradiation

Hadronic irradiation causes bulk damage and leads to a fluence-proportional increase of the bulk generation current as described by formula (1.37) (see section 1.5.2.2).

For the neutron irradiation with $\phi_{eq} = 1 \cdot 10^{13} cm^{-2}$ this model predicts an increase of the leakage current by

$$\Delta I_{1week} = \alpha(1\,week, 21^oC) \cdot \phi_{eq} \cdot V_{det} = 550\mu A$$

for an annealing time of one week at room temperature. After three weeks of annealing, the predicted value is

$$\Delta I_{3\,weeks} = \alpha(1week, 21^oC) \cdot \phi_{eq} \cdot V_{det} = 450\mu A.$$

Figure 5.13 shows the I/V measurement 3 weeks after neutron irradiation. The measured and predicted values are summarized in table 5.2.

The results agree qualitatively with the predicted values. Together with the results from the total bulk capacitance measurements (see section 5.2.2.1) this supports the assumption that the influence of hadronic irradiation on the detector is understood by only taking into account bulk damage. The effect on the detector performance should therefore be limited to an increase of the leakage current that corresponds to an increase of the noise level according to equation (5.16).

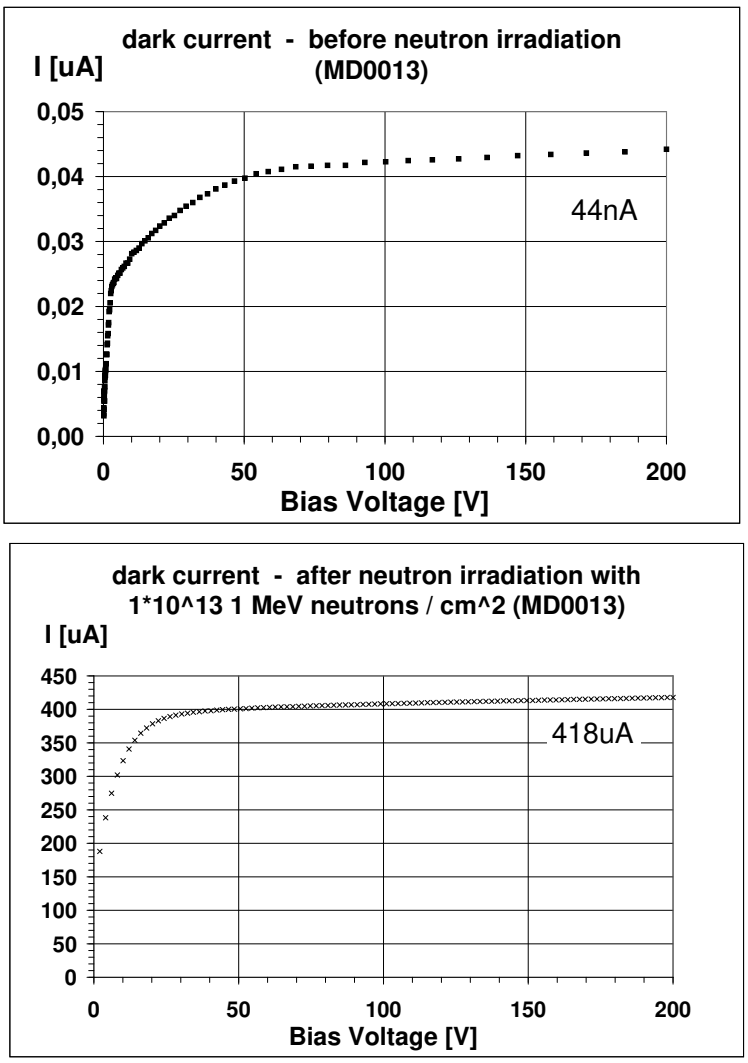

Figure 5.13: Total leakage current before and three weeks after neutron irradiation with $\phi_{eq} = 1 \cdot 10^{13} cm^{-2}$.

annealing time	$I_{leakage}$ measured	$I_{leakage}$ predicted
$1\,week$	$620\mu A$	$550\mu A$
$3\,weeks$	$420\mu A$	$450\mu A$

Table 5.2: Measured and predicted total leakage currents at different annealing times after neutron irradiation with $\phi_{eq} = 1 \cdot 10^{13} cm^{-2}$.

5.2.12.3 Total leakage current after $\gamma-$irradiation

As described in section 1.5.1, low energetic $\gamma-$irradiation mainly causes damage in the SiO_2 and at the $Si-SiO_2-$interface of semiconductor devices. The damage is larger if the SiO_2 is in an electric field which reduces the recombination of created electron-hole-pairs. During normal operation of the detector the p^+-strips and the aluminum readout strips of the MVD detector modules will both be kept at zero potential. The field distribution inside the $SiO_2-Si_3N_4-$isolation layer depends on the geometry of the n-p^+-SiO_2-Si_3N_4-aluminum configuration, on the presence of surface- and oxide-charges and on the biasing conditions. For the irradiation tests only two cases were investigated:

- *Floating irradiation.* All connections on the detector and on the test-structure were left floating.

- *Biased irradiation.* The bias line of the detector was kept at zero potential while the backplane was biased to $V_{bias} = 100V$. Unlike the situation in the experiment, the aluminum readout strips were left floating. For the test-structures, the biased irradiation was performed with the backplane biased to $V_{bias} = 100V$ and with all connections on top grounded. With this connection scheme the SiO_2 layer above the grounded p^+-implanted regions was electrically shielded while the SiO_2-layer in the MOS-regions were inside an electric field with field lines pointing towards the gate. As described in section 1.5.1, the created holes in this field are repelled from the SiO_2-Si-interface and dissipated through the grounded gate. Thus the expected radiation damage is smaller for the biased test structure irradiation than for the unbiased irradiation. It should be noted that for the data reported in literature normally "biased irradiation" is done with a positive biased gate, which increases the expected radiation damage.

  In the measurements no remarkable difference between the biased and the unbiased irradiated test-structures has been observed. Therefore in the following sections it will not be distinguished between biased and unbiased irradiated test-structures.

The radiation induced increase of the detector leakage current depends strongly on the production technology and the specific geometry of the device [Wun92]. No prediction has been made for the additional leakage current after $\gamma-$irradiation. The measured additional leakage current has been scaled to the SiO_2-Si-interface area. These values have been compared to measurements on the test-structures and to published data.

A large increase of the measured leakage current may not affect the detector performance itself but can indicate problems at the $Si-SiO_2-$interface which is the most sensitive area of the detector with respect to charge collection and charge sharing. Possible effects of a radiation induced increase of oxide charges on the detector performance are [AL90]:

- An increase of the interstrip capacitance due to the presence of an electron accumulation layer between two strips.

- A local reduction of the energy sensitivity of the detector, caused by non depleted volumes close to the electron accumulation layer between the strips.

- An increased electric field at the $p^+ - Si - SiO_2-$triangle possibly causing local avalanche breakdown.

These effects may also depend on time, temperature, bias conditions, humidity and external electric fields.

Figure 5.14 shows the total leakage current of a detector as measured before and 18 days after floating $\gamma-$irradiation with $2kGy$. The current at $V_{bias} = 200V$ has increased from

$$I_{leakage,unirrad.} = 22nA$$

before irradiation to

$$I_{leakage,2kGy,fl.} = 13\mu A$$

after irradiation.

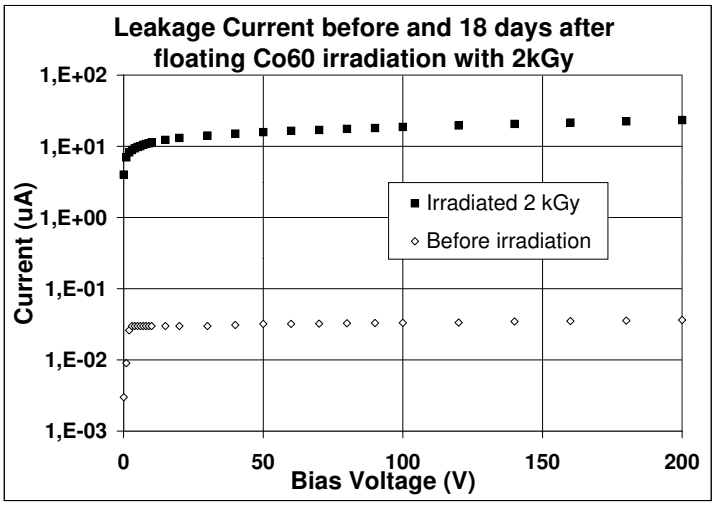

Figure 5.14: Total leakage current before and 18 days after unbiased $\gamma-$irradiation with $2kGy$.

The irradiation under $V_{bias} = 100V$ corresponds more to the situation in the experiment, where the detectors will also be under bias when receiving irradiation. But in contrary to the irradiation test, the aluminum readout strips will be grounded, resulting in a different field distribution. For the irradiation up to $2.9kGy$ at $V_{bias} = 100V$, the leakage current at $V_{bias} = 100V$ has been measured between the single irradiation

steps as plotted in figure 5.15. It can be seen that the leakage current increases linearly with the applied dose up to

$$I_{leakage,2.9kGy,biased} = 370\mu A$$

at the maximum dose of $2.9kGy$.

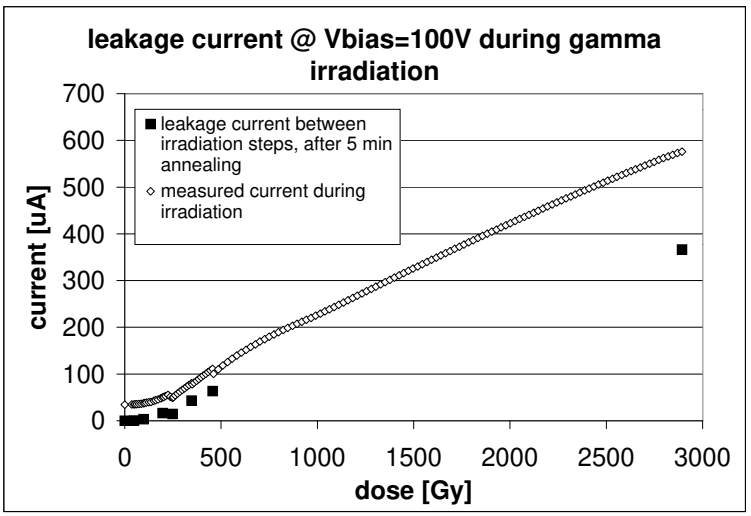

Figure 5.15: Total leakage current between irradiation steps for $\gamma-$irradiation at $V_{bias} = 100V$.

The annealing at room temperature has been studied with measurements until 25 days after irradiation (figure 5.16). After this time a decrease by a factor of 3 from

$$I_{leakage,0} = 425\mu A$$

down to

$$I_{leakage,25days} = 140\mu A$$

at $V_{bias} = 200V$ has been observed. When scaled down lineary to $2kGy$, this value can be compared with

$$I_{leakage,2kGy,fl.} = 13\mu A$$

after the floating irradiation at an annealing time of 18 days.

5.2.12.4 Guard ring current

The three guard rings surrounding the active area of the detector are designed to smoothly adjust the potential from $0V$ at the bias ring to $+V_{bias}$ at the edge [Bec97]. In addition they carry the current generated from defects and impurities outside of the sensitive volume of the detector. For this purpose the two outmost guard rings are left floating and the innermost guard ring is connected to ground during normal detector

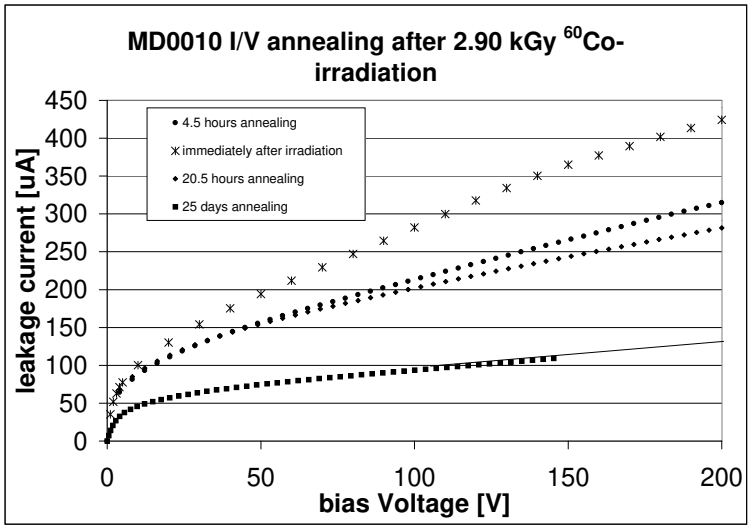

Figure 5.16: Total leakage current at different annealing times after $\gamma-$irradiation with $2.9kGy$ at $V_{bias} = 100V$.

operation. In this configuration the first guard ring can protect the active area of the detector even in the case of very high generation currents from the edge that exceed the total leakage current of the active area by orders of magnitude.

The guard ring structure becomes especially important if type inversion occurs after strong hadronic irradiation ($\phi_{eq} > 1 \cdot 10^{13} cm^{-2}$). In this case, the depletion layer starts growing from the backside, leading to a larger lateral extension of the depletion zone [Lin99]. However, for the life-time of the MVD such high doses are not expected and the detectors will most probably stay n-type.

For the prototype detectors, the guard current has been determined by grounding the bias ring, biasing the backplane and connecting the first guard ring to the LO input of the amperemeter.

The measured guard ring I/V-curve is shown in figure 5.17 for one detector. It was typically about 6% and always below 10% of the corresponding total leakage current. This fraction also remained relatively constant for mechanically damaged detectors and for detectors which had received $\gamma-$irradiation or neutron-irradiation.

5.2.13 Long-term monitoring of the leakage current

Experience with silicon detectors in the past has shown that in some cases for a certain fraction of the delivered detector modules a strong increase in the total leakage current within the first 24 hours of operation under bias is observed [Bar98]. Since these detectors can not be replaced after installation in the experiment, it is important to sort out the respecting detector-modules before mounting. For this purpose a long-term measurement of the leakage current at constant bias voltage for 48 hours is planned for all delivered detectors.

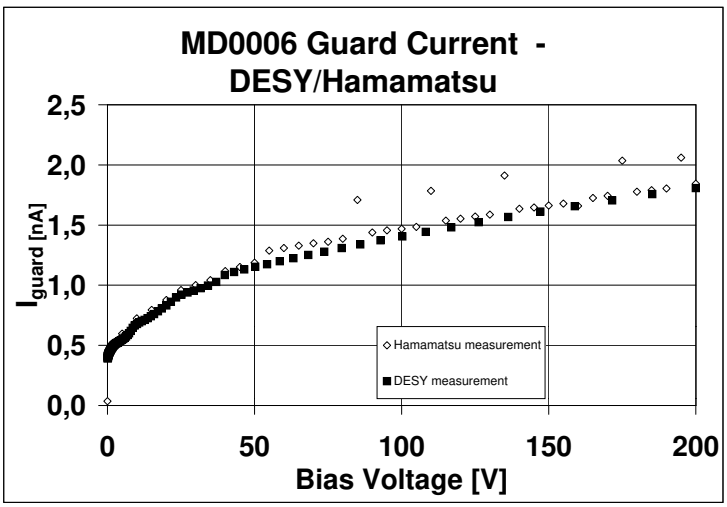

Figure 5.17: Guard ring I/V measurement for one of the protoype detectors.

Eight of the prototype detectors were measured for six weeks at $V_{bias} = 100V$ (figure 5.18). In contrary to the long-term test foreseen for the production phase, they had to be bonded for this test in special support structures (see section 5.1.3). Detector #41 was most probably damaged during bonding. It showed an increase of up to a value of $I_{leakage} = 36\mu A$ immediately after the first measurement. After two weeks it had recovered to a leakage current close to the values measured by Hamamatsu before delivery. The other seven detectors were stable from the beginning and the measurement values are also similar to the measurements done by Hamamatsu.

From these results no problems concerning the long-term stability of the MVD detector modules are expected. The long-term test during the production phase will be limited to 48 hours per detector which is assumed to be sufficient to find detectors with increasing leakage current. For this purpose another prober-test-box has been produced where the leakage current of 10 unbonded detectors can be measured at the same time.

5.2.14 MOS capacitor measurements

Capacitance-voltage-characteristic measurements on the MOS capacitor located at the test-structures were used to extract technological parameters related to the detector surface region.

Figure 5.20 shows a CV-measurement for an unirradiated test-structure. The bias voltage is applied between the aluminum gate on top and the backplane. The measured capacitance allows to distinguish three regions [Gro67]:

- *Accumulation region.* The positive charges in the oxide (oxide charges) and at the $Si - SiO_2-$interface (interface charges) are compensated by electrons which

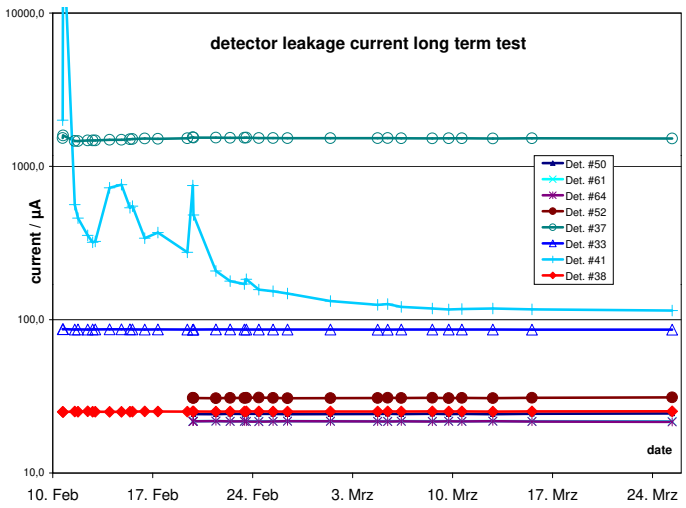

Figure 5.18: Long-term test of total leakage current at $V_{bias} = 100V$.

are accumulating in the silicon close to the interface. The same holds for positive charges on a positively biased gate. The *accumulation layer* acts like a metal plate for the CV-measurement. The n-doped bulk is not depleted and thus the measured capacitance corresponds to the geometric capacitance of the oxide. The oxide thickness can be derived from the capacitance measured in accumulation as

$$t_{ox} = \frac{\epsilon_{SiO_2} \cdot A}{C_{ox}}. \tag{5.17}$$

- *Depletion region.* A negatively biased gate repells free electrons in the silicon from the $Si - SiO_2-$interface and a positive charged zone depleted of free carriers is created below the oxide. It acts as an insulator, increasing the distance between the gate and the neutral bulk. Therefore the measured capacitance decreases. The applied voltage has to first compensate for the work function difference between aluminum and silicon by about $\phi_{ms} = -1.0V$ and for the potential created by positive oxide- and interface-charges. Thus the flatband voltage, defined as the voltage at which charges in the oxide and the work function difference potential are exactly compensated, is shifted to negative voltages. The density of oxide- and interface-charges can be derived from the flatband-voltage V_{fb} as

$$Q_{ox} = -\left(V_{fb} - \phi_{ms}\right) \cdot \frac{C_{ox}}{A} \tag{5.18}$$

- *Inversion region.* A more negative gate voltage results in a build-up of holes below the SiO_2 forming an *inversion layer*. The measured capacitance then corresponds

to the series of the oxide capacitance and the depletion layer capacitance:

$$C_{inv} = \frac{C_{ox} \cdot C_{dep}}{C_{ox} + C_{dep}} \tag{5.19}$$

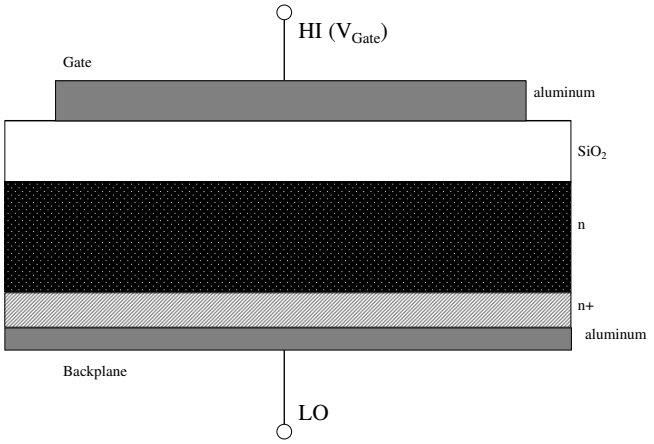

Figure 5.19: scheme of setup used for MOS-capacitance measurements.

5.2.14.1 Oxide-thickness t_{ox}

From the accumulation region in figure 5.20 the oxide capacitance can be determined as $C_{ox} = 29pF$. The same value has been measured for all test-structures from the first prototypes. With $\epsilon_{SiO_2} = 3.45 \cdot 10^{-13} Fcm^{-1}$ and an estimated area of the MOS capacitor of about $A = 5 \cdot 10^{-3} cm^2$ the oxide thickness t_{ox} has been calculated with equation (5.17) to:

$$t_{ox} \approx 600nm.$$

This value is valid also for the thickness of the field oxide between the p^+ strips in the detector since detector and test-structure are made in the same production process.

5.2.14.2 Density of oxide- and interface-charges for unirradiated detectors

The density of positive charges in the SiO_2-bulk and at the $SiO_2 - Si-$interface depends on the crystal orientation and on details of the production process which is the same for the test-structures as for the detectors. Thus the density of oxide- and interface-charges as derived from the MOS capacitor will also be the same for the oxide in the detector.

The positive oxide- and interface-charges lead to an electron-accumulation layer below the oxide. These electrons may affect the detector performance as they distort

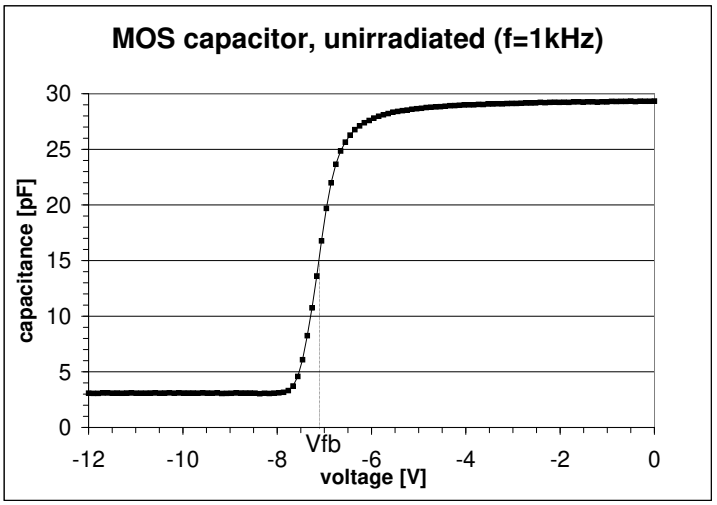

Figure 5.20: C/V measurement of unirradiated MOS capacitor.

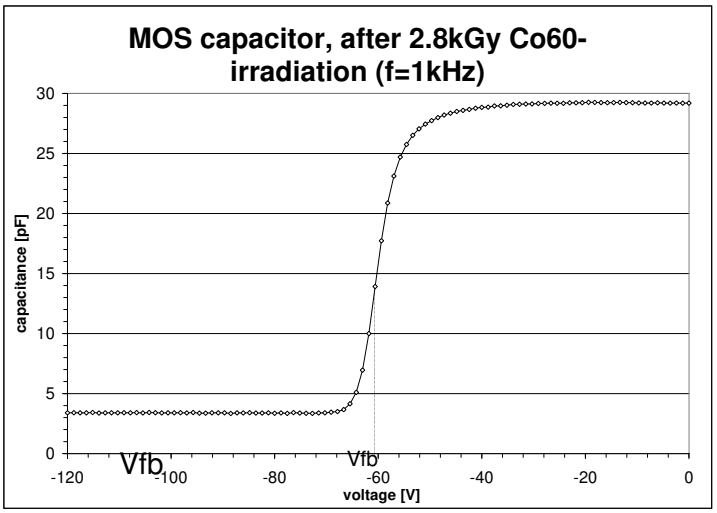

Figure 5.21: MOS capacitor C/V measurement after $\gamma-$irradiation with $2.8kGy$.

the electric field between the p^+-implants. In contrary to the MOS capacitor on the test-structures, there is no gate above most of the SiO_2 in the detector, which could guarantee a strong inversion below the oxide. Thus the electron layer may lead to a high field at the $p^+-n-SiO_2-$triangle even at full depletion, causing a local avalanche breakdown that increases the leakage current. Besides an increase in the leakage current, a high density of oxide- and interface-charges can also affect the charge collection and the charge division between neighbouring strips. Both depend on the DC-isolation and a constant capacitance between neighbouring strips. These parameters may be changed by charges in the oxide- and interface-region.

Several ways of determining the flatband-voltage from the CV-curve of the MOS capacitor have been proposed [Joh94]. In this work the flatband-voltage is estimated as the voltage where the maximum slope of the C/V-curve is observed.

The flatband-voltage for the unirradiated test structure in figure 5.20 has been estimated from the CV-curve as

$$V_{fb} = -7V.$$

The density of oxide- and interface-charges can be derived from the measured capacitance in accumulation ($C_{ox} = 29pF$), the estimated area of the MOS capacitor ($A = 5 \cdot 10^{-3} cm^2$), the measured flatband voltage ($V_{fb} = -7V$) and with $\phi_{ms} = -1.0V$ according to equation (5.18):

$$\begin{aligned} Q_{ox} &= 3.5 \cdot 10^{-8} Cb/cm^2 \\ \text{corresponding to } N_{ox} &= 2.2 \cdot 10^{11}\, states/cm^2. \end{aligned}$$

Similar values have been obtained for all unirradiated detectors.

5.2.14.3 Density of oxide- and interface-charges after $\gamma-$irradiation

As described in section 1.5.1, low energetic $\gamma-$irradiation leads to an increase of oxide- and interface-charges.

The additional amount of positive charges ΔQ_{ox} can be derived from the shift in the flatband-voltage measured after irradiation.

A measurement for a MOS capacitor after $50Gy$ $\gamma-$irradiation showed a flatband voltage of

$$V_{fb} = -15V,$$

corresponding to an additional charge density of

$$\Delta N_{ox} = 2.5 \cdot 10^{11}\, states/cm^2.$$

Figure 5.21 shows the CV-characteristic of the MOS capacitor after receiving a $\gamma-$irradiation with $2.8kGy$. A shift of the flatband voltage to

$$V_{fb,2.8kGy} = -60V$$

can be observed at a measurement frequency of $f = 1kHz$. This value corresponds to an additional density of positive charged states of

$$\Delta N_{ox} = 1.8 \cdot 10^{12}\, states/cm^2.$$

Compared to the C/V measurement before irradiation (figure 5.20), the curve shows a more shallow transition from accumulation to inversion. This shape indicates interface states which change their charge with the fermi level at the interface.

Another effect that has been observed after $\gamma-$irradiation is shown in figure 5.22. Not only the shape of the C/V curve but also the value of the flatband voltage becomes frequency dependent and reaches values from $-50V$ measured at $10kHz$ to $-68V$ measured at $120Hz$. The strong discrepancy of the $100kHz$ measurement can be attributed to the parallel mode of the LCR meter which leads to a smaller displayed capacitance for high frequencies. The shift of the flatband voltage for frequencies from $10kHz$ to $120Hz$ has not been understood. The value for the radiation induced additional charge density, which is given above, can thus only be a rough estimation.

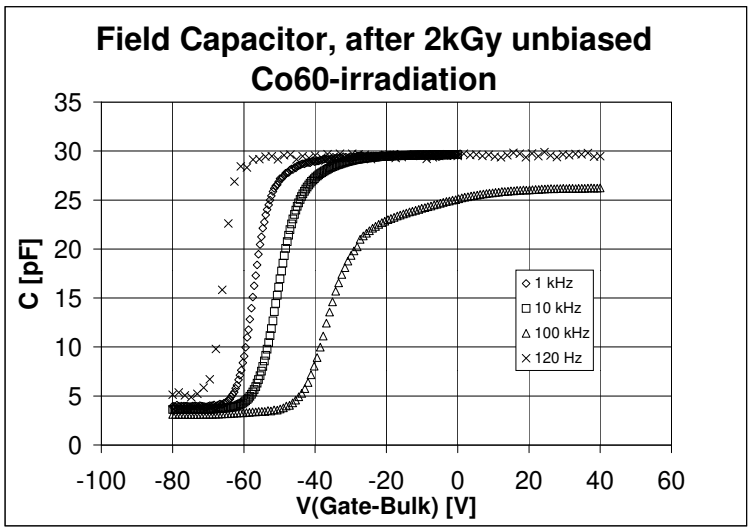

Figure 5.22: CV-measurement of a MOS capacitor about 5 hours after floating $\gamma-$irradiation with $2kGy$.

5.2.14.4 Annealing after $\gamma-$irradiation

Figure 5.23 shows the C/V measurement of a MOS capacitor 17 days after $\gamma-$irradiation with $2kGy$. Compared to the measurement which was performed immediately after irradiation (figure 5.22), the flatband voltage is shifted again to lower values by about $10V$ for all frequencies.

Annealing has been observed for all measured parameters that changed with $\gamma-$irradiation.

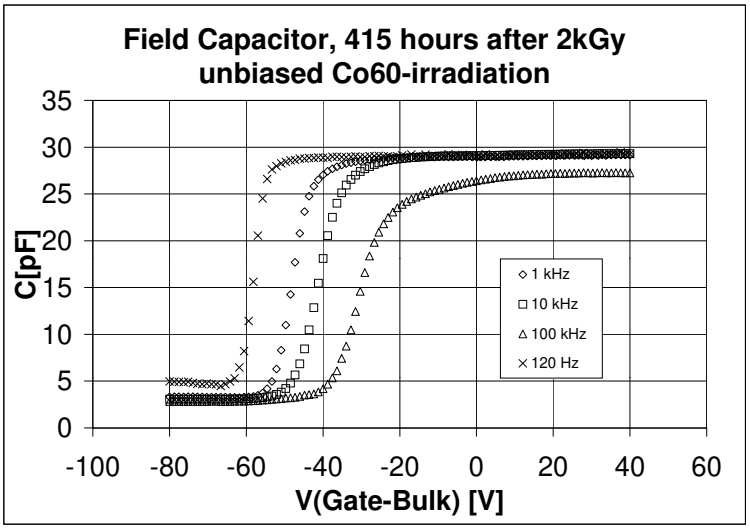

Figure 5.23: CV-measurement of a MOS capacitor 415 hours after floating $\gamma-$irradiation with $2kGy$.

5.2.14.5 Depletion depth below the gate

From the oxide capcitance C_{ox} (section 5.2.14.1) and the minimum capacitance measured in inversion ($C_{inv} = 3.5pF$), the capacitance of the depletion region C_{dep} below the gate can be derived according to equation 5.19 as

$$C_{dep} = 4.0pF. \tag{5.20}$$

Assuming that the measured capacitance corresponds to the geometric capacitance of the depleted volume, one can estimate the depletion depth below the gate as

$$x_{dep,min.cap.} = \frac{\epsilon_{Si} \cdot A}{C_{dep}} = 13\mu m. \tag{5.21}$$

With $\phi_F = -0.11V$ (equation 5.5), the depletion depth in inversion can also be estimated as [Gro67]

$$x_{dep} = \sqrt{\frac{2\epsilon_{Si}|2 \cdot \phi_F|}{qN_{eff}}} = 19\mu m, \tag{5.22}$$

which agrees reasonably with the minimum value from the capacitance measurement.

5.2.15 Gated diode measurements

The gated diode located on the test-structures allows the direct measurement of the contribution of the bulk generation current and of the interface current to the total leakage current [Gro67]. Fig. 5.24 shows a cross section through the cylindrical

symmetric gated diode and the connection scheme used for the measurements. The expected depletion volume in accumulation, depletion and inversion for the guard ring left floating is also sketched. The leakage current of the reverse biased diode is measured as function of the gate voltage applied to the aluminum gate surrounding the diode on top of the structure.

The measured I/V-curve for an unirradiated gated diode is shown in figure 5.26. Accumulation, depletion and inversion regions can clearly be distinguished.

In case of an electron accumulation layer below the gate, only the volume generation current I_V from the partially depleted bulk volume below the p^+-implant and the almost constant diffusion current from the backplane and n-region contribute to the total leakage current. The applied bias voltage of $V_{bias} = 5V$ corresponds to a depletion depth of about $80\mu m$ below the p^+-implant. The depletion volume below the floating guard is also sketched. Its depth can be determined from the built-in-potential V_{bi} (see section 5.2.8) as about $34\mu m$.

Once a depletion layer is created below the SiO_2, the interface states at the $SiO_2 - Si-$interface are not anymore shielded from the electric field and thus contribute to the measured current, which results in a steplike increase in the I/V-curve at $V_{gate} = V_{bias} + V_{fb}$. The interface area below the gate is about

$$A_{gate} = 3.5 \cdot 10^{-3} cm^2.$$

Also volume generation current from the depletion region below the gate adds now to the total leakage current. The depletion depth below the gate is about $20\mu m$ (see section 5.2.14.5).

If the gate is biased to inversion, the interface generation states are shielded from the electric field zone by a hole inversion layer below the interface and are unable to contribute to the measured current. A steplike decrease of the current is observed in the I/V curve at $V_{gate} = V_{fb}$. The hole-inversion-layer electrically connects the diode with the guard ring. Therefore the measured volume current in inversion consists of the generation current within the depletion region of the metallurgical junction below the diode and the guard ring and of the generation current within the depletion region of the field-induced junction below the gate.

The volume generation current increases with the square root of the backplane voltage (see section 1.4):

$$I_{vol} \propto \sqrt{V_{backplane} + V_{bi}}. \tag{5.23}$$

Since the diffusion current I_{diff} is almost independent from the backplane voltage, it is possible to separate both by measuring the gated diode leakage current at a fixed gate voltage as function of the bulk voltage. Figure 5.25 shows a measurement at $V_{gate} = -12V$. The leakage current is plotted against $\sqrt{V_{bulk} + V_{bi}}$. With a linear fit the diffusion current in inversion is obtained as the intercept of the curve with the current-axis. The estimated value is

$$I_{diff} = 15pA.$$

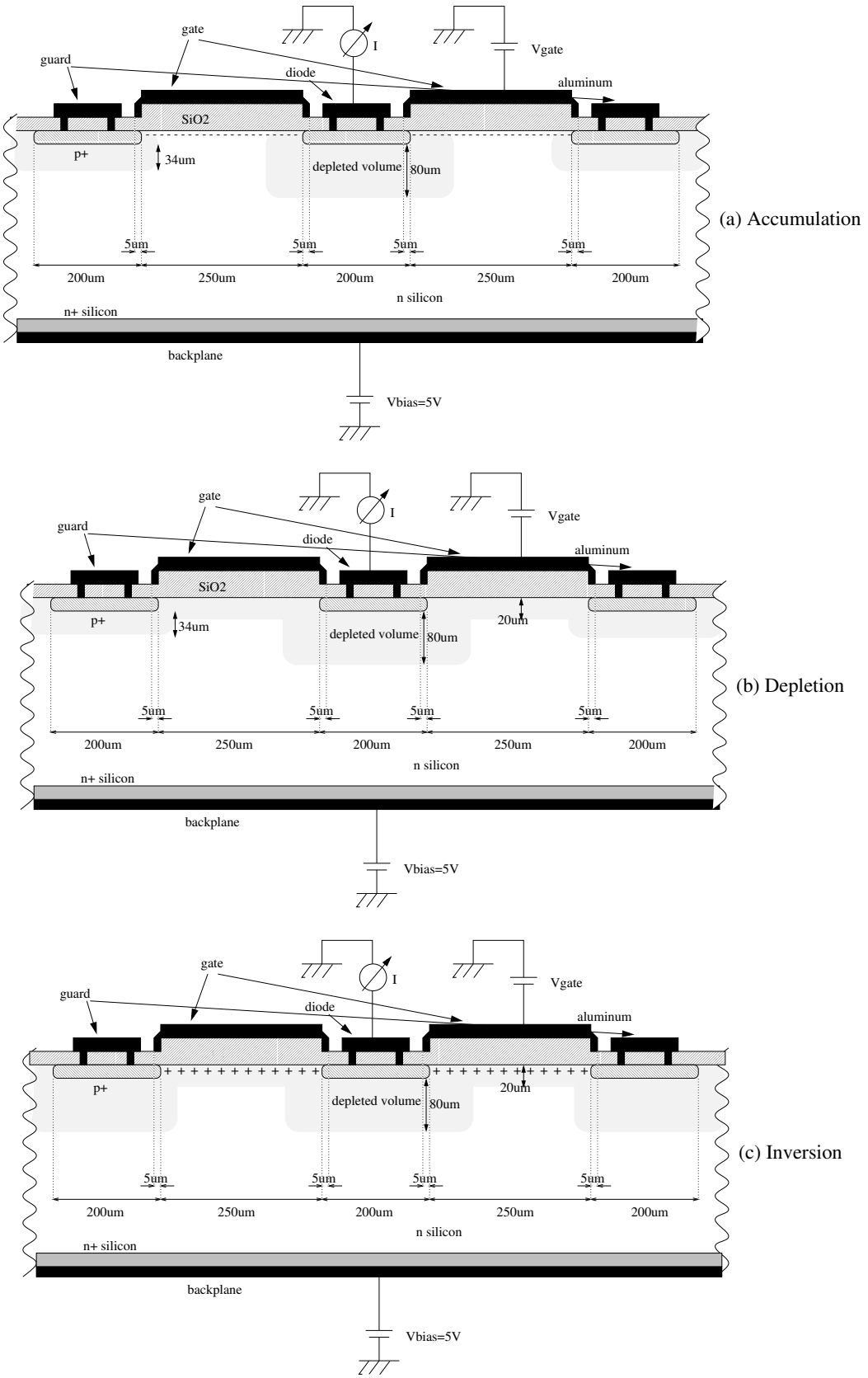

Figure 5.24: Cross section of gated diode ring-structure and connection scheme (not to scale). The depleted volume in accumulation (a), depletion (b) and inversion (c) is also sketched.

For estimating the surface generation current below the gate, the difference between the depletion- and the accumulation-plateau has been read from figure 5.26. Thus the additional volume generation current from the field induced junction below the gate has been neglected and it has been assumed that the diffusion current remains unchanged. A value of

$$I_{S,unirr.} = 17pA$$

has been obtained.

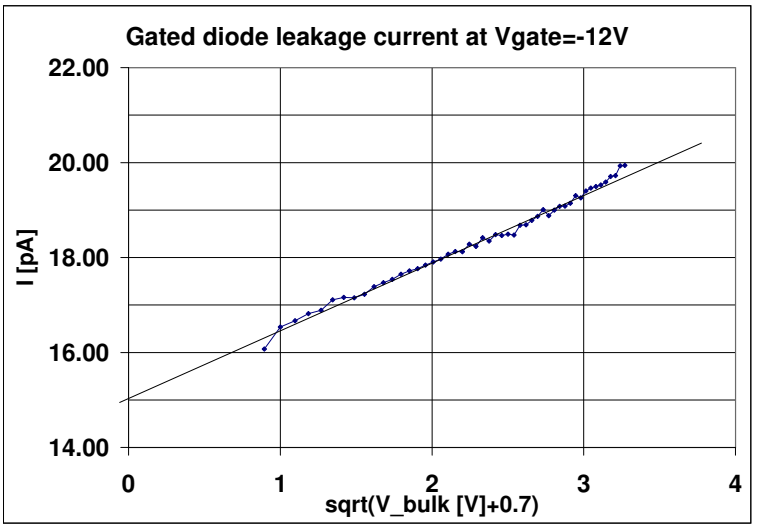

Figure 5.25: Gated diode I/V measurement that allows to estimate the diffusion current.

The flatband voltage can roughly be estimated from the I/V curve as the voltage where depletion and inversion region become separated [Gro67]. For the unirradiated detector a value of about

$$V_{fb} = -8V$$

can be obtained from figure 5.26.

Fig. 5.27 shows the gated diode measurement after $\gamma-$irradiation with $50Gy$. A shift in the flatband-voltage to

$$V_{fb,50Gy} = -15.5V$$

is observed. A small increase of the bulk generation current and a large increase of the surface generation current compared to the unirradiated measurement can be determined. For estimating the surface generation current, again the difference between depletion and inversion plateau has been taken, yielding a value of

$$I_{S,50Gy} = 260pA.$$

The shape of the I/V curve at depletion changes from a plateau to an almost linear decrease with further increasing negative gate voltage. This decrease is not expected

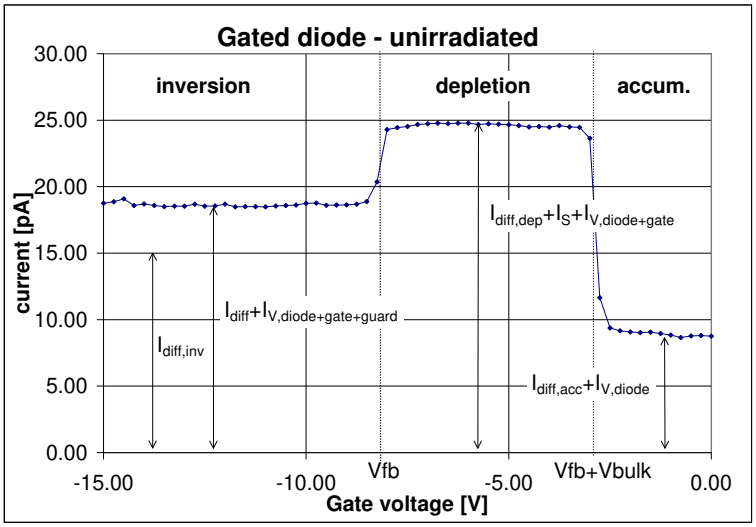

Figure 5.26: IV measurement of an unirradiated gated diode.

since the growing depletion region of the field induced junction below the gate should lead to a further increase of the measured current.

Fig. 5.28 shows the measurement result of another gated diode which was $\gamma-$irradiated with $2.8kGy$. The shape of the curve becomes more distorted compared to the irradiation with $50Gy$, making the interpretation of the results questionable. Thus only a rough estimation of I_S and V_{fb} can be obtained. A further shift of the flatband voltage to about

$$V_{fb,2.8kGy} = -60V$$

and a large additional increase of the interface generation current to about

$$I_{S,2.8kGy} = 5.5nA$$

are estimated from the plot.

The numerical results for the three measurements are summarized in table 5.3. The surface generation currents have been normalized to the area of $1cm^2$. The surface recombination velocity S_0 has been obtained from equation 1.34.

Dose	V_{fb}	I_S	S_0
$0Gy$	$-8V$	$4.9nA/cm^2$	$3.6cm/s$
$50Gy$	$-15.5V$	$74nA/cm^2$	$56cm/s$
$2.8kGy$	$-60V$	$1.6\mu A/cm^2$	$1200cm/s$

Table 5.3: Gated diode measurement results for different radiation doses.

The additional surface generation current after irradiation can be compared with results of the detector irradiation tests. The total leakage current of the detector

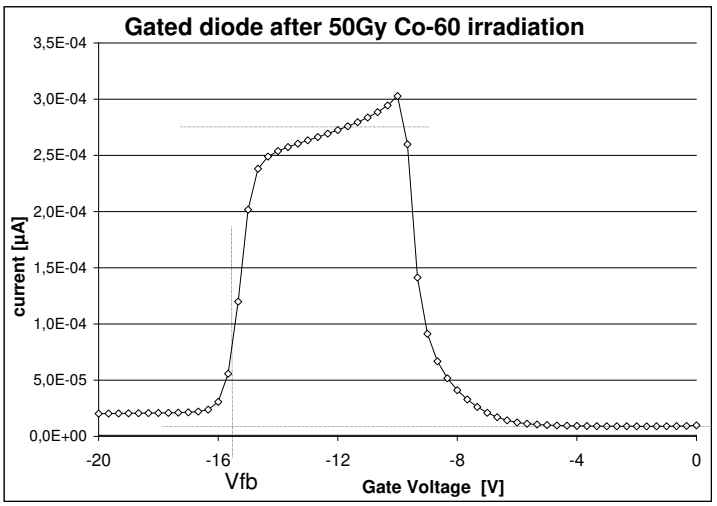

Figure 5.27: IV measurement of a gated diode after $\gamma-$irradiation with $50Gy$.

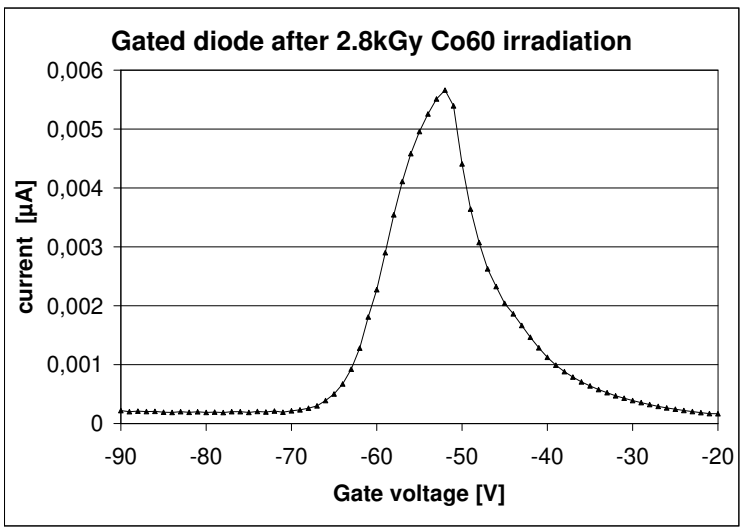

Figure 5.28: IV measurement of a gated diode after $\gamma-$irradiation with $2.8kGy$.

which was $\gamma-$irradiated floating with $2kGy$ was about $20nA$ before and $20\mu A$ after the irradiation. Assuming that the additional leakage current after the irradiation is only a surface generation current and that the whole $SiO_2 - Si-$interface area is taking part in the current generation, the surface current would be about $I_S = 1.37\mu A/cm^2$. This estimation for the current density is a lower limit since only the depleted part of $SiO_2 - Si-$interface area contributes to the surface generation current. Assuming a linear increase with the dose, the value at $2.8kGy$ would be about $I_S = 2\mu A/cm^2$, which corresponds to the order of the surface generation current of the gated diode. For the biased irradiation the detector leakage current after irradiation was about a factor of 10 larger.

Published values for the surface generation currents of similar material, but processed at other manufacturers, are one order of magnitude lower compared to the results from the gated-diode measurements [Wun99],[Fei97].

The large increase in the volume generation current as observed at the gated diode measurements thus was not expected for low energetic $\gamma-$ irradiation.

5.2.16 Hole mobility in the interface area

The defects located at the $SiO_2 - Si-$interface do not only act as generation centers for the surface generation current but also as scattering centers for the charges below the interface. With the PMOS-transistor of the test-structures the change of the hole mobility after irradiation can be measured. A decrease of the hole mobility indicates additional defects directly at the interface.

Figure 5.29 shows a cross-section of the PMOS-transistor and the connection scheme used for the measurements in this work. The (hole-)current between the p^+-implants is regulated with the gate voltage V_G which can create an accumulation-, depletion- or inversion layer below the SiO_2-Si-interface. In case of accumulation or depletion both $p-n-$junctions are reverse biased and the drain-source-current will almost be zero. An inversion layer between the p^+-implants connects the p^+-implants and allows a current of majority carriers between drain and source. The current is controlled by the density of holes below the interface, which depends (for small values of the drain voltage V_D) linearly on the gate voltage V_G. The threshold voltage V_{th} is reached when the gate voltage has compensated for the positive charges in the oxide and the work function difference and starts building an inversion layer. For a gate voltage below V_{th} and small values of the drain-source-voltage V_{DS} the drain-source-current I_{DS} is given as [Gro67]

$$I_{DS} = \frac{W}{L}\mu_h \frac{\epsilon_{SiO_2}}{t_{ox}} V_D \cdot (V_G - V_{th}). \tag{5.24}$$

On the test-structures for the MVD detector modules 3 different $W/L-$ratios are realized ($W/L = 0.5, 1, 2$). Also the gate controlled diode can be used as a PMOS-transistor, if the voltage is applied between diode and guard ring. Figure 5.30 shows the I/V curve for the gated diode used as PMOS-transistor with $W/L = 5.7$[3]. The shift

[3]The channel length has been approximated by the width of the gap between the diode and the

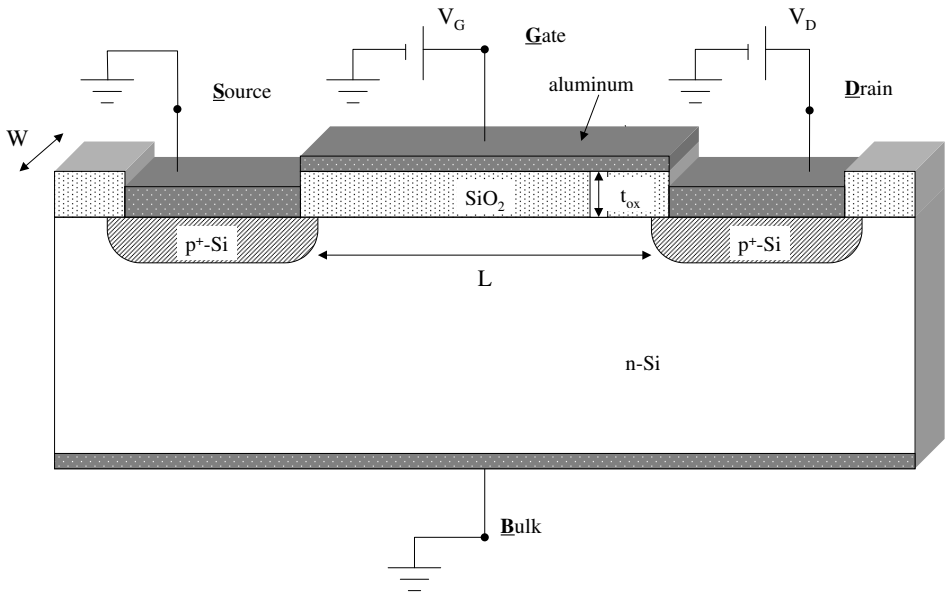

Figure 5.29: Scheme of PMOS-measurement-setup.

in the threshold-voltage from $V_{th} = -7V$ to $V_{th} = -62V$ corresponds to the shift in the flatband-voltage measured at the MOS-capacitor and the gated diode (see sections 5.2.14 and 5.2.15). The results are compared in table 5.4. The values derived from the different test-structures agree.

Parameter	Before irradiation	After $50Gy$ $\gamma-$irrad.	After $2.8kGy$ $\gamma-$irrad.
V_{fb} at MOS-cap.	$-7V$	-15	$-60V$
V_{fb} at gated diode	$-8V$	$-15.5V$	$-60V$
V_{th} at PMOS-trans.	$-6.5V$	$-16V$	$-62V$

Table 5.4: Comparison of flatband and threshold voltage observed on the different test structures for different radiation doses.

The hole mobility μ_h is proportional to the slope of the $I/V-$curve according to equation (5.24). With an oxide thickness of about $t_{ox} = 600nm$, as derived from the MOS capacitor measurement (section 5.2.14.1), the mobility of the holes below the gate can be estimated from the I/V-curve of the PMOS measurement. The change of the slope corresponds to a change in the hole-mobility from

$$\mu_{h,unirrad} = 370cm^2/Vs$$

guard ring ($L = 250\mu m$). For the channel width the mean perimeter of the gap has been used ($W = 1414\mu m$).

before irradiation to

$$\mu_{h,2.8kGy} = 80cm^2/Vs$$

after irradiation. These values can be compared to the hole mobility for intrinsic silicon at T=20^oC (see table 1.1):

$$\mu_{h,intr.} = 450cm^2/Vs$$

.

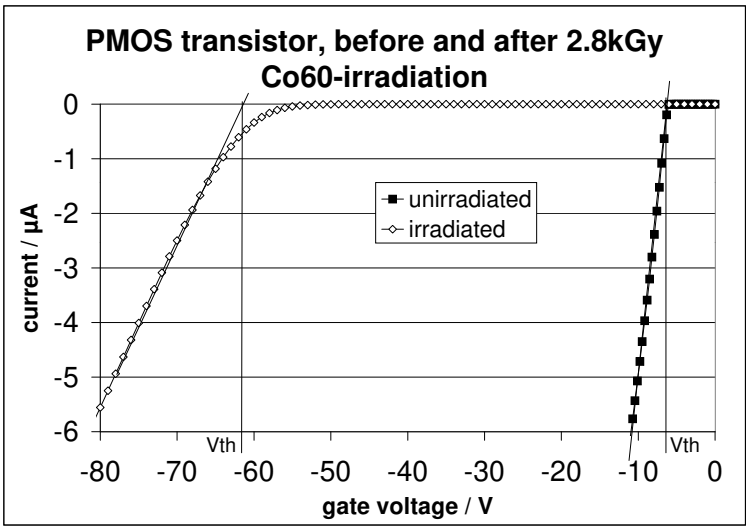

Figure 5.30: IV measurement of a PMOS FET with W/L=5.7 before and after 2.8kGy $\gamma-$irradiation, measured at $V_D = 0.1V$.

5.2.17 $p^+ - p^+-$isolation

The ohmic resistance measured between two adjacent strips (interstrip resistance) is an important parameter affecting the charge division at the detector surface. The interstrip capacitance between adjacent strips can be superimposed by an ohmic contact between the strips. In this case the charge division is no longer determined only by the interstrip capacitance but the amount of charge which is transferred to neighbouring strips becomes a function of the complex impedance of the parallel circuit between the interstrip capacitance and interstrip resistance. Instable and spreading values of the interstrip resistance thus worsen the resolution of the detector. Low resistances on the order of the biasing resistors (2$M\Omega$) can also locally change the DC potential of the strips, which has to be the same for all strips (see section 5.2.5).

The ohmic resistance between two adjacent p^+-strips is expected to be very high since one of the two $p-n-$junctions is always reverse biased. If no electron accumulation is present, both strips are grounded and the backplane is positively biased, the electric potential between the strips is expected to be a parable with a minimum in the middle (see figure 5.31). The depth of the minimum increases with the bias voltage

and with the gap between the strips. An external voltage applied to one of the strips leads to a distortion of the interstrip potential. If the voltage is high enough, the minimum of the potential vanishes and a current due to hole injection arises. Charges in the SiO_2, interface charges and an electron accumulation layer below the oxide affect the shape of the potential between the strips. Therefore a change of the measured I/V-characteristic between adjacent strips is expected after irradiation.

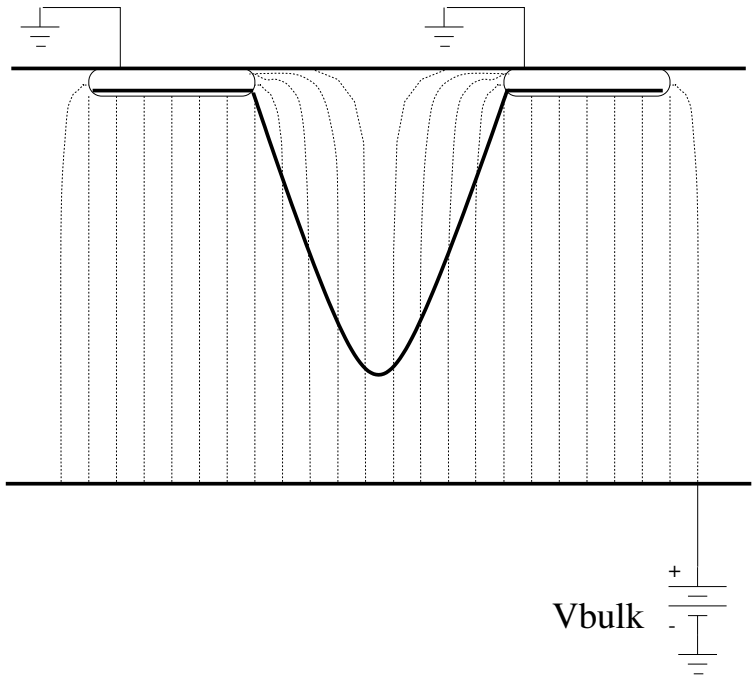

Figure 5.31: Devolution of the electric potential between adjacent strips for unbiased situation without an electron accumulation layer.

The measurement of the interstrip isolation can not be performed on the detectors, since the p^+- strips are not accessible from outside and all strips are connected through the biasing resistors. On the test structures there are separated p^+-fingerstrip-structures with contact pads for the p^+- strips (figure 3.3). Two different strip widths are available. The $12\mu m$ structure (W12) corresponds to a gap between the strips of $8\mu m$, for the $14\mu m$ structure (W14) the gap is $6\mu m$. On the detector the gap between readout strips (W14) and intermediate strips (W12) is $7\mu m$, between two intermediate strips it is $8\mu m$.

Figure 5.32 shows a sketch of the setup which has been used for measuring the resistance between adjacent strips. One should keep in mind that the measured current is the sum of the current between the strips and the leakage current from the backplane, which makes it impossible to determine the interstrip resistance independently from the backplane leakage current, since also the latter changes as function of the strip potential. Thus the measurements after irradiation with increased backplane leakage current have not been used to estimate the interstrip resistance in the region around

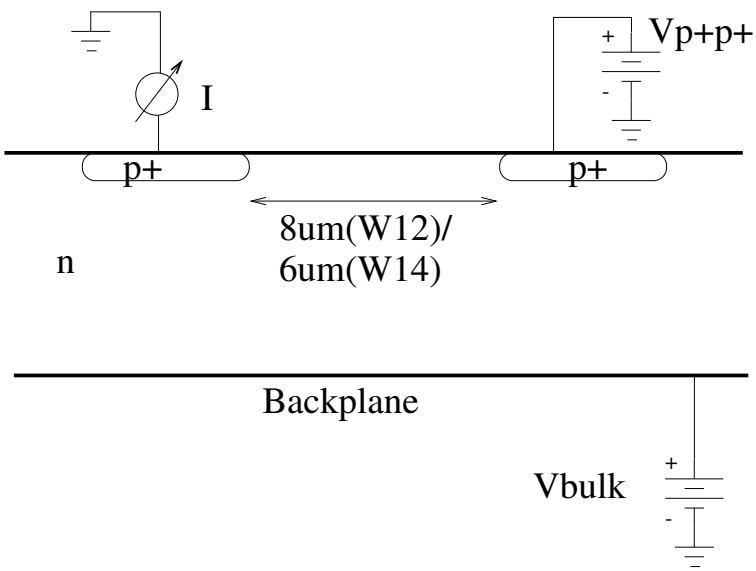

Figure 5.32: Setup used for $p^+ - p^+$−isolation measurements on the fingerstrip structures.

$V_{p^+p^+} = 0V$.

5.2.17.1 $p^+ - p^+$−isolation at unirradiated test-structures

Figure 5.33 shows measurements for the unirradiated W12 structure at different bulk voltages. The interstrip resistance corresponds to the slope of the I/V curve. If the backplane is at zero potential and both strips are kept also on the same potential, as they are normally during detector operation, the interstrip resistance is about $R_i = 130k\Omega$.

The I/V curves with applied backplane voltage allow to distinguish two regions. Below a certain break-through voltage V_{bt} the interstrip resistance is very high ($R_i \approx 400G\Omega$). If V_{bt} is reached, the slope of the I/V curve changes to a steep linear increase corresponding to an interstrip resistance of about $R_i \approx 100k\Omega$) for all bulk voltages. The value of V_{bt} is increasing with increasing bulk voltage from $V_{bt} = 5V$ at $V_{bulk} = 10V$ to $V_{bt} = 14V$ at $V_{bulk} = 200V$. This behaviour can be understood with the model introduced before. The increasing bulk voltage increases the depth of the potential minimum between the strips and therefore the break-through voltage, at which charge injection leads to a current between the strips, is increased.

Figure 5.34 shows the same measurement for the W14 fingerstrip structure. Also here the measurement at $V_{bulk} = 0V$ corresponds to a low interstrip resistance of about $R_i = 80k\Omega$ around $V_{p^+p^+} = 0V$. The interstrip resistance with applied bulk voltage is about $R_i = 95k\Omega$ above the break-through voltage V_{bt} which is similar to the W12 measurement. In the plateau region the interstrip resistance is about $R_i \approx 360G\Omega$. The break-through voltages are shifted to lower values compared to the W12 measurement. V_{bt} ranges for the W14 measurement from $V_{bt} = 5V$ at $V_{bulk} = 10V$ to $V_{bt} = 14V$ at

$V_{bulk} = 200V$. The smaller distance between the strips at the W14 structure leads to a less deep potential minimum between the strips compared to the W12 measurement, which can already be counterbalanced at a lower value of $V_{p^+p^+}$.

During its operation, the detector is biased with a voltage above the depletion voltage of about $V_{depl} = 65V$ (for unirradiated detectors) and all strips are kept at the same potential. At these conditions, the measurements at the unbiased W12 and W14 structures show a suitable high value of about $R_i \approx 400G\Omega$ (W12) and $R_i \approx 360G\Omega$ (W14). In this case the resistance between the strips is dominated by the value of the biasing resistors, which is on the order of $2M\Omega$.

5.2.17.2 $p^+ - p^+-$isolation after $\gamma-$irradiation

The same measurements were performed on a test structure after floating $\gamma-$irradiation with $2kGy$. Figure 5.35 shows the measurement at the W12 structure. The measured current, which is the sum of the leakage current from the backplane and the interstrip current, starts at different plateau-values, depending on the bulk voltage[4]. The measurement at $V_{bulk} = 0V$ shows a resistance of about $R_i = 140k\Omega$. The break-through voltage V_{bt} has shifted to values which are about $3V$ lower compared to the unirradiated measurements. V_{bt} ranges from $V_{bt} = 2.5V$ at $V_{bulk} = 10V$ to $V_{bt} = 11.5V$ at $V_{bulk} = 200V$. The resistance values in the region above the break-through voltage are very close to the values before irradiation ($R_i \approx 90k\Omega$ for $V_{p^+p^+} > V_{bt}$).

Figure 5.36 shows a measurement after irradiation at the W14 structure. Also here a shift of the break-through voltage of about $3V$ towards lower values is observed. The values of V_{bt} are already close to $0V$ (from $V_{bt} = 1V$ at $V_{bulk} = 10V$ to $V_{bt} = 5.5V$ at $V_{bulk} = 200V$). The interstrip resistance is about $R_i = 80k\Omega$ for the measurement at $V_{bulk} = 0V$. With $R_i \approx 95k\Omega$ for $V_{p^+p^+} > V_{bt}$ the interstrip resistance above the break-through voltage is the same as for the unirradiated measurement. The curve with $V_{bulk} = 80V$ shows a break-through voltage of about $V_{bt} = 3V$. Also this potential difference should not be reached between adjacent strips at a normal detector operation. But if the curves shift further towards lower values of V_{bt}, problems for the charge division could possibly occur.

[4]For the measurements on unirradiated test structures the plateaus were not visible since the leakage currents before and after irradiation differ by almost 3 orders of magnitude (see section 5.2.12.3).

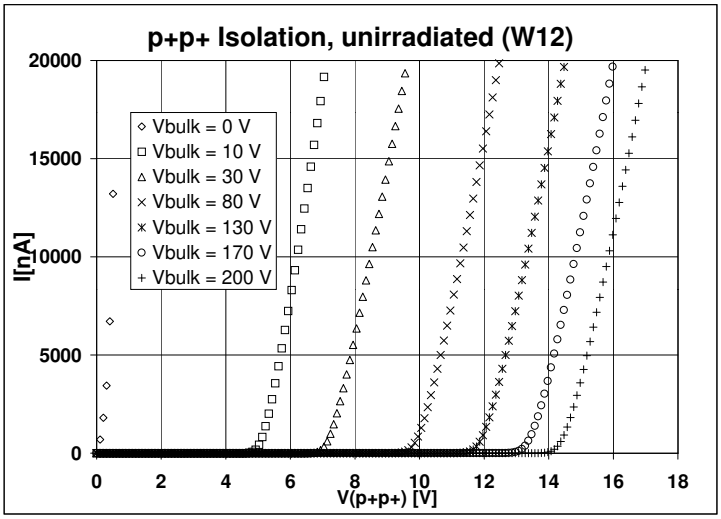

Figure 5.33: I/V characteristics between adjacent p^+-strips before irradiation (W12).

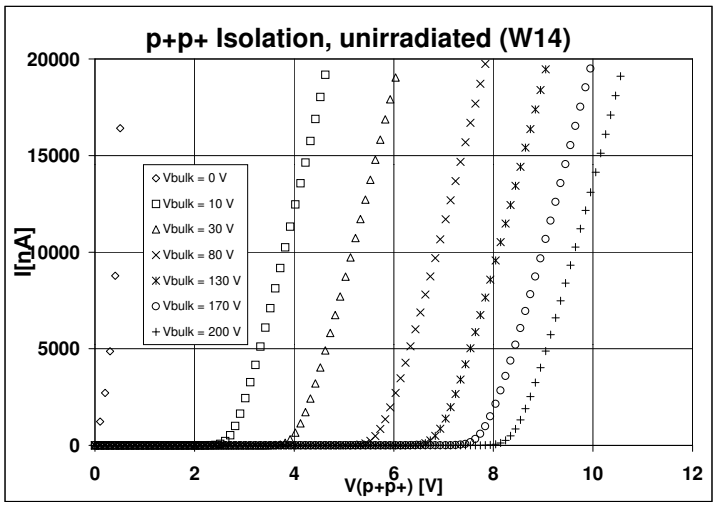

Figure 5.34: Isolation between adjacent p^+-strips before irradiation (W14).

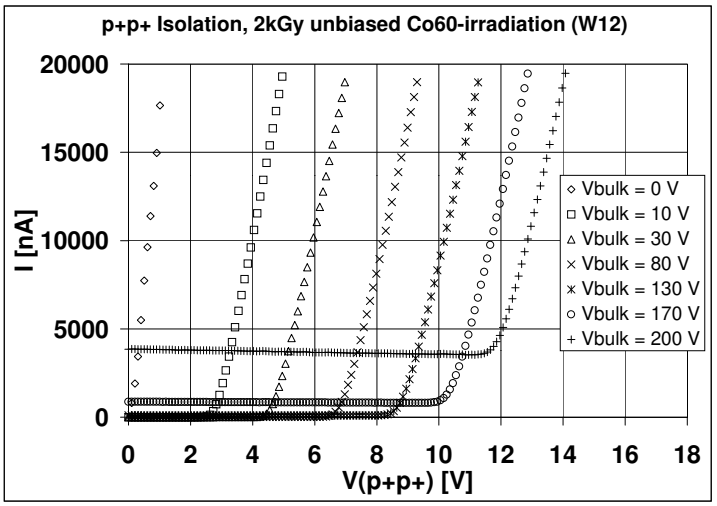

Figure 5.35: Isolation between adjacent p^+-strips after unbiased $^{60}Co-$ irradiation with $2\,kGy$ (W12).

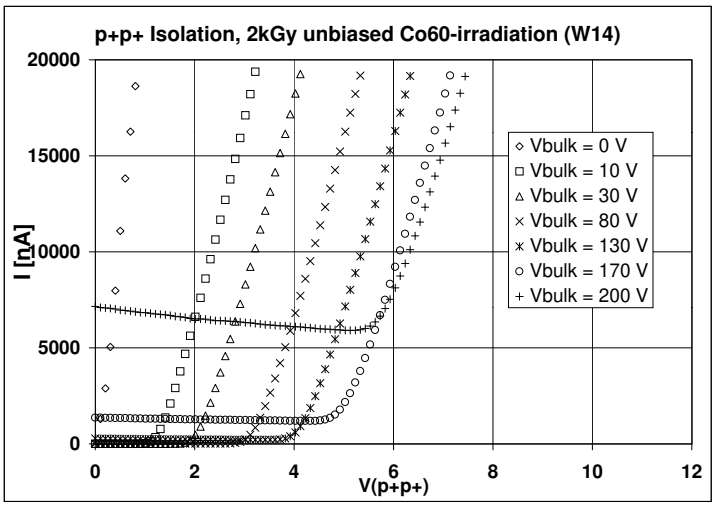

Figure 5.36: Isolation between adjacent p^+-strips after unbiased $^{60}Co-$ irradiation with $2\,kGy$ (W14).

5.2.18 Summary of electrical measurements and conclusions for production quality control

The results of the electrical measurements at the prototype detectors and at the test-structures are summarized and compared to the specifications in table 5.5.

parameter	symbol	measured value	specified value	measurement location
Bulk capacitance at full depletion	C_{bulk}	$1.34nF$	$1.35nF$[5]	detector
Voltage of full depletion	V_{dep}	$60V < V_{dep} < 70V$	$60V < V_{dep} < 95V$	detector
1 week after n-irradiation with $\phi_{eq} = 1 \cdot 10^{13} cm^{-2}$	$V_{dep,1w}$	$17V$	-	detector
3 weeks after n-irradiation	$V_{dep,3w}$	$30V$	-	detector
Effective doping concentration	N_{eff}	$7.9 \cdot 10^{11} cm^{-3}$	-	detector
1 week after n-irradiation	$N_{eff,1w}$	$2.1 \cdot 10^{11} cm^{-3}$	-	detector
3 weeks after n-irradiation	$N_{eff,3w}$	$3.7 \cdot 10^{11} cm^{-3}$	-	detector
Fermi potential of n-bulk	ϕ_F	$-0.11V$	-	detector
Resistivity of n-material	ρ	$5.3k\Omega cm$	$3k\Omega cm < \rho < 6k\Omega cm$	detector
Biasing resistors	$R_{poly-si}$	$1.5M\Omega < R_{poly-si} < 2.5M\Omega$	$1.0M\Omega < R_{poly-si} < 2.0M\Omega$	test-struct.
p^+ strip resistance	R_{p^+}	$90k\Omega/cm(W12)$ $100k\Omega/cm(W14)$	$< 150k\Omega/cm$	test-struct.
after n-irradiation	$R_{p^+,n-irrad}$	$90k\Omega/cm(W12)$ $100k\Omega/cm(W14)$	-	test-struct.
Doping concentration of p^+-implants	N_a	$5.8 \cdot 10^{19} cm^{-3}$	-	test-struct.
Built-in-voltage	V_{bi}	$0.7V$	-	test-struct.
Aluminum strip resistance	R_{Alu}	$< 20\Omega/cm$	$< 20\Omega/cm$	det./test-str.
Coupling capacitance	C_c	$27pF/cm$	$> 20pF/cm$	det./test-str.
Max. leakage current through C_c	I_{cc} at $V_{cc} = 100V$	$< 20pA$	$< 100pA$	detector
Total leakage current	$I_{leakage}$	$\lesssim 100nA$ at $Vbias = 200V$	$< 2\mu A$ at $Vbias = 200V$	detector
1 week after n-irradiation	$I_{leakage,1w}$	$620\mu A$ at $Vbias = 200V$	-	detector

[5]Value corresponding to the geometrical capacitance at the specified detector thickness of $d = 300\mu m$. At the measured detector thickness of about $d = 330\mu m$, the geometric capacitance is $C_{geom} = 1.23nF$.

parameter	symbol	measured value	specified value	measurement location
3 weeks after n-irradiation	$I_{leakage,3w}$	$420\mu A$ at $Vbias = 200V$	-	detector
Directly after $2kGy$ unbiased $\gamma-$irradiation	$I_{leakage,\gamma,u}$	$24\mu A$ at $Vbias = 200V$	-	detector
Directly after $2.8kGy$ $\gamma-$irradiation at $V_{bias} = 100V$	$I_{leakage,\gamma,b}$	$425\mu A$ at $Vbias = 200V$	-	detector
Guard ring current	I_{guard}	$\approx$ 6% of total leakage current	-	detector
Thickness of field oxide	t_{ox}	$600nm$	-	test-struct.
Flatband voltage[6]	V_{fb}	$-7V$	-	test-struct.
After $50Gy$ $\gamma-$irradiation	$V_{fb,50Gy}$	$-15.5V$	-	test-struct.
After $2.8kGy$ $\gamma-$irradiation	$V_{fb,2.8kGy}$	$-60V$	-	test-struct.
Density of oxide- and interface-charges	N_{ox}	$2.2 \cdot 10^{11}$ $states/cm^2$	-	test-struct.
After $50Gy$ $\gamma-$irradiation	$\Delta N_{ox,50Gy}$	$2.5 \cdot 10^{11}$ $states/cm^2$	-	test-struct.
After $2.8kGy$ $\gamma-$irradiation	$\Delta N_{ox,2.8kGy}$	$1.8 \cdot 10^{12}$ $states/cm^2$	-	test-struct.
Surface generation current	I_S	$4.9nA/cm^2$	-	test-struct.
After $50Gy$ $\gamma-$irradiation	I_S	$74nA/cm^2$	-	test-struct.
After $2.8kGy$ $\gamma-$irradiation	I_S	$1.6\mu A/cm^2$	-	test-struct.
Surface recombination velocity	S_0	$3.6cm/s$	-	test-struct.
After $50Gy$ $\gamma-$irradiation	$S_{0,50Gy}$	$56cm/s$	-	test-struct.
After $2.8kGy$ $\gamma-$irradiation	$S_{0,2.8kGy}$	$1200cm/s$	-	test-struct.
Hole mobility at the SiO_2-Si-interface	μ_h	$370cm^2/Vs$	-	test-struct.
After $2.8kGy$ $\gamma-$irradiation	$\mu_{h,2.8kGy}$	$80cm^2/Vs$	-	test-struct.
Interstrip resistance	R_i	$400G\Omega$ (W12) / $360G\Omega$ (W14)	-	test-struct.
Interstrip break-through voltage	V_{bt} at $V_{bulk} = 80V$	$9.5V$(W12) / $5.5V$(W14)	-	test-struct.
After $2.8kGy$ $\gamma-$irradiation	$V_{bt,\gamma}$ at $V_{bulk} = 80V$	$6.5V$(W12) / $3V$(W14)	-	test-struct.

Table 5.5: Electrical specifications and measurement results for BMVD prototype detectors and test-structures.

All measured values complied with the electrical specifications. The values of the

[6]Average value estimated from MOS capacitor-, gated-diode- and PMOS-measurement.

biasing resistors, which are slightly above the specifications, also meet the aim of the specifications, as explained in section 5.2.5.

The measurement results after irradiation with $1MeV$ neutrons at a fluence of $\phi_{eq} = 1 \cdot 10^{13} cm^{-2}$ are in agreement with the predictions from empirical formulae. It has been shown that type inversion will most probably not occur during the lifetime of the MVD and that the influence of hadronic irradiation on the detector operation is limited to a change in the depletion voltage and an increase of bulk generation current.

After $\gamma-$irradiation up to $3kGy$ an unexpectedly large increase of the total detector leakage current has been observed. The increase after irradiation under bias was a factor of 20 larger compared to the unbiased irradiation. With measurements on gated diodes the increasing leakage current has been attributed to radiation induced additional interface generation current at the $SiO_2 - Si-$interface. As a further effect of ionizing radiation on the SiO_2-surface a large shift of the flatband voltage, corresponding to a positive charge up of the oxide-bulk and -interface, has been observed with measurements on MOS capacitors. Measurements on PMOS-transistors showed a decrease of the hole mobility in the silicon below the oxide with $\gamma-$irradiation. It has been attributed to radiation induced interface states, acting as scattering centers.

In order to check and understand the influence of ionizing radiation on the detector parameters in detail, further investigations are needed. In particular, an irradiation in small steps with a set of measurements in between the radiation steps would be necessary to find a possible saturation for the flatband voltage and the surface generation current.

For the quality control during the production phase of the MVD, the following measurement procedure has been agreed upon:

5.2.18.1 Measurements on all detectors before delivery

Before delivery, a set of measurements is performed on each detector at the manufacturer Hamamatsu. The measurement results are sent as EXCEL-files with the corresponding batch of detectors.

- *Leakage current.* An I/V curve is taken for the detector total leakage current through the bias ring and for the guard ring current.
- *Bulk capacitance.* A global C/V measurement is performed.
- *Single strip measurements.* All strips are electrically checked for coupling capacitance shorts, shorts between aluminum readout strips and interruptions in the aluminum readout strips.

5.2.18.2 Measurements on all detectors after delivery

In order to sort out detectors that do not fulfill the specifications, a set of key measurements has been defined that are performed for each detector after delivery.

- *Leakage current.* An I/V curve from 0 to $200V$ bias voltage is taken for the detector total leakage current through the bias ring and for the guard ring current. The results are compared with the Hamamatsu measurements.

- *Depletion voltage.* A global C/V measurement is performed and the depletion voltage is estimated from the $1/C^2-$plot. Also the effective doping concentration and resistivity of the material can be calculated from this measurement. The results are compared with the Hamamatsu measurements.

- *Long-term stability of the leakage current.* Each detector has to survive 24 hours at a bias voltage of $V_{bias} = 200V$ without exceeding the specified maximum leakage current of $I_{leakage,max} = 2\mu A$.

5.2.18.3 Measurements for a sample of each production batch

The production at the manufacturer ist split into production batches. Most of the specifications and technological parameteres have been found to vary only little inside each production batch. In order to become aware of changes in the production-technology or -material, measurements of these parameters will be performed on a sample of test structures of each production batch. Typical measurements for this quality control during the production are:

- *Value of the biasing resistors*

- *p^+ strip resistance for W12 and W14 strips*

- *Aluminum strip resistance*

- *Coupling capacitance between p^+-fingerstrips and aluminum*

- *Leakage current through coupling layers*

- *Field capacitor C/V measurement for different frequencies*

- *PMOS measurement at gated diode*

- *Gated diode leakage current*

- *Interstrip resistance*

The test-structures of all detectors will stay available for further measurements also after the assembly and mounting of the detector system. Thus, if needed, certain measurements can always be repeated for a larger sample of test-structures or further invented measurements can be performed.

Chapter 6

Summary

This thesis describes the quality control measurements on the silicon strip detector modules and test-structures for the ZEUS microvertex detector (MVD). The relation between the measurement results and the goal of the MVD, to improve the precision of the ZEUS tracking system, is presented. The resulting requirements for the MVD are introduced. The design specifications, based on these requirements, are given. It is shown how the specifications were confirmed by electrical measurements on detector modules and test-structures, and by measurements in an electron test beam.

The measurements agree with the specifications and the most important results are summarized as follows:

- A resolution of $\sigma_i \approx 7.5\mu m$ and a signal to noise ratio of about 22 was measured in the electron test beam.

- Measurements of unirradiated detectors showed a total leakage current below $100nA$. The depletion voltage was about $65V$, corresponding to an effective doping concentration of $N_{eff} = 7.9 \cdot 10^{11} cm^{-3}$.

- The total leakage current and effective doping concentration after a neutron irradiation test with $\phi_{eq} = 1 \cdot 10^{13} cm^{-2}$ agreed with expectations from empirical formulae.

- The total leakage current after $^{60}Co-$irradiation up to $2.9kGy$ increased to a maximum value of about $400\mu A$. At this dose a shift of the flatband voltage from $-7V$ pre- to $-60V$ post-irradiation was also observed, indicating an additional density of positive oxide- and interface states of about $\Delta N_{ox} = 1.8 \cdot 10^{12}\, states/cm^2$. Measurements on gate controlled diodes and PMOS transistors were performed, in order to investigate the source of post-irradiation increased currents. According to these measurements, the additional currents can be attributed to surface generation current from generation centers at the $SiO_2 - Si-$interface. The high leakage currents after $\gamma-$irradiation are still under study and additional irradiation tests are under way.

- A long-term measurement of the leakage current of eight detectors for six weeks showed no increasing currents.
- The values of the poly-silicon biasing resistors have been found to be of the order of $R_{poly-si} = 2M\Omega$.
- The p^+ strip resistance was measured to be about $R_{p^+} = 100k\Omega/cm$.
- The resistance of the aluminum readout strips was estimated to agree with the specification of $R_{alu} < 20\Omega/cm$.
- The coupling capacitance to the aluminum readout strips was measured to be about $C_c = 27pF/cm$.
- The quality of the coupling capacitance dielectric was tested and a leakage current below the specified maximum value of $I_{cc} = 20pA$ at a voltage of $V_{cc} = 60V$ has been observed. The unexpected sensitivity to voltage transients of about $10V/ms$, resulting in high leakage currents through the coupling capacitors ($I_{cc} > 100pA$ at $V_{cc} = 60V$) is still under study.
- The isolation between neighbouring p^+-strips has been tested. With an applied backplane voltage the interstrip resistance was found to be determined only by the biasing resistors.

Based on these results, a test-program for the production phase of the MVD has been agreed upon, which includes global leakage current and capacitance measurements as well as a long-term leakage current test for all arriving detector modules. In addition, measurements on a sample of test structures from each production batch are foreseen.

Appendix A

Measurement principle of an LCR meter

The measurement principle of the LCR meters used for the MVD measurements is shown in fig.A.1. [Pac92]

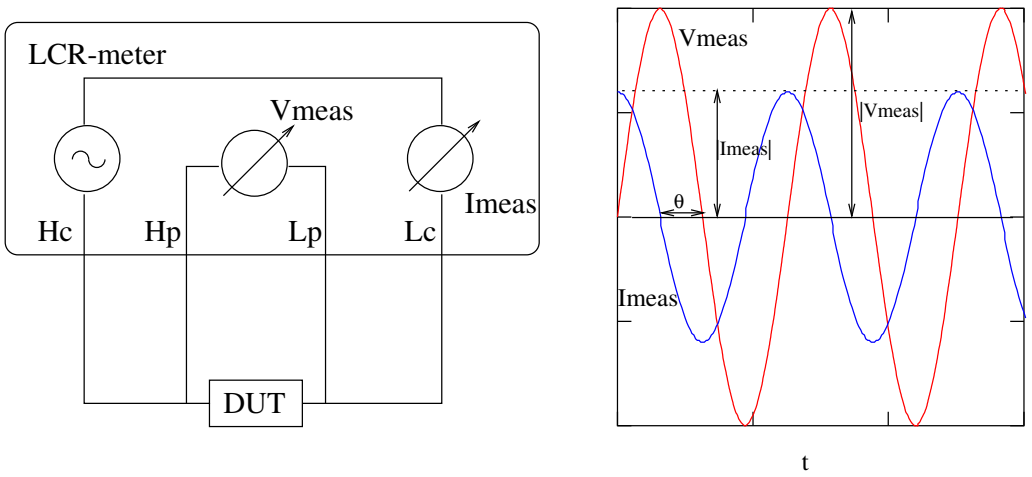

Figure A.1: Operation principle of an LCR meter

An adjustable AC-voltage ($level = 50mV..1V$, $f = \omega/2\pi = 120Hz..100kHz$) is applied to the DUT.

The amplitude $|I_{meas}|$ and phase shift θ of the current through the DUT is measured. $|Z| = |V_{meas}|/|I_{meas}|$ and θ lead to the complex impedance Z of the DUT:

$$Z = |Z|e^{i\theta} = \mathrm{Re}(Z) + i\ \mathrm{Im}(Z) \quad (A.1)$$

$$\mathrm{Re}(Z) = |Z|\cos\theta \quad (A.2)$$

$$\mathrm{Im}(Z) = |Z|\sin\theta \quad (A.3)$$

Besides $|U|/|I|$ and θ the LCR meter can also display derived parameters in different display modes. For the MVD measurements the following modes were used:

- *Series mode* (fig. A.2). The measured complex impedance is interpreted as a series circuit of a capacitance C_s and a resistor R_s: $Z = R_s + \frac{1}{i\omega C_s}$. The displayed values of C_s and R_s are derived from Z in this case as:

$$R_s = \mathrm{Re}(Z) = |Z|\cos\theta. \tag{A.4}$$

$$C_s = -\frac{1}{\omega \mathrm{Im}(Z)} = -\frac{1}{\omega |Z| \sin\theta} \tag{A.5}$$

- *Parallel mode* (fig. A.2). The measured complex impedance is interpreted as a parallel circuit of a capacitance C_p and a conductance $G_p = 1/R_p$: $Z = \frac{1}{G_p + i\omega C_p}$. The displayed values of C_p and G_p are thus derived from the measured complex impedance Z as:

$$G_p = \frac{\mathrm{Re}(Z)}{\mathrm{Re}(Z)^2 + \mathrm{Im}(Z)^2} = \frac{1}{|Z|}\cos\theta \tag{A.6}$$

$$C_p = -\frac{\mathrm{Im}(Z)}{\omega \mathrm{Re}(Z)^2 + \mathrm{Im}(Z)^2} = -\frac{1}{|Z|\omega}\sin\theta \tag{A.7}$$

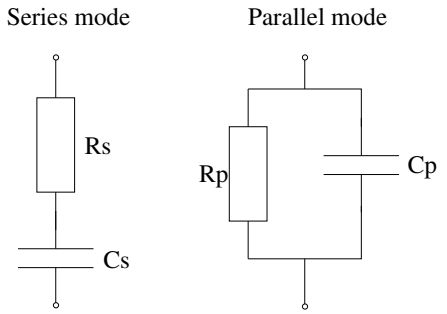

Figure A.2: Assumed equivalent circuits for parallel and series display mode of the LCR

As an example for the projection of the measured complex impedance to the displayed capacitance in parallel- and series-mode, the measurement of the detectors total bulk capacitance (section 5.2.1) can be evaluated.

For this measurement, as for all LCR measurements, the default setting was "parallel mode". Therefore it was assumed that the equivalent electronics circuit of the detector consists only of a capacitance C_{bulk} and a resistor $R_{bp} = 1/G_{bp}$ in parallel. A more realistic detector-model is shown in figure A.3. For symmetry reasons all 3070 strips can be combined in one line consisting of n elementary cells and one resistor R_{bias} in series. R_{bias} combines the parallel circuit of all poly-silicon biasing resistors $R_{poly-si}$ and the resistance of the undepleted bulk R_{undep} in series. Each elementary cell consists of 3 parts: One resistor R_{strip}/n along the strip represents the finite resistivity of the strips. The conductance of the depleted volume is carried by $R_{bp} \cdot n$. C_{bulk}/n represents the total bulk capacitance of the detector.

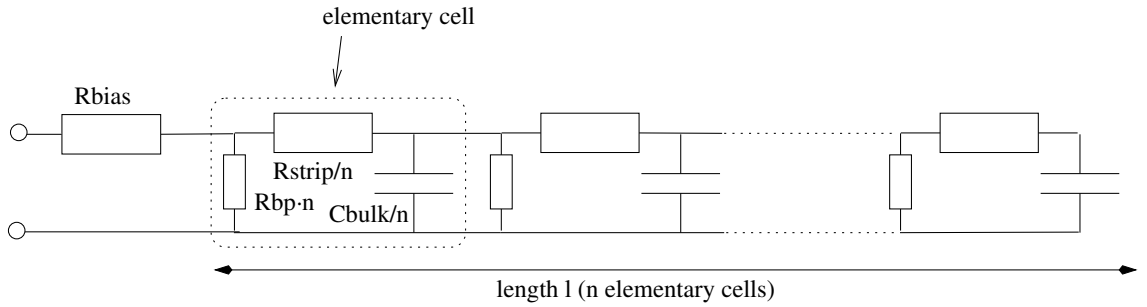

Figure A.3: Extended equivalent circuit for the detector measurements

For $n \to \infty$ the complex impedance of the detector according to this model can be evaluated by standard cable theory ([Küp90]) as

$$Z_{det} = R_{bias} + \sqrt{\frac{R_{strip}}{i \cdot \omega \cdot C_{bulk} + 1/R_{bp}}} \cdot \left(\tanh \sqrt{R_{strip} \cdot (i \cdot \omega \cdot C_{bulk} + 1/R_{bp})} \right)^{-1}. \tag{A.8}$$

The values for the resistors and capacitors in the model can be estimated from electrical measurements (see section 5.2) and are summarized in table A.1.

Parameter	value	remark
R_{bias}	$2.1M\Omega/3070 \approx 680\Omega$	Main reason for frequency dependence
R_{undep}	$< 12\Omega$	Maximum value for irradiated detector at low bias voltage, can be neglected against R_{bias}
R_{strip}	$600k\Omega/3070 = 195\Omega$	Contributes only very little to frequency dependence
R_{bp}	$25G\Omega$	Estimated from slope of I/V-curve
C_{bulk}	$1.3nF$	

Table A.1: Values for the resistors and capacitors in figure A.3

Figure A.4 shows the projection of Z_{strip}, measured at full depletion, to the displayed capacitance in parallel and series mode as function of the measurement frequency. From $0.1Hz$ up to $20kHz$ the displayed capacitance is very close to the detectors total bulk capacitance in both modes. For the highest measurement frequency of the HP 4263A ($f = 100kHz$) a lower capacitance value is displayed in parallel mode. This has been confirmed by the capacitance measurements on the prototype detectors (section 5.2.1). The curve for the parallel mode measurement is sensitive to the series resistance from the biasing resistors, which is about $R_{bias} = 680\Omega$. When the backplane voltage is applied on the top-side of the detector, the n^+-implantation through the bulk gives an additional contribution to the series resistance, which is in the order of the biasing

resistors ($R_{n^+} \approx 470\Omega$). The increased series resistance leads to a shift of the parallel mode curve in figure A.4 to lower frequencies. In this case it is preferable to measure in series mode. For the parallel mode capacitance measurements reported in this work, the biasing voltage was always applied directly to the backplane.

Similar calculations have also been performed in order to ensure the reliability of capacitance measurements on test-structures [Joh94].

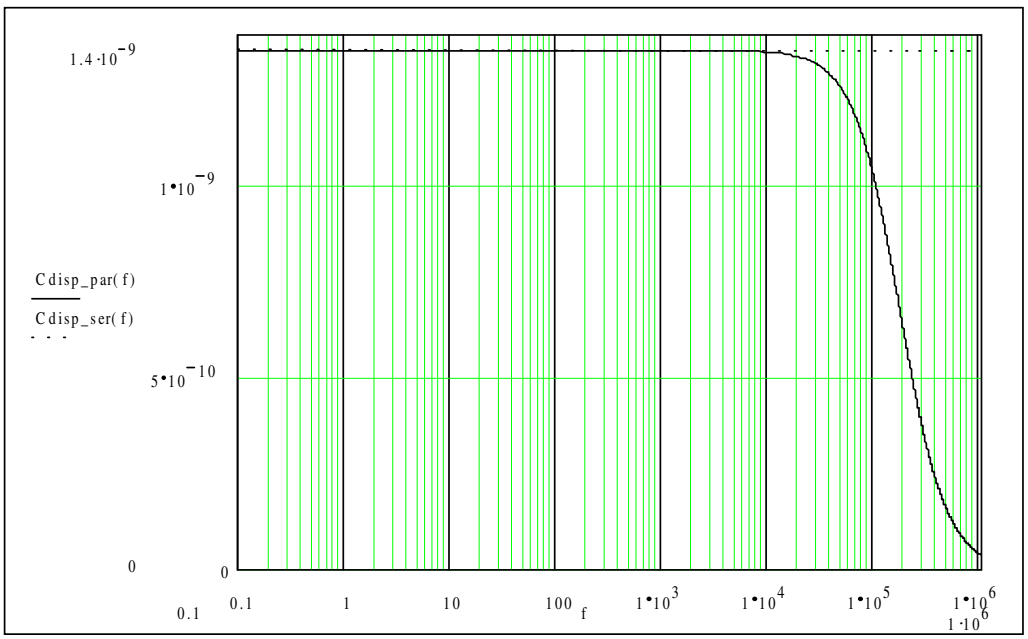

Figure A.4: Capacitance in parallel- and series-mode as function of measurement frequency

References

[AL90] L. Strüder A. Longoni, M. Sampietro, *Instability of the behaviour of high resistivity silicon detectors due to the presence of oxide charges*, Nuclear Instruments and Methods in Physics Research A (1990), 35–43.

[Bar98] G. Barichello et al., *A B_4C-silicon target for the detection of neutrino interactions*, CERN-EP-98-21 (1998), Submitted to Nuclear Instruments and Methods in Physics Research A.

[Bec97] G.A. Beck et al., *Radiation-tolerant breakdown protection of silicon detectors using multiple floating guard rings*, Nuclear Instruments and Methods in Physics Research A **396** (1997), 214–227.

[Bel83] G. Belau et al., *Charge collection in silicon strip detectors*, Nuclear Instruments and Methods **214** (1983), 253–260.

[Bra89] D. Braeunig, *Wirkung hochenergetischer Strahlung auf Halbleiterbauelemente*, Springer-Verlag, 1989.

[CER97] CERN, *Radiation monitoring and beam dump system of the opal silicon microvertex detector*, Tech. Report CERN-PPE/97-091, CERN, 1997.

[Eic98] R. Eichler, *Private communication*, 1998.

[Fei97] H. Feick, *Radiation Tolerance of Silicon Particle Detectors for High-Energy Physics Experiments*, Ph.D. thesis, Universität Hamburg, 1997.

[FM54] J.P. Maita F.J. Morin, *Electrical properties of silicon containing arsenic and boron*, Physical Review **96** (1954).

[FR97] M. Feurstack-Raible, *HELIX 128S-2 user manual version 1.9*, Tech. Report 33-0697, HD-ASIC, 1997.

[Gro67] A.S. Grove, *Physics and technology of semiconductor devices*, John Wiley & Sons, 1967.

[Joh94] T. Johnsen, *Evaluation of Test Structures for Position Sensitive Silicon Detectors*, Ph.D. thesis, University of Bergen, 1994.

[Kei98] *Low level measurements*, Keithley, 1998.

[Koe85] U. Koetz et al., *Silicon strip detectors with capacitive charge division*, Nuclear Instruments and Methods in Physics Research A **235** (1985), 481–487.

[Kuh97] M. Kuhnke, *Untersuchung von Defekten in MOS-dioden nach Schädigung mit 20 kev Elektronen*, Master's thesis, Universität Hamburg, 1997.

[Küp90] K. Küpfmüller, *Einführung in die theoretische Elektrotechnik*, Springer-Verlag, 1990.

[Lin99] G. Lindström, M. Moll, E. Fretwurst, *Radiation hardness of silicon detectors - a challenge from high-energy physics*, Nuclear Instruments and Methods in Physics Research A **426** (1999), 1–15.

[LJU] Jožef Stefan Institute and Department of Physics, University of Ljubljana, SI-1000 Ljubljana, Slovenia. (http://www.ijs.si:90/ijs-dept-r3.html).

[Mar99] J. Martens, *Private communication*, 1999.

[Mol99a] M. Moll, *Radiation damage in silicon particle detectors - microscopic defects and macroscopics properties*, Ph.D. thesis, Universität Hamburg, 1999.

[Mol99b] M. Moll, E. Fretwurst, G. Lindström, *Investigation on the improved radiation hardness of silicon detectors with high oxygen concentration*, 1999.

[NB82] E.H. Nicollian and J.R. Brews, *MOS (Metal Oxide Semiconductor) physics and technology*, John Wiley & Sons, 1982.

[Pac92] Hewlett Packard (ed.), *HP LCR 4263A manual*, Hewlett Packard, 1992.

[Rie98] K. Riechmann, *Overview of the HERA-B vertex detector system and first results from prototype runs*, Nuclear Instruments and Methods in Physics Research A **408** (1998), 221–228.

[Sch98] U. Schneekloth, *The HERA luminosity upgrade*, Tech. Report DESY HERA 98-05, DESY, 1998.

[Sus] *http://www.suss.com.*

[Sze81] S.M. Sze, *Physics of semiconductor devices*, John Wiley & Sons, 1981.

[Wun92] R. Wunstorf, *Systematische Untersuchungen zur Strahlenresistenz von Silizium-Detektoren für die Verwendung in Hochenergiephysik-Experimenten*, Ph.D. thesis, Universität Hamburg, 1992.

[Wun99] R. Wunstorf, *Private communication*, 1999.

[ZEU93] The ZEUS collaboration, *The ZEUS detector, status report 1993*, Tech. report, DESY, 1993.

[ZEU97] The ZEUS Collaboration, *A microvertex detector for ZEUS*, Tech. Report DESY-PRC 97/01, DESY, 1997.